Design, Optimization and Evaluation of an Extracorporeal Piezoelectric Lithotripter

Gilles Thomas

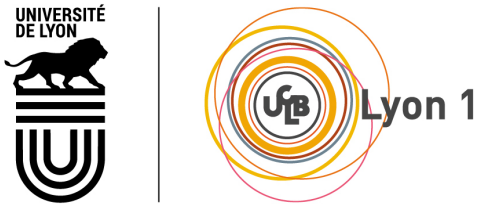

N° d'ordre NNT : 2019LYSE1021.

THÈSE DE DOCTORAT DE L'UNIVERSITÉ DE LYON
opérée au sein de
l'Université Claude Bernard Lyon 1

École Doctorale ED205
École Doctorale Interdisciplinaire Science-Santé

Spécialité de doctorat : Ingénierie Biomédicale
Discipline : Acoustique Thérapeutique

Soutenue publiquement le 25/02/2019, par :
Gilles Pierre Loïc THOMAS

Design, Optimization and Evaluation of an Extracorporeal Piezoelectric Lithotripter

---

Devant le jury composé de :

Nom Prénom, grade/qualité, établissement/entreprise	Président(e)
CLEVELAND Robin, Professeur, University of Oxford	Rapporteur
KHOKHLOVA Vera, Professeure Associée, Moscow State University	Examinatrice
LETHIECQ Marc, Professeur des Universités, Université de Tours	Rapporteur
MARTIN Xavier, Professeur des Universités, UCBL	Examinateur
PRADA Claire , Directrice de Recherche CNRS, Université Paris Diderot	Raporteur
CHAPELON Jean-Yves, Directeur de recherche, INSERM	Directeur de thèse
LAFON Cyril, Directeur de recherche, INSERM	Co-Directeur de thèse

UNIVERSITÉ DE LYON

Abstract

Université Claude Bernard
INSERM

Doctor of Philosophy

Design, Optimization and Evaluation of an Extracorporeal Piezoelectric Lithotripter

by Gilles THOMAS

Kidney Stones can be found in the kidney, ureter, or in the bladder, and affect about 1 in 11 people at least once in a lifetime in the US. Extracorporeal shock wave lithotripsy is a widely used technique where high intensity acoustic pulses are focused toward kidney stones in order to break them. The work presented in this thesis focus on optimizing piezoelectric lithotripter, both in design and efficiency, in order to have more efficient treatment while also being less costly. First, a study of the current state of lithotripsy was made, followed by experiments on commercial and experimental lithotripters in order to define properly the different parameters to be worked on. From this, it was decided to optimize the current piezoelectric elements in the lithotripter to obtain a more efficient treatment. Then, a lithotripter using optimized lens focused piezoelectric transducers set in confocal setups was designed and manufactured. Its acoustic characterization, effect on cavitation and model stone fragmentation efficiency were evaluated. The resulting lithotripter showed performances equivalent to existing commercial lithotripter, while allowing more flexible treatment than traditional lithotripter.

UNIVERSITÉ DE LYON

Résumé

Université Claude Bernard
INSERM

Grade de docteur

Conception, optimisation et évaluation d'un lithotriteur piézoélectrique extracorporel

par Gilles THOMAS

Les lithiases urinaires peuvent affecter le rein, l'uretère ou la vessie, et affectent en moyenne, au moins une fois durant leur vie, 1 personne sur 11 aux États-Unis. La lithotritie extracorporelle est une technique largement répandue dans le monde qui consiste à focaliser des ondes de choc acoustiques de haute intensité sur les lithiases afin de les briser. Le travail présenté dans cette thèse porte sur l'optimisation de la lithotritie piézoélectrique, à la fois dans sa conception mais aussi dans son efficacité, tout en réduisant son coût de fabrication. Premièrement, une étude de l'état de l'art de la lithotritie a été réalisée, suivie par des expériences sur des lithotriteurs commerciaux et expérimentaux afin de déterminer les différents axes de recherche de la thèse. Ensuite, une optimisation des éléments piézoélectriques d'un lithotriteur a été réalisée afin d'obtenir un traitement plus performant. Finalement, des lithotriteurs composés de transducteurs piézoélectriques focalisés grâce à des lentilles optimisées ont été conçus et fabriqués. Leurs champs acoustiques, leurs effets sur la cavitation et leur efficacité à fragmenter des lithiases artificielles ont été évalués. Les lithotriteurs résultant ont montré des performances équivalentes à des lithotriteurs commerciaux existant, tout en permettant un traitement plus flexible que ces derniers.

Contents

List of Figures

List of Tables

List of Abbreviations

BWL	**B**urst **W**ave **L**ithotripsy
ESWL	**E**xtracorporeal **S**hock **W**ave **L**ithotripsy
FDM	**F**used **D**eposition **M**odeling
FEM	**F**inite **E**lement **M**ethod
PML	**P**erfectly **M**atched **L**ayers
PRF	**P**ulse **R**epetition **F**requency
RPM	**R**evolution **P**er **M**inute
SWL	**S**hock **W**ave **L**ithotripsy
US	**U**ltra**S**ound

Chapter 1

Introduction

Extracorporeal shock wave lithotripsy was one of the first non invasive application of ultrasound therapy. Shock waves are generated outside the body and are focused toward the kidney stone in order to break it in small fragments that can pass the urinary tract naturally. As a substitute to surgery, it offered an uncontested safety and comfort and was, and still is, widely used around the world. Unfortunately, shock wave lithotripsy still presents weaknesses, such as inefficiency against certain type or size of stone, or even a rather high chance of needing to be treated for the same stone multiple times, that decades of research and development did not compensate. As a result, other more invasive surgical procedures that were initially used if the stone was not treatable by shock wave lithotripsy, beneficed from technological developments and are now widely used, representing a direct concurrent to shock wave lithotripsy. Slowly but surely, extracorporeal shock wave lithotripsy market is declining.

This thesis was realized in close collaboration between the public laboratory INSERM LabTau and the medical therapy company EDAP-TMS in a state sanctioned contract (CIFRE). The research interests of the laboratory LabTAU are focused on medical application of ultrasound, for both therapy and imaging. The company EDAP-TMS was funded by members of the LabTAU, and its products can be divided in two categories: extracorporeal lithotripsy (SONOLITH) and therapeutics ultrasound (HIFU).

The objective behind this thesis was to design, optimize and evaluate an extracorporeal lithotripter that could potentially improve both the efficiency of the treatment and the cost of manufacturing.

Chapter 2

State of the art

2.1 Introduction

A kidney stone is a solid inside the urinary tract, with a size comprised between a few millimeters up to a few centimeters. It usually forms in the kidney, and while the small ones can pass the urinary tract without trouble, others can get stuck and generate symptoms, often very painful. Before the 1980s and the apparition of non invasive methods of stone removal like lithotripsy, the stones were removed by surgery with elevated risk of mortality. This chapter will first introduce the kidney, the central part of the urinary tract, and then describe the kidney stones with their causes and management. Then, extracorporeal shock wave lithotripsy will be introduced in detail.

2.2 The kidney

The kidneys are at the center to the urinary system, which itself consists of a pair of kidneys and ureters, a bladder and an urethra. Their main role is the filtering of the blood, the byproduct being the urine, but also have secondary functions, such as controlling blood pressure, red blood cell production and calcium absorption. The kidneys are located in the human body between the 12^{th} thoracic and the 3^{rd} lumbar vertebrae (T12 and L3), with the right kidney slightly lower than the left due to the position of the liver. They are maintained in place by a layer of fat called the perirenal fat which also protects them from shock. The perirenal fat is itself surrounded by the renal/Gerota's fascia. The lateral, medial and posterior sides of the fascia are in contact with the pararenal fat. The kidneys are also in contact at their superior poles with the adrenal gland, directly influencing their sodium reabsorption. This next two subsection are a synthesis of the books [1], [2], and will cover the principal anatomy of the kidney without detailing much of its physiology.

2.2.1 Gross anatomy of the kidney

For an human adult, each kidney weights around 115-175 g, is about 12x6x4 cm in size, depending of the sex and individuals, and is immediately covered by a fibrous capsule that holds its shape. The outer region is called the cortex and the inner region the medulla, divided into approximately 8 lobes by the renal

columns, separating the renal pyramids and renal papillae. The renal pyramids have the form of a cone, with their base facing the cortex and their inner facing apex being the papilla. The papilla is a bundle of collecting ducts transporting urine to the minor calyces of the kidneys. From there, the urine flows to the major calyces, the renal pelvis and then the ureter. The flow from the pelvis to the ureter is realised via peristalsis by a smooth muscle. The renal artery is directly linked to the descending aorta and the renal vein to the inferior vena cava, and with the pelvis are linked to the kidney through the renal hilum. About 25% of the cardiac output at rest goes to the kidneys. An illustration of the gross anatomy of the kidney is presented in fig. 2.1.

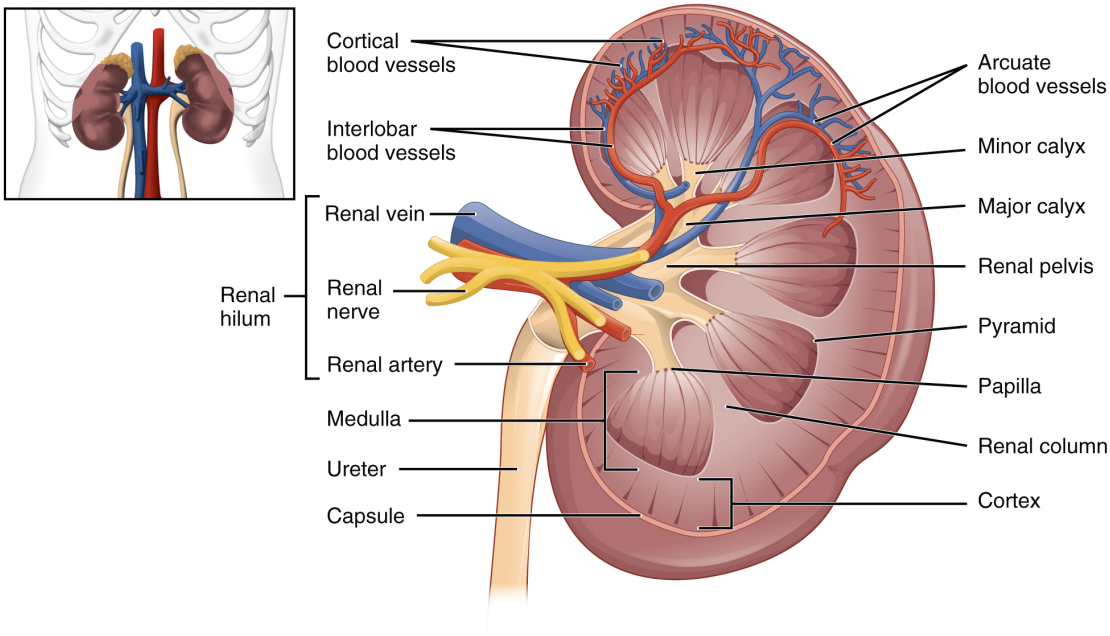

FIGURE 2.1: The internal anatomy of the left kidney [1].

2.2.2 Microanatomy of the kidney

The renal artery divides into segmental arteries, that in turn divide in interlobar arteries, which divide into arcuate arteries, cortical arteries and finally afferent arterioles that serve about 1 million nephrons (per kidney). The nephron function is to cleanse and balance the blood. The afferent arterioles form the glomelurus, a high pressure capillary, which combined with the Bowman's capsule forms the renal corpuscle, located in the cortex, and is responsible for the filtration of the blood, while the other part of the nephron, the renal tubule, is responsible for the reabsorption of proteins, amino acids, glucose, creatine, water and Na^+ and Cl^- ions. The blood flow to the nephron and its anatomy is presented in fig. 2.2.

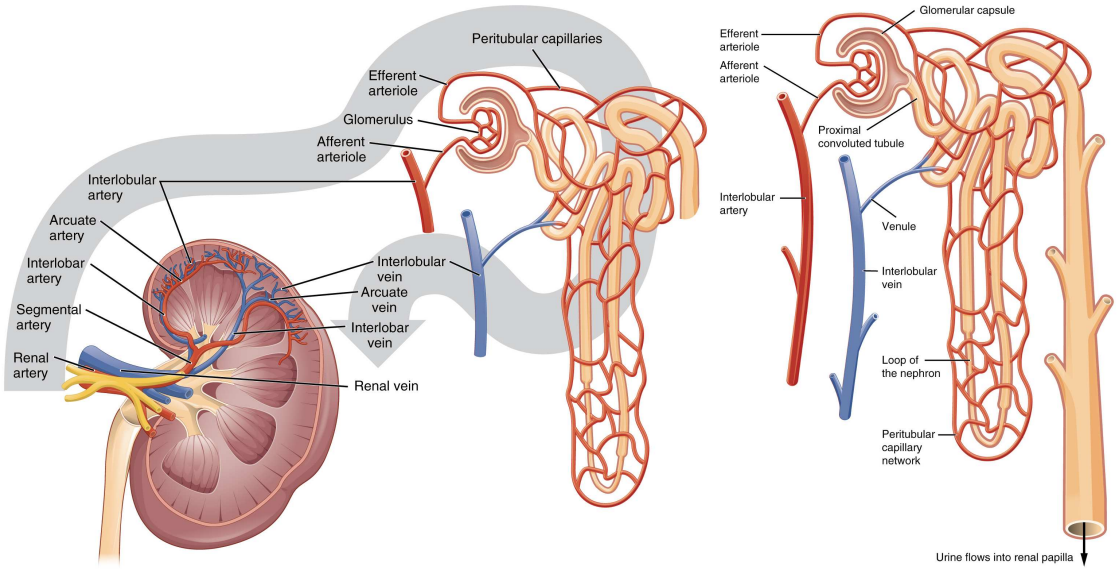

FIGURE 2.2: Left: the blood flow to the nephron, right: the nephron anatomy, [1].

2.2.3 Animal model

Animal models are important in evaluating new treatments before they are applied to humans. In urology, the first models were rabbits and dogs, but were rapidly replaced by the porcine kidney as a model. The pig's kidney is similar to the human kidney in size, weight and function [3]–[7]. On the morphological point (size and weigth), the similarity is very high [5], with its width and thickness slightly inferior to the human. The vascular system of the pig kidney is close to the human kidney, and both have a multipapillary architecture composed of numerous minor and major calyces [4], [6], [7], thus making it ideal as a model for kidney stone related treatments. While the trial treatments are made on living pigs, it is also possible to use a porcine kidney ex-vivo. In 1994, Körmann *et al.* used an explanted, perfused pig's kidney as a mean of damage evaluation following an extracorporeal shock wave lithotripsy treatment [8]. A similar experiment was made in 1998 for damage evaluation following HIFU and SWL treatment in the porcine liver [9], and in 2005 a simpler setup of Bergsdorf *et al.* was proposed as a way to compare different lithotripters [10]. Szyrach *et al.* showed that using kidney from non heart beating donor (i.e. from commercial slaughterhouse) was possible: after a 30 min warm ischemia (typical timing between the death of the animal and the kidney extraction in a slaughterhouse), the kidney is flushed using a 500 mL isotonic NaCl solution with 12.5 kU/L streptokinase and then preserved on ice with Custodiol HTK at $4°C$ [11]. The streptokinase successfully limited the intravascular thrombosis post cardiac arrest and therefore protected the vascular integrity of the kidney. Compared to a control group exposed to a much shorter warm ischemia, some mild change in structural integrity in the cortex was observed and was less pronounced in the medulla. The kidney is then perfused 2 to 6 hours after explantation. The main advantages of using kidney

from commercial slaughterhouse is that there are inexpensive compared to laboratory animals and do not require ethical committee evaluation.

2.3 Kidney stones

2.3.1 Prevalence and pathophysiology

Kidney stones (also referred as urolithiasis or nephrolithiasis) can be found in the kidney (in calyces or the pelvis, and a staghorn stone will fill multiple calyces), in the ureter or in the bladder, as shown in fig. 2.3. The prevalence of kidney stones in the United States is about 8.8% [12], with men having a statistically higher risk of contracting kidney stones than women (10.6% against 7.1%). The risk of having kidney stones also increases with the age and weight of the person. One observation made during the cited study is the dramatic increase in prevalence of kidney stones compared to older studies, as those statistics are 63% higher than 16 years before. Patients that already has formed a kidney stone are aslo at high risk of recurrence, at around 50% after 10 years [13].

FIGURE 2.3: Location of kidney stones in the urinary system [14].

Kidney stones are the results of inorganic and organic residues mixed with proteins, often starting as microscopic nuclei that can rapidly aggregate into large clumps [15]. The majority of the stones are calcareous with more than 80% of the stones treated, then struvite (10%), uric acid (9%) and other stones like cystine are much rarer (around 1%) [14], [16]. The different types of stones with their prevalence are shown in table 2.1. Kidney stone formation can be the result of one or multiple factors, divided as genetic predisposition [17], dietary and metabolic [18]–[20]. The rise of incidence of kidney stones in the world in the last decades has been linked to the rise of type-2 diabetes, which itself is directly linked to the rise of obesity [21].

While the causes for kidney stones formation are wide, one factor that increases greatly the risk of incidence of all kinds of kidney stones is low urine volume per day (due to either low intake or loss of water), since the important factor in stone formation is the concentration of crystallizing solutes in the urine rather than its amount.

2.3.2 Mechanical properties

Kidney stones are considered as brittle [22], meaning that their elastic and plastic deformation is very small before failure. Therefore, they are more likely

TABLE 2.1: The different types of stones and their prevalence [16].

Stone composition	prevalence
Calcium oxalate-monohydrate	40-60%
Calcium oxalate-dihydrate	40-60%
Calcium phosphate (apatite)	20-60%
Calcium phosphate (brushite)	2-4%
Uric acid	5-10%
Magnesium ammonium phosphate (struvite)	5-15%
Cystine	1-2.5%
Ammonium urate	0.5-1%
Mixed calcium oxalate-phosphate	35-40%
Mixed uric acid-calcium axalate	5%

to break under tensile and shear stress than compressive stress due to the presence of numerous micro cracks in their structure [23]. For breaking the stones into fragments, the expansion and coalescence of those microcracks is required, making the stones sensitive to cyclic stress. The mechanical properties of stone made of cystine, calcium oxalate monohydrate (COM), brushite and COM, uric acid, apatite (CA) with calcium oxalate dihydrate and magnesium ammonium phosphate (MAPH) were determined [24] and are listed in table 2.2.

TABLE 2.2: Material properties of kidney stones [24].

Stone mass composition (%)	Fracture toughness (MPa/m)	Density (kg/m^3)	Longitudinal wave speed (m/s)	Transverse wave speed (m/s)	Vickers hardness (GPa)
Cystine (100)	high	1624 ± 73	4651 ± 138	2125 ± 9	0.238 ± 0.014
COM (100)	0.136 ± 0.021	2038 ± 34	4535 ± 58	2132 ± 25	1.046 ± 0.088
Brushite (95)/COM (100)	0.119 ± 0.030	2157 ± 16	3932 ± 134	1820 ± 22	0.727 ± 0.148
Uric acid (100)	0.090 ± 0.028	1546 ± 12	3471 ± 62	1464 ± 12	0.312 ± 0.044
CA (95)/COD (5)	0.057 ± 0.003	1732 ± 116	2724 ± 75	1313 ± 20	0.556 ± 0.170
MAPH (90)/CA (10)	0.056 ± 0.003	1587 ± 68	2798 ± 82	1634 ± 25	0.257 ± 0.080

All the stones except the cystine one presented a brittle behavior. Of all the brittle stones, the COM stone is the strongest one, with both high elastic and

hardness properties, while the MAPH/CA stone is the weakest.

2.3.3 Model stones

Artificial kidney stones play an important role in research as a tool for a better understanding of the fragmentation process of the different treatment but also as a tool to compare the efficiency of each treatment. Most of the first model stones were made of plaster of Paris, which yield stones having mechanical properties in the range of human kidney stone, however the properties variability between plaster providers and even between each plaster provider batch make it unreliable. Nowadays, two model stones are widely used in kidney stone treatment research: the BegoStone [25] which uses a plaster for dental application and yields mechanical properties close to the COM stones (the hardest and most common stones), and the Ultracal-30 [26] which is a gypsum-based cement and has mechanical properties close to uric acid/MAPH stones. The plaster/water ratio of the BegoStone can also be modulated in order to obtain mechanical properties closer to other stones [27].

2.3.4 Diagnosis and localization

The main symptom of kidney stones is renal colic, an excruciating pain in the lower abdomen, that progresses as the stone moves from the kidney down the ureter [28]. The list of symptoms in relation to the position of the stone are listed in table 2.3.

TABLE 2.3: The symptoms of kidney stone [28].

Stone location	Symptoms
Kidney	Vague flank pain, hematuria
Proximal ureter	Renal colic, flank pain, upper abdominal pain
Middle section of ureter	Renal colic, anterior abdominal pain, flank pain
Distal ureter	Renal colic, dysuria, urinary frequency, anterior abdominal pain, flank pain

The localization of the stone can be realized using various techniques, the most common being computed tomography (CT) scan, radiography and ultrasound imaging. If the patient has no history of kidney stones, the best way to determine if the acute flank pain is caused by a kidney stone is a CT scan [29]. The CT scan has a sensitivity and a specificity both around 95-100% [30], [31] and can estimate efficiently the size of the stone [32] and its composition [33], both very important factors in choosing which treatment is more efficient for the stone management. Plain radiography has a relatively low sensibility and specificity (47% and 70%, respectively) [34], and some stones, such as uric acid stones, are

radiolucent (i.e. transparent to x-rays). Finally, ultrasound imaging has a low sensibility but high specificity (19% and 97%, respectively) [35], with the outcome being mostly dependent on the BMI (body mass index) of the patient, but also on the type and size of stone. The stone is shown on CT scan and radiography as a clearer region, similar to bones, while on ultrasound the detection is mostly made by detecting the 'shadow' on the image generated by the stone high acoustic impedance.

During the last two decades, a new method using color-Doppler ultrasound, called the "twinkling artifact", has been developed to help the detection of kidney stone. It was first presented in 1996 as a mean to detect granular structures inside the body [36], and was first applied to kidney stone localization in 1998 [37]. The twinkling artifact manifests itself as rapidly changing colors around the hard object on color-Doppler imaging, and is caused by micro-bubbles trapped in the cracks and cavities of the stone [38]. The twinkling artifact yields a much higher sensitivity than classical ultrasound imaging, 55% against 19%, and also a very high specificity of 99% [39]. Still, to this day CT scan stays the gold standard for kidney stones diagnosis. Different imaging techniques of one stone are shown in fig. 2.4.

FIGURE 2.4: Different images of a kidney stone from [39]. a) Ultrasound imaging: the stone leaves a recognizable "shadow" behind itself. b) Twinkling artifact: trail of changing colours behind the stone. c) CT scan: stone identifiable as it is hyperechoic in the kidney.

2.3.5 Management of the stones

The objectives of the treatment of a kidney stone are to alleviate symptoms, remove the stone and prevent recurrence. The management will depend on the type of stone, its size and location. As in most cases the treatment is not immediate but days after the diagnosis of the stone, the management of the renal colic is done using antibiotics to prevent infection, anti-inflammatory to reduce local edema, and paracetamol to raise the pain threshold while waiting for stone removal [40].

If the stone is smaller than 5 mm it should pass spontaneously through the ureter [41], but larger stones require external actions to be removed. While open surgery was the main treatment for removing kidney stones, it has been almost

completely replaced by less invasive methods, namely ureteroscopy and extracorporeal shock wave lithotripsy for stones smaller than 2 cm and percutaneous nephrolithotomy for bigger stones.

Ureteroscopy, also called intracorporeal lithotripsy, consists of an endoscope with different tools to extract and break the stones. The fragmentation of the stone is realized by repeatedly generating shock waves at close proximity of the stone, either by using a pneumatic lithotripter, an electrohydrolic lithotripter, or laser lithotripters. Nowadays, with the progress of fiber optics, the fragmentation is made mostly using a laser, where two parameters are at play: the frequency of the repeated shock and the power of each shock, and acting on those parameters yields different results with both advantages and disadvantages [42]. The main advantages in favor of intracorporeal lithotripsy is a very high stone free rate (near 90-97%)[43], [44], treatments of stones of up to 3 cm possible [45], effective treatment of morbidly obese patients, and is the safest treatment for patient on anticoagulant [46], while the disadvantages are often long treatment time, the majority of the treatment made under general anaesthesia, and its invasiveness relatively to extracorporeal lithotripsy.

Percutaneous nephrolithotomy is used only in the case of very large stones ($>$2 cm), extremely dense stones, very high quantity of stones, or staghorn stones (stones that fill a large part of the kidney). The operation, which requires general anaesthesia, consists of a sheath place into the kidney to allow the passage of a nephroscope for the fragmentation of the stones using the same technologies as the ureteroscope, and then to allow the succion of the fragments [47]. This method also generates a high stone free rate (near 100%), but also has a high complication rate compared to the other minimally invasive methods [48], and as such is generally used only in extreme cases. Extracoporeal shock wave lithotripsy, being the main subject of this thesis, is described extensively in the next section.

2.4 Extracorporeal shock wave lithotripsy

Extracorporeal shock wave lithotripsy (ESWL or SWL) was introduced in the early 1980s [49] and is the most common treatment for removing kidney stones [50]. It is a non invasive method where very high amplitude acoustic shock waves generated outside the patient body are focused toward the kidney stone in order to break it. A complete shock wave lithotripter system requires a system to localize the stone to be treated and position the patient accordingly, and a shock wave generator. The localization systems used are X-rays and ultrasound, that are typically used in combination, and the positioning can be made by either moving the generator or the patient. A complete extracoporeal shock wave lithotripter system is shown fig. 2.5.

FIGURE 2.5: The Sonolith® i-sys lithotripter, EDAP-TMS, is composed of a C-arc X-ray for the rapid localization of the stone inside the body, but also have the option to use ultrasound imaging to follow the stone during the treatment. The shock wave generator is electroconductive and the patient is positioned by moving the table.

2.4.1 Shock wave generators

The shock wave generator can be electroconductive, electrohydraulic, electromagnetic or piezoelectric. In the case of the electroconductive and electrohydraulic generators (see fig. 2.6(a)), the shock wave is generated by discharging a very high voltage (around 10 to 30 kV) between two electrodes facing each other at a small distance, usually in the order of a few millimeters and immersed in a liquid, either water for the electrohydraulic generator or a conductive liquid such as a mix of salt water for the electroconductive generator. The spark provoked by the discharge of the high voltage generates a shock wave in water at the first focus of an semi-ellipsoid reflector which is therefore focused at its second focus, where the kidney stone should be. The electrodes wear off after each discharge, much more so in water (electrohydrolic) than in a conductive liquid (electroconductive), increasing progressively the gap between them, and thus need to be replaced after a determined number of sparks. Also, as the electrodes wear off, the spark might slightly change its position inside the ellipsoidal reflector, and as a result might dramatically decrease the pressure level at the second focus and thus the efficiency of the treatment. These types of generators are the most common in commercial lithotripters as they were the first technology to be developed for ESWL. In the electromagnetic system, the initial shock wave is generated using a loudspeaker-like system by sending a short electrical pulse into a coil to move a metal plate that then generates an acoustic wave. This acoustic wave can be focused toward the kidney stone by using a parabolic reflector (see fig. 2.6(b))

or a lens [51]. In the piezoeletric generator (fig. 2.6(c)), a 2D array of piezoelectric elements is tied to a spherical structure, focusing the shock waves of each element to the center of the sphere. A typical shock wave, measured at the focus point of an electrohydraulic generator, is presented fig. 2.6(d)[52].

FIGURE 2.6: Different shock wave generators [52]: (a) electrohydraulic generator; (b) electromagnetic generator; (c) piezoelectric generator; (d) a shock wave generated by a Dornier HM-3 electrohydraulic generator.

The first peak (compression) pressure is usually called 'P+', and can vary between 30 and 110 MPa while the second peak (tensile trail) pressure is called 'P-' (or sometime 'PNP', for peak negative pressure) and is usually comprised between -5 and -15 MPa [52]. The shock waves of electrohydraulic and electroconductive generators have low reproducibility whereas they are very reproducible for electromagnetic and piezoelectric ones. Also, both electromagnetic and piezoelectric shock waves are not completely a single pulse, as often a few trailing pulses of lower amplitude are seen behing the initial shock, whereas a single shock wave pulse is effectively delivered for the other generators.

In the first generation of lithotripters, the transmission of the shock wave into the body was made by using a water bath: the patient and the generator were immersed into degassed water, and thus the transmission was made directly from the water to the body, as its soft tissues have acoustic impedance very close to that of water, allowing maximum acoustic transmission. Nowadays, the transmission is made through a thin membrane covered with coupling agent that closes the shock wave generator and can be filled or emptied with degassed water to place the focus at the correct position inside the body.

Other kinds of lithotripsy generators were notably made for research purpose. A generator consisting of a 2D array of piezoelectric transducers, where the focus can be steered electronically, was also presented [53], [54] and time-reversal technique [55] can also be used to track and focus a stone inside the body [56], [57], but the number of piezoelectric elements needed to obtain high-amplitude shock wave and the electronics they involve render them not cost worthy for commercial applications. More recently, works on one-bit time-reversal method combined with multipe scattering [58]–[60], a waveguide [61], [62], or a chaotic cavity [63], [64] showed promises for electronically focused lithotriper, by using fewer piezoelectric elements and being electronically simpler than a classical

time-reversal generator. Also, progress in the field of meta-materials could potentially simplify the electronics behind phased array [65].

2.4.2 Mechanisms involved in ESWL stone comminution

To this day, a complete understanding of the mechanisms implicated in stone fragmentation by SWL remains uncertain. Still, some mechanisms were identified, as spallation, shear stress, squeezing and cavitation.

Spallation

As presented in 2.3.2, kidney stones are made up of brittle materials, full of small microcracks that can expand, nucleate and generate failure lines when exposed to tensile and shear stress [23]. This property makes the stones particularly sensitive to cyclic stress, like in shock wave lithotripsy where they are exposed to repeated stress as an average of 3000 shock waves are used in clinical treatments [66]. Due to the shock wave waveform, the compressive stress is preponderant when the shock wave hits and propagates through the stone. But when the wave inside the stone reaches a boundary, most of the compressive wave is reflected as a tensile wave (Hopkinson effect) due to the high impedance difference between the stone and the urine/tissues, which is then added to the negative trail of the shock wave. Thus, a high amplitude tensile stress is present near the distal boundary of the stone and fragmentation occurs in this area. This phenomenon is illustrated in fig. 2.7

While the spall failure is mostly happening on the distal boundary of the stone due to the partial reflection of the very high compressive stress into a tensile stress, the whole stone is also exposed to the tensile trail of the shock wave, which can also generate fragmentation on cracks naturally present inside the stones. As the stones are often inhomogeneous and with voids present in their structure, partial tensile reflection of the compressive wave also happens locally around these, potentially participating in the fragmentation as well.

Shear stress

Kidney stones, by their composition of brittle material maintained together by a protein matrix, have a very low resistance toward shear stress [67]. Shear waves are generated in the stone as the shock wave passes trough the stone and their impact is dependent of the shape of the stone [68], [69]. In the case of highly focused lithotripter, high shear stress values will also be present, in solid/tissues only, at the focus due to the high gradient of compressive pressure at the focal area.

Squeezing

The sound speed inside the kidney stone is much higher than in water, urine and tissues, with a longitudinal wave speed between 2700 m/s and 4700 m/s (see table 2.2) compared to $\sim$1500 m/s, meaning that the shock wave in the

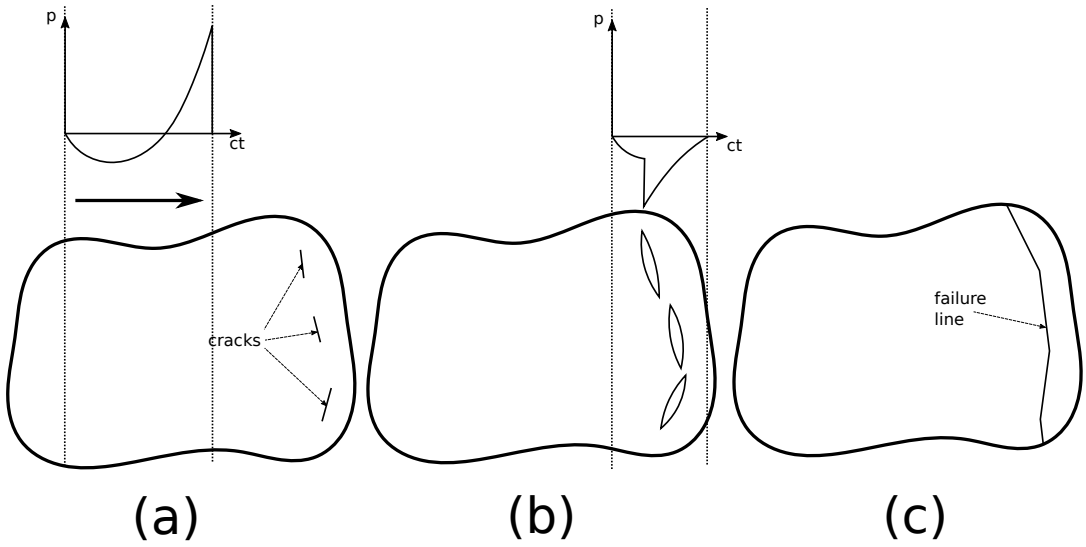

FIGURE 2.7: Illustration of the spall failure model. (a) The shock wave travels inside the kidney stones from left to right. (b) The compressive part of the shock wave is partly reflected as a tensile stress, due to the impedance of the stone being higher than water/urine/tissues (Hopkinson effect), on the distal boundary of the stone and is then added to its tensile trail. The microcracks exposed to this tensile stress open, irreversibly expand and nucleate. (c) After multiple shock waves, the cracks form a fracture line close to the distal boundary, resulting in the fragmentation of the stone.

fluid/tissues surrounding the kidney stone is at a different position that the shock wave inside stone. The squeezing mechanisms imply that the lateral pressure of the shock wave that propagates in the surrounding urine/tissues around the stone exerts enough stress to break the stone [70]. This means that the shock wave, and therefore the focus of the lithotripter, is large enough to encapsulate the stone. The quasi-static squeezing theory [70] postulates that the shock wave surrounding the stone generates a hoop stress inside the stone, effectively 'squeezing' it, and as a results the stone breaks under fatigue due to the coalescence of the micro-cracks naturally present. An illustration of this phenomenon is shown in fig. 2.8

According to another squeezing theory, the dynamic squeezing [71], [72], the shear waves inside the stone are initiated when the shock wave hit the corners of the stone and then reinforced by the lateral pressure of the shock wave outside the stone generating a high tensile stress concentration at about one third of the distal end of the stone. Numerical and experimental analysis were made to support this theory [72], showing that the first fragmentation occurs close to the numerically found location of the high tensile stress. A numerical simulation of this phenomenon is shown in fig.2.8. These results are also supported clinically, as it was observed that low pressure large focus lithotripter, like the Dornier HM3, the first commercial lithotripter, yielded better results compared to highly focused lithotripters [73], [74].

FIGURE 2.8: Left: quasistatic squeezing fragmentation mechanism [70]. Right: Numerical simulation of the dynamic squeezing inside a cylindrical model stone [72], where the negative values are the compressive stress (blue) and the positive values are the tensile stress (red). At t=2 μs, the shock wave inside the stone has already distanced itself from the shock wave in water, and generates shear stress that propagates toward the axisymmetric axis of the stone. At t=4 μs, high tensile stress is generated by the longitudinal wave in the surrounding liquid (dynamic squeezing). The spallation phenomenon is also observable on the distal part of the stone, and is less preponderant that dynamic squeezing. at t=5 μs, the high tensile region is the result of the dynamic squeezing, with also a contribution from the reflected tensile wave of the spallation.

Cavitation

The negative pressure trail of the shock wave induces a rapid growth of the small bubbles naturally present in the water/urine. After a while, these bubbles will violently collapse, creating a strong microjet that can damage the surface of the kidney stone [75], [76]. The collapsing of these bubbles causes erosion at the surface of the stone, yielding small sized fragments (radius inferior to 1-2 mm) [77]. The importance of cavitation in stone comminution was underlined when SWL was performed *in vitro* in water and in castor oil (which has the property of inhibiting cavitation at ESWL pressure levels) [77]. After the same number of shock waves, the same type of model stone treated in water was fragmented in much smaller pieces than the ones in castor oil, which lead the authors to conclude that there is a synergy between stress waves inside the stone and cavitation: stress waves break the stone in large fragments that are then reduced by cavitation to a sub 2 mm size. The same conclusion was obtained when combining SWL with histotripsy (a method that uses cavitation to destroy tissues) [78]. The cavitation in lithotripsy is usually the result of the collapse of a large bubble cluster instead of multiple individual bubbles, generating crater shaped holes on large surfaces of the stone [79]. Photographic time series of the collapse of a bubble cluster and a photo of its subsequent damages on the stone are shown in fig. 2.9

FIGURE 2.9: Photographs of cavitation on model stones [79]. (a) High speed photographic time series of the collapse of a bubble cluster on the proximal face of a model stone. (b) Resulting damages on the proximal face of the stone after 50 shock waves.

2.4.3 Limitations of ESWL

While being widely used around the world, extracorporeal shock wave lithotripsy presents some limitations, some of which have solutions that are not commonly implemented in modern commercial lithotripters.

Motion of the stone

During the treatment of the stone using shock wave lithotripsy, the stone can move due to the respiratory motion or discomfort of the patient, or even after receiving the shock wave itself. A small cyclic motion of the stone has been found to reduce dramatically the efficiency of shock wave lithotripsy [80]. Efforts have been made to improve tracking of the stone during treatment, by either using real time localization [81]–[83], time-reversal piezoelectric generator using the reflected wave on the stone [57] or the cavitation bubbles [84] to refocus after each shot, resonant scattering of the shock wave after hitting the stone [85] or a piezoelectric lithotripter that has the ability to operate in pulse/echo mode to verify if the stone is present at its focal before firing the shock wave [86].

Side effects of ESWL

Even if shock wave lithotripsy is considered as a non invasive procedure, shock waves are known to have side effects on the kidney and the tissues around it [87], [88] and even the residual fragment of the treated stone can lead to some complications like recurrent kidney stone formation [89]. A non extensive list of clinical acute side effects of ESWL includes: hematomas, hematuria, partial to total ureteral obstruction, arrhythmia and pancreatitis. The injuries caused by SWL can also result in the long term to the loss of functional renal mass [90] and new onset of hypertension [91]. Similar to the mechanisms of the stone comminution, the mechanisms of tissue damages are not fully known. The shock wave generated by a lithotripter has been proved to cause cell lysis (rupture of the membrane

of the cell, resulting in its death) [92], [93], and shear stress due to tissues heterogeneity results in tissue lesions [94]. But what may be the main cause of tissue injuries is cavitation [95]–[97] that, while being efficient at reducing kidney stones into very small fragments, is also very efficient for tissue destruction. The damage caused by SWL to the kidney can be linked to the number of shock waves delivered [98] and to their amplitude [99]. Shock waves trigger a protective response by the kidney, and a pretreatment of a few hundreds of low amplitude shock waves, followed by a pause of 3 to 4 minutes before the real SWL treatment begin, can greatly reduce the damage caused to the kidney [100]. Keeping the shock wave pulse repetition frequency inferior to 0.5 Hz also proved to greatly limit the damage caused to the kidney [101].

Pre-focal cloud cavitation

While cavitation at the boundaries of the stone is important for the stone comminution as discussed earlier, if a bubble cloud is located before the focal of the generator (which should be coincident with the kidney stone), it will dramatically affect the amplitude of the pressure of the shock wave and therefore greatly diminish or even remove the cavitation effect on the stone [102]. A bubble hit by the negative trail of the shock wave will expand until collapsing into a cluster of micro-bubbles [103], and if this cluster is hit again before completely dissolving, it will yield an even bigger cluster of bubbles and eventually absorb the totality of the negative pressure of the shock wave while reflecting its compressive part [104]. Since these micro-bubbles have a short lifespan (inferior to one second), it is recommended to use a pulse rate frequency (PRF) inferior or equal to 1 Hz [102], [104], [105]. A low amplitude "bubble removal pulse" burst can also be used between each shock wave pulse to stimulate the coalescence of the bubbles and thus greatly reduce the lifespan of the bubble cloud [106], [107].

SWL resistant stones

Shock wave lithotripsy success depends heavily on the composition, location and size of the stones to be treated [32], [108]–[110]. Stones of high density or composed of cystine have a low probability to be fragmented enough to be naturally eliminated if treated with SWL, and large COM stones (>2 cm) are unlikely to be fully treated in one session of ESWL. One way to prevent this kind of situation is a proper diagnostic, by using CT imaging [32], [33], or maybe supersonic shear imaging [111]–[113], and to use a more invasive technique than extracorporeal shock wave lithotripsy to treat such stones. An *in vitro* study was also made to estimate (up to 1 mm precision) the size of the stone using a small (1.2 mm in diameter) 2 MHz hydrophone [114].

2.4.4 Recent progress and evolution in extracorporeal lithotripsy

In the last two decades research on extracorporeal lithotripsy evolved, mostly by changing the number of pulses sent, their repetition frequency (PRF) and their

intensity. The application also widened, with the emergence of histotripsy, a method similar to shock wave lithotripsy but focused on tissue removal.

Histotripsy

Histotripsy uses mechanical effects (mostly cavitation) to liquify tissues using short high pressure acoustic pulses with low PRF, similar to lithotripsy, and was developed as an alternative to the non-invasive thermal ablation of living tissues realized by HIFU (high intensity focused ultrasound) [115]–[119]. The main advantage of histotripsy over HIFU thermal ablation is the immediate removal of tissue rather than the production of thermal coagulation necrosis.

Histotripsy uses transducers with a center frequency around 0.5-1 MHz, and sends bursts of ultrasound pulses with a low duty cycle (around 2 to 20 cycles), with a peak negative pressure in the range of 12 MPa to 25 MPa and a peak positive pressure that can be greater than 50 MPa, and the low PRF, allows the thermal effect in the body to be negligible [120]. Typical histotripsy bursts are shown fig. 2.10.

FIGURE 2.10: Typical histotripsy bursts [116].

At the focus of the transducer, a dense bubble cloud is created and the resulting cavitation allows tissue removal. But water and water-rich tissues have a cavitation threshold usually higher than the peak negative pressure of the burst wave. For example, for a 2 cycles, 1.1 MHz focused ultrasound pulse, the cavitation threshold of water is around 27 MPa [121]. If the pressure is lower than this threshold, no bubble cloud can be formed with a single shot, however there is a probability of single bubbles appearing sparsely in the focal region. These bubbles then permit the initiation of the dense cloud cavitation: due to non linear propagation, the positive pressure has a much higher amplitude than the negative pressure, giving a very asymmetric waveform, and when the waveform encounters a bubble, a large negative pressure is generated by the backscattering of the shockwave, and thus yields a bubble cloud with a size dependent of the number of pulses per burst (i.e. the duty cycle, see fig. 2.11) [122]. Once the bubble cloud is initiated, the PRF must be high enough so that there is always some residual cavitation nuclei in the focal zone to re-initiate the bubble cloud, which will extend toward the transducer. In order to optimise the probability of cloud cavitation, a cloud of microbubbles can be generated by an initiating sequence, consisting of very high intensity pulses (with a peak negative pressure superior to the cavitation threshold), and then sustain the cloud cavitation using lower intensity pulses [118]. Another way to ensure cloud cavitation at the focus would be to use pulses with very intense peak negative pressure, superior to the cavitation

threshold of the targeted tissue, which can be achieved using second-harmonic superimposition [123], for example.

FIGURE 2.11: Top: The size of the bubble cloud is related to the number of cycles at the focus [122]. Right: (1) the bubble expands in response to the negative pressure, (2) the positive pressure is reflected on the boundary of the bubble as a negative pressure pulse due to the strong impedance difference, (3) the backscattered negative pressure pulse is added to the negative pressure, (4) this very intense negative pressure generates more bubbles behind, and the process is repeated as much as there are cycles [122].

One of the challenges of histotripsy is generating a precise lesion inside the body. Lin *et al.* found that sub-wavelength sized lesions can be obtained by estimating the intrinsic cavitation threshold and controlling the size of the focal beam where the peak negative pressure is superior to the threshold [124], [125]. Using this technique, reproducible lesions as small as 0.9x1.7 mm (lateral/axial) were made. Lin *et al.* also investigated dual-beam histotripsy [126]: a low frequency "pump" of 500 kHz with a peak negative pressure inferior to the intrinsic cavitation threshold and a high frequency probe of 3 MHz were combined confocaly in order to obtain peak negative pressures beyond the intrinsic cavitation threshold, in a similar manner to that of Umemura *et al.* [123]

Cavitation as the main mechanism in stone comminution

The idea of using cavitation as the main mechanism to break kidney stones was first proposed by Ikeda *et al.* [127]. Their idea was to induce cloud cavitation erosion around the kidney stone using a "cavitation control" waveform, *i.e.* using low amplitude/high frequency ultrasound (between 1 and 4 MHz) to generate a cavitation cloud around the stone and then immediately force the collapse of the bubbles using a moderate amplitude (compared to SWL)/low frequency ultrasound (545 kHz) [128]. The cavitation control waveform and the resulting fragmentation process is shown fig. 2.12.

This method showed great results *in vitro*, communiting model and real kidney stones into powder (fragment size inferior to 1 mm) rapidly. A comparison between using only the high frequency pulse, low frequency pulse and the "cavitation control" pulse at a PRF of 25 Hz on model stones during 2 minutes is shown fig. 2.13.

In 2013, Duryea *et al.* investigated the use of SWL and histotripsy combined to produce small fragments in lithotripsy [78]. Their prototype consisted of a

FIGURE 2.12: A "cavitation control" waveform and its working principle as presented in [127], [128].

FIGURE 2.13: The model stones were exposed to 2 minutes at a PRF of 25 Hz to (a) high frequency wave (3.82 MHz) (b) low frequency wave (545 kHz) (c) "cavitation control" waveform [128].

classical electrohydraulic SWL generator with a ring of piezoelectric elements tied to the border and focused at the same focal point of the reflector of the SWL generator. The SWL generator had a typical peak positive pressure P+ of 34 MPa, a peak negative pressure P- of -8 MPa and a PRF of 1 Hz, while the histotripsy module had a peak negative pressure P- of -33 MPa (extrapolated linearly, not mesured) and a PRF of 100 Hz. Five treatment schemes were compared *in vitro*: 10 minutes of SWL and histotripsy interleaved (*i.e.* the histotripsy pulses were sent between each SWL pulse), 10 minutes of SWL then 10 minutes of histotripsy, 10 minutes of histotripsy then 10 minutes of SWL, and finally 10 minutes of SWL and 10 minutes of histropsy isolated for comparison purpose. The results are presented in fig. 2.14.

FIGURE 2.14: Stone fragments size proportion following the different treatment schemes [78].

All of the combined SWL/histotripsy treatments showed better results compared to SWL and histotripsy alone, as they yielded smaller fragments. The best

method was determined as SWL followed by histotripsy, as almost no fragment of a size superior to 6 mm were found afterward. From this, the authors concluded that, during SWL treatments, once the stone was broken in a few fragments, cavitation was the main comminution mechanism. During these experiments, the authors observed the formation of pre-focal cloud cavitation and determined that their results can be improved if the shielding exerted by these bubbles was removed.

Following that conclusion, Duryea *et al.* investigated the use of a "bubble removal pulse" to remove the pre-focal "cavitation memory", responsible of reducing the effectiveness of cavitation erosion on the stone [106], [107]. A separate transducer generating a low amplitude and wide focus ultrasound burst was used on the cavitation cloud resulting of the histotripsy treatment to stimulate the cloud coalescence (fig. 2.15) and therefore shorten greatly the bubbles lifespan.

FIGURE 2.15: The bubble removal pulse [129].

Ultimately, the "bubble removal pulse" was proved to highly increase the erosion caused by histotripsy, up to 7.5 times more than histotripsy performed without it [129].

Ultrasonic propulsion of kidney stones

Ultrasonic propulsion of kidney stones was first introduced in 2010, with a device that could move small stones using ultrasound radiation force inside a tissue phantom [130]. As such, it is not a lithotripsy device as its objective is to move small stones outside the kidney rather than fragment them, however it could easily be used in combination of lithotripsy, as, for example, to clear the kidney of small fragments that could potentially generate another kidney stones after the ESWL treatment. It was then tested with success *in-vivo* on swine models, where stones were moved with less than 2 minutes of ultrasound exposure, but also generated mild thermal damages to the surrounding tissues [131]. As of 2016, ultrasonic propulsion of kidney stones was successfully evaluated in clinical trials [132].

Burst wave lithotripsy

While the lithotripsy system described in [129] was highly focused (2 mm in the lateral directions and 6.3 mm in the axial) to rely mainly on cavitation to fragment the stone, Maxwell *et al.* investigated the use of a wider focused system that could fragment stones combining stress waves and cavitation, called burst wave lithotripsy (BWL) [133]. The pressure waveform consisted in a burst of 10 cycles at relatively low pressure ($<$7 MPa), at three different pulse frequencies (170 kHz, 285 kHz and 800 kHz), at a PRF of 200 Hz and with a lateral focus -6 dB bandwidth of 7.6 mm. Results on both artificial and human small stones (size $<$8 mm) were impressive, with very fast total comminution of the stones. The authors underlined that the fragments size were dependent on the pulse frequency: high frequencies yielded small fragments but required longer treatment times, while low frequency yielded larger fragments after short treatments. Conversely, it was found on *in-vivo* pig model that low frequency implied high kidney damage, while high frequencies are relatively safe compared to ESWL [134]. The use of BWL combined with ultrasonic propulsion to help push the stone out of the urinary tract was also investigated [135].

Chapter 3

Preliminary Experiments

3.1 Introduction

The general objective of this doctoral work was to find and develop an innovative extracorporeal lithotripsy treatment transducer that could potentially be equipped on the next generation of commercial lithotripters of the company *EDAP-TMS*. As this general objective was the only directive of this thesis, a rather long time was consecrated to define properly the different subjects to be worked on. As such, extensive experiments on burst wave lithotripsy, a promising new extracorporeal lithotripsy method that was first published in 2015, were made to evaluate the possibility of dedicating this thesis to this method. Also, an evaluation of the different shock wave lithotripsy technologies used at *EDAP-TMS*, *i.e.* electroconductive and piezoelectric lithotripters, was made in order to look for possible innovations in that area.

3.2 Burst wave lithotripsy

The first paper on burst wave lithotripsy (BWL) was published in 2015 [133], just before this thesis, and as such this new extracorporeal lithotripsy method was investigated at the beginning of this thesis. The focus here was to try to reproduce the results of the original paper and see their limits. In their paper, Maxwell *et al.* sent low pressure bursts of 10 cycles at three different frequencies with a PRF of 200 Hz on both artificial and human kidney stones to break them. The pressure was relatively low, and it was found that a maximum pressure amplitude superior to 2.8 MPa was needed for stone comminution at 170 kHz, but an increase in pressure did not improve the fragmentation significantly. In their experiments, the maximum pressure used was 6.5 MPa. The stones were glued onto a thin, acoustically transparent, membrane and positioned in a way that the focal width at the focus of the transducer was wider than the stones. The artificial stones were BegoStones made according to the paper from Liu and Zhong [25], and were cylindrical with a diameter of 6 mm and length of 10-12 mm.

The artificial stones needed around 9.7 min of BWL exposure to be fully fragmented, and it was found that the maximum size of the fragments were dependent of the frequency used: at 170 kHz, the maximum size was around 3 mm, while at 285 kHz no fragment larger than 2 mm was produced and at 800 kHz

no fragment superior to 1 mm were found. The size distribution of the fragments after BWL treatment is shown in fig.3.1.

FIGURE 3.1: Fragments size after a BWL treatment [133].

For the original authors, the intended objective of the development of BWL was to fragment the stones with the shear waves generated when a stone is exposed to a focus wider than its size, and the low pressure was a important factor to avoid cavitation, which is most likely the main mechanism of tissue damages during ESWL.

From this article, the results were very encouraging and presented a clear evolution from traditional extracorporeal lithotripsy, but all these results were, at the time, *in vitro* and therefore the effect on tissue of such ultrasound exposure were still unknown. After the experiments presented here were made, an article assessing the tissues damages was published, and this *in-vivo* study showed heavy renal damages for low frequency BWL [134].

3.2.1 Experimental setup

The experimental setup was similar to that of the original paper. Here, two different frequencies of focused transducers were used, 180 kHz and 360 kHz, with their focal characteristics given in table 3.1.

TABLE 3.1: -6 dB focal characteristics of the focused transducers

Frequency (kHz)	width (mm)	length (mm)	Max pressure (MPa)
180	8.3	37.7	3.5
360	4.5	21	4.1

The stones were made of plaster of Paris mixed with water with a weight ratio of 10:6, were cylindrical and with two different sizes: large stones had a diameter of 15 mm and a length of 17 mm while the small ones had a diameter of 6 mm and a length of 10 mm (similar, in size, to the ones used by Maxwell *et al*). The stones were placed in degassed water (<2 mg/L O2) at least 12 hours before the experiments. The experiments were made in a tank full of degassed water (<2 mg/L O2) where the stones were glued to an acoustically transparent membrane and placed at the focus of the transducers with a computer numerical control

(CNC) 3-axis positioning. The cavitation photographs were captured using a high speed camera (Phantom V12.1, Vision research, USA).

The stone exposure settings were also almost the same than in the original paper: bursts of 10 cycles were sent at a PRF of 200 Hz at maximum pressure (3.5 MPa at 180 kHz and 4.1 MPa at 360 kHz). During the stone treatment, the fragments were collected in order to determine their size by placing a recipient under the stone.

3.2.2 Results

Small artificial stones

Fragmentation of the small artificial stones (6 mm diameter and 10 mm length) was done with both frequencies. At 180 kHz, the total fragmentation was made in less than 10 minutes, similarly to the original paper. Photos of the fragmentation of artificial stones at 180 kHz are shown in fig. 3.2 and fig. 3.3. In the first case, the stone quickly broke in three large fragments with only a handful of less than 3 mm fragments, while the second figure shows fragments of sizes mostly comprised between 2 mm and 3 mm, but larger fragments were also occasionally observed, as sometimes the stones were not breaking uniformly, *i.e.* from bottom to top, and thus large parts of the stones fell. This is mostly a setup defect rather than a problem with the BWL itself. The different ways of breaking the stones were obtained by changing the position of the center of the focus of the transducer inside the stone: in the case where the stone broke in three large parts, the center of the focus was at about one third of the length to the stone from the distal face, while in the case with the fragmentation in small pieces, the center of the focus was at about one third of the length of the stone from the proximal face.

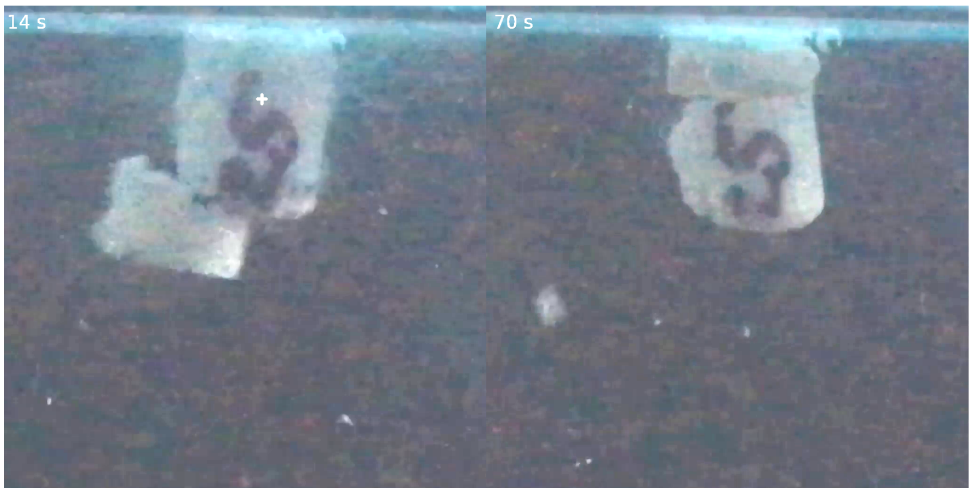

FIGURE 3.2: Example of an artificial stone that quickly broke in 3 parts after exposure to 180 kHz BWL. The white cross in the first photo represents the approximate position of the focus of the transducer. Acoustic propagation from bottom to top.

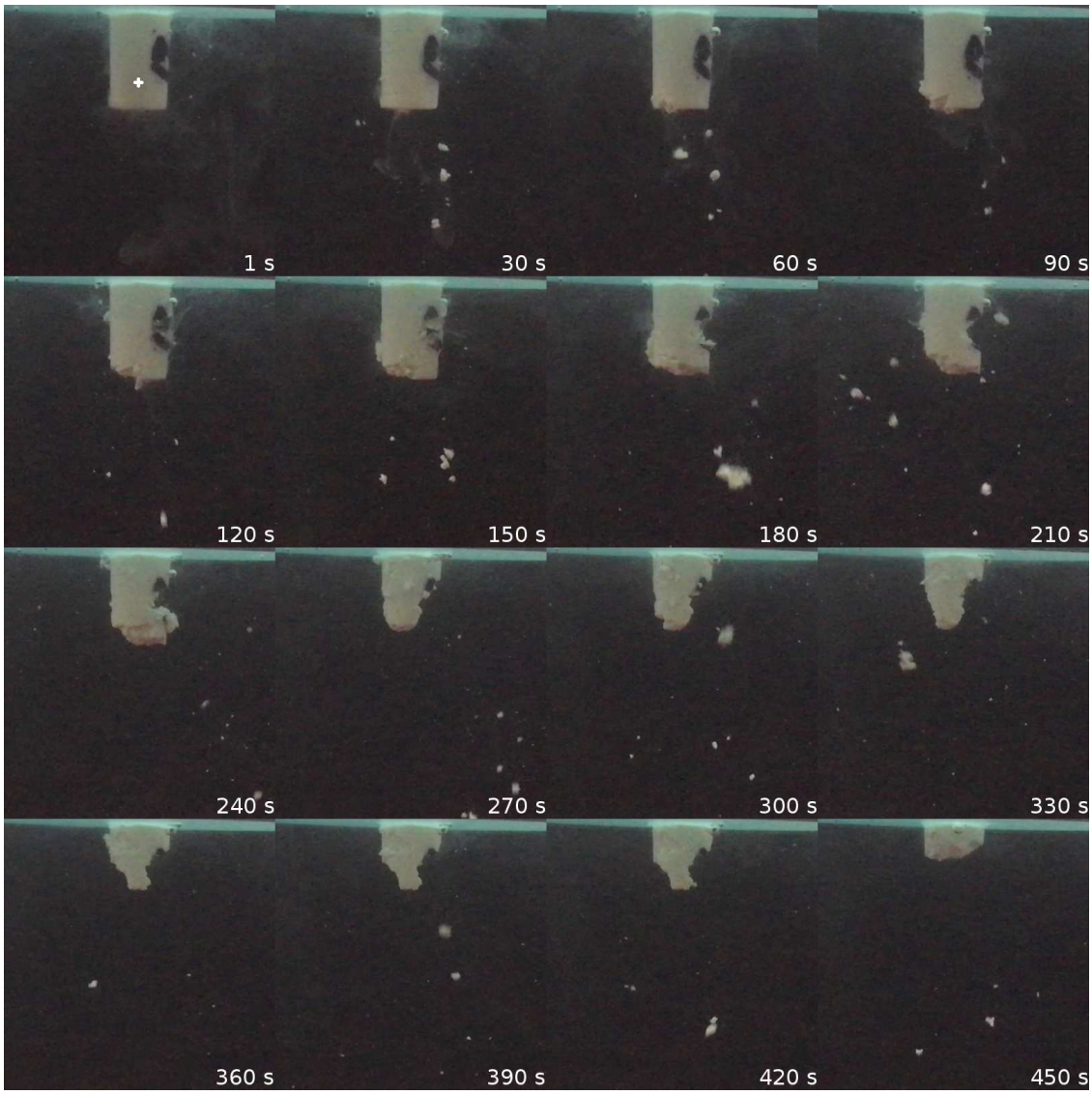

FIGURE 3.3: Photographic time series of the fragmentation of a small artificial stone at 180 kHz. The white cross in the first photo represents the approximate position of the focus of the transducer. Acoustic propagation from bottom to top.

Cavitation was also present during the stone comminution, as shown in the high speed photographs in fig.3.4.

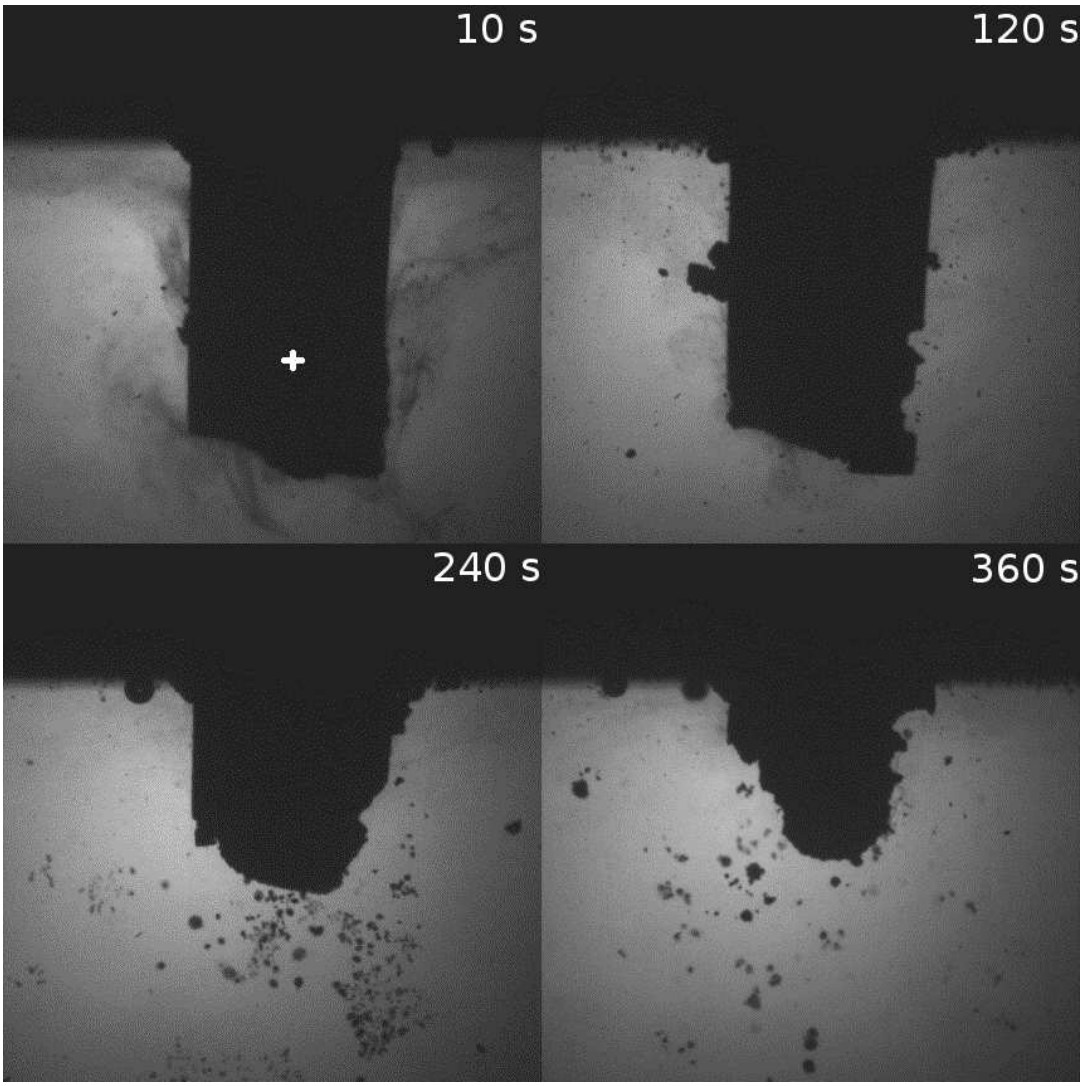

FIGURE 3.4: Photos of the stones during 180 kHz BWL with a shutter speed of 10 μs. The white cross in the first photo represents the approximate position of the focus of the transducer. Acoustic propagation from bottom to top.

At 360 kHz, the width of the focus of the transducer was smaller than the stone itself, and outside small damages caused by cavitation pitting on the proximal face of the stone, no fragmentation was made after more than 10 min of BWL exposure. As the maximum pressure was already close to the lowest limit (2.8 MPa according to the original paper) at the focus, moving the stone behind the focus to have a wider exposure was unfortunately impossible.

Large artificial stone

In this case, the width of the stones (15 mm) was much larger than the width of the focus at both frequencies. This was done to evaluate the importance of the stone size in BWL. As in the case of the small stone exposed to BWL at 360 kHz,

only cavitation pitting damages was seen of the proximal face (in relation to the transducer) of the stone for both frequencies, as seen in fig.3.5.

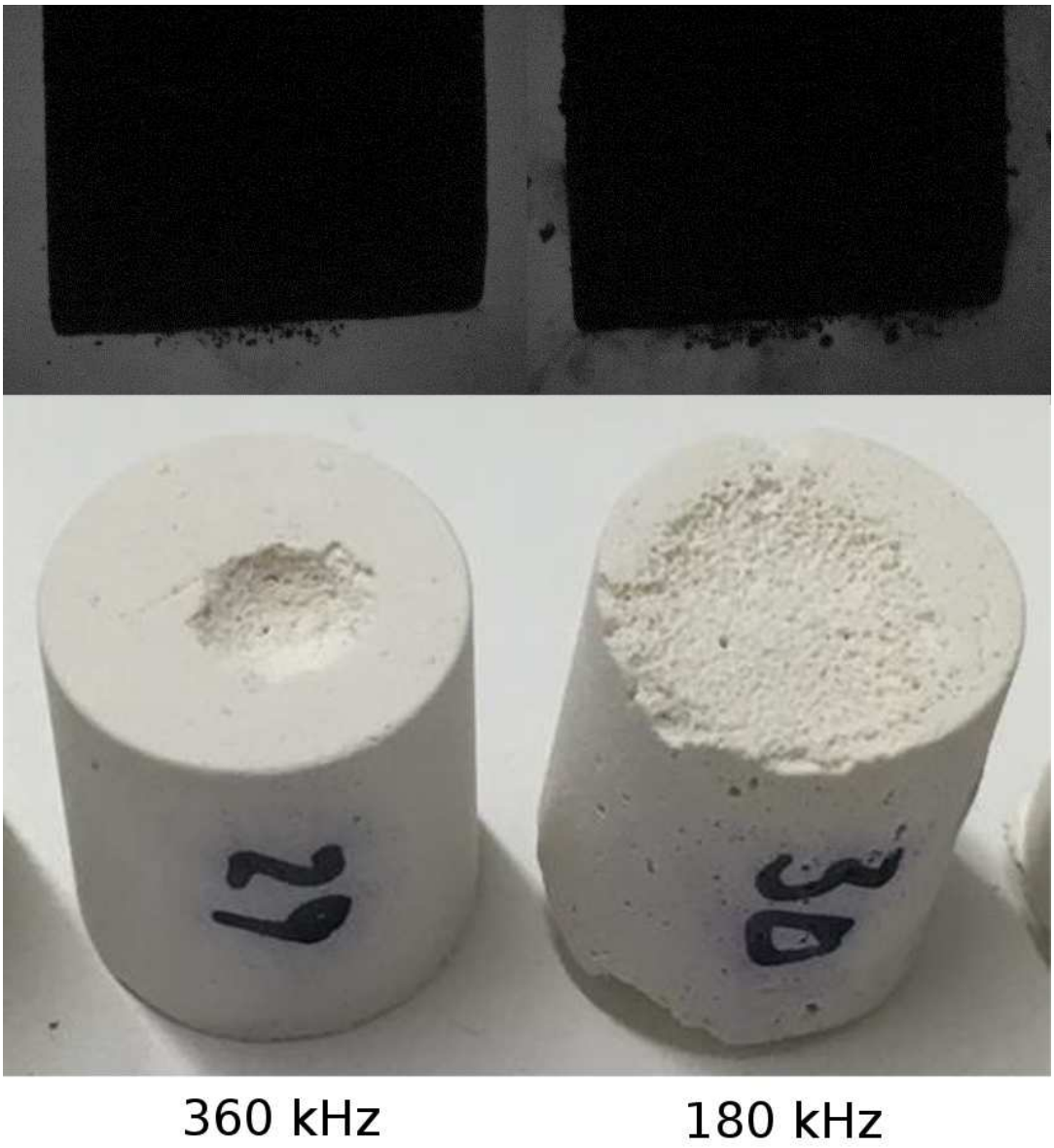

FIGURE 3.5: Top: High speed photographs of the stones during BWL with a shutter speed of 10 μs. Bottom: Photo of the proximal face of the stone after an exposure of 10 min of BWL.

3.2.3 Discussion

In the case of the 180 kHz transducer treating small stones (which have the approximate same size as those of the original papers from Maxwell *et al.*), the fragmentation is occurring as described in the original paper, with some notable observations. First, the way the stones fragment seems to be dependent on the position of the focus in our case, with larger fragments obtained with the focus closer to the distal face of the stone. This may be related to cavitation: as seen

on the high speed photographs and with the cavitation pitting damage on large stones, cavitation is present and the pitting it causes around the stone, *i.e.* in our case on the cylindrical face, may generate cracks that initiate the fragmentation by the stress wave. In the case where the position of the focus is close to the distal face, the cavitation may only happen on the distal side while the proximal side is mostly exposed to stress, meaning that only the cracks naturally present inside the brittle artificial stones are affected, therefore resulting in larger fragments. This show the importance of the cavitation in the burst wave lithotripsy communition process, which was initially sought to be avoided by the authors in order to minimize tissue damage. Recent works acknowledge the presence of cavitation at the focus of the BWL transducer [136].

Second, the ratio between the -6 dB diameter of the focus of the transducer and the size of the stone is a very important factor, as observed here: if the stone is larger than the diameter of the focus, no fragmentation is observable, only cavitation pitting damages on the proximal face. This supports the initial hypothesis from the authors of the original paper that a phenomenon similar to the dynamic squeezing in shock wave lithotripsy [71], [72] is the main factor in stone comminution in burst wave lithotripsy.

Burst wave lithotripsy *in-vitro* experiments show overall very impressive results, with rapid and efficient communition of small artificial (and human) stones. However, the treatment was completely inefficient for stones larger than the -6 dB width of the transducers. The large focal width necessary to treat stones larger than 6 mm can be obtained with piezoelectric transducers by simply setting the stone before the focal point (between the focus and the transducer), which is what Maxwell *et al.* did in the original article for the transducers that did not possess the focus width requirements. But in those areas the pressure amplitude is largely inferior to the one at the focal point, so to compensate the surface pressure of the transducer needs to be much higher, resulting in very high pressure at the focus which will undoubtedly generate heavy tissue damages as its waveform will be close to the one used in histotripsy for tissue ablation. Other solutions to have a large focal width include piezoelectric arrays, which are still too expensive to consider for a commercial lithotripter to stay in the price range of its competitors, as it is the aim in this thesis, and also confocal setups can be considered.

Unless using a setup that allows focal area to have large width without generating high pressure levels, BWL is limited to the treatment of small (1 cm at most) kidney stones. However, shock wave lithotripsy is already very efficient for stones of the same size requirement [40], and can also treat larger stones, albeit with lower success rate. As such, BWL is not yet a total replacement of SWL, but it does present the advantage of a possible handheld and inexpensive small therapeutic transducer that can treat rapidly small stones. This last solution, combined with ultrasonic propulsion, already seems in development by a team composed of the original authors [135].

It is also relevant to note that this method has not yet been approved by the US Food and Drug Administration (FDA), a process that could take years. A recent *in-vivo* study [134] showed high tissue damage at 170 kHz, which was the transducer that had the larger focus width, while higher frequencies seemed safe.

Therefore, burst wave lithotripsy as the main mechanism for stone fragmentation was set aside for next generation of commercial lithotripters. However, seeing how efficient it was for small stones it was not dismissed, and as such a requirement was set that the prototype of this thesis will either be able to generate BWL for small stone treatments, or even try to combine it in some way with classical SWL in order to improve fragmentation, similarly to a combination of histotripsy and SWL [78].

3.3 Shock wave lithotripsy

This section presents both numerical simulations and experiments realized on commercial lithotripters in order to look for potential innovations in the ESWL technology.

3.3.1 Impact of the focal characteristics

Since the beginning of ESWL and its first lithotripter, the *Dornier* HM3, a wide range of commercial lithotripters were made using different shock wave technologies, and each one having a different waveform and focal volume. As presented in the literature review in chapter 2, wide focal volume seems to lead to more efficient stone fragmentation, mostly due to the participation of the dynamic squeezing phenomenon. In the article introducing this phenomenon, the author changed the size of the focal width and concluded that wider focus leads to higher stress inside the stones. Still, many narrow focused lithotripters, which have pressure amplitude at least twice higher than the HM3, presents good results both *in-vitro* and clinically. A comparison of the focal characteristics of the *Dornier* HM3 and the *EDAP-TMS* Diatron 4 (whose commercial name is I-Sys) are shown in table 3.2. While the Diatron 4 focal width is around three times smaller than that of the HM3, its maximum pressure is also around three times higher.

TABLE 3.2: -6 dB focal characteristics of two commercial lithotripters, where t_{FWHMp+} is the time during which the positive pressure exceeds half the maximum pressure

Name	width (mm)	length (mm)	Max pressure (MPa)	t_{FWHMp+} (μs)	Rise time (ns)
HM3-A [137]	10	60	+38.4/-10	0.31	49
Diatron 4	3.1	34.7	+120/-12	0.342	38

In order to compare the impact of both lithotripters on kidney stones, an equivalent numerical modeling to the original article [71] was made. The model was axisymmetric and was implemented in finite element using COMSOL, where the fluid (water) was modeled using linear acoustics equation, the kidney stone was modeled using linear elasticity and the fluid solid interface was realized using surface integrals. The axysimmetrical model did not include a way of absorbing the wave at the boundaries but instead was made large enough to avoid

the boundaries reflections to enter the stone during the time of the simulation. The simulation domain is presented in fig. 3.6 and the numerical modeling is detailed extensively in the next chapter. The maximum element size was 55 μm with second order Lagrange elements and the temporal discretization was 20 ns. The shock wave was set as an initial condition 2 mm away from the proximal face of the stone and the total time of the simulation was chosen in order to allow the wave to fully travel inside the stone and come back to the its proximal face.

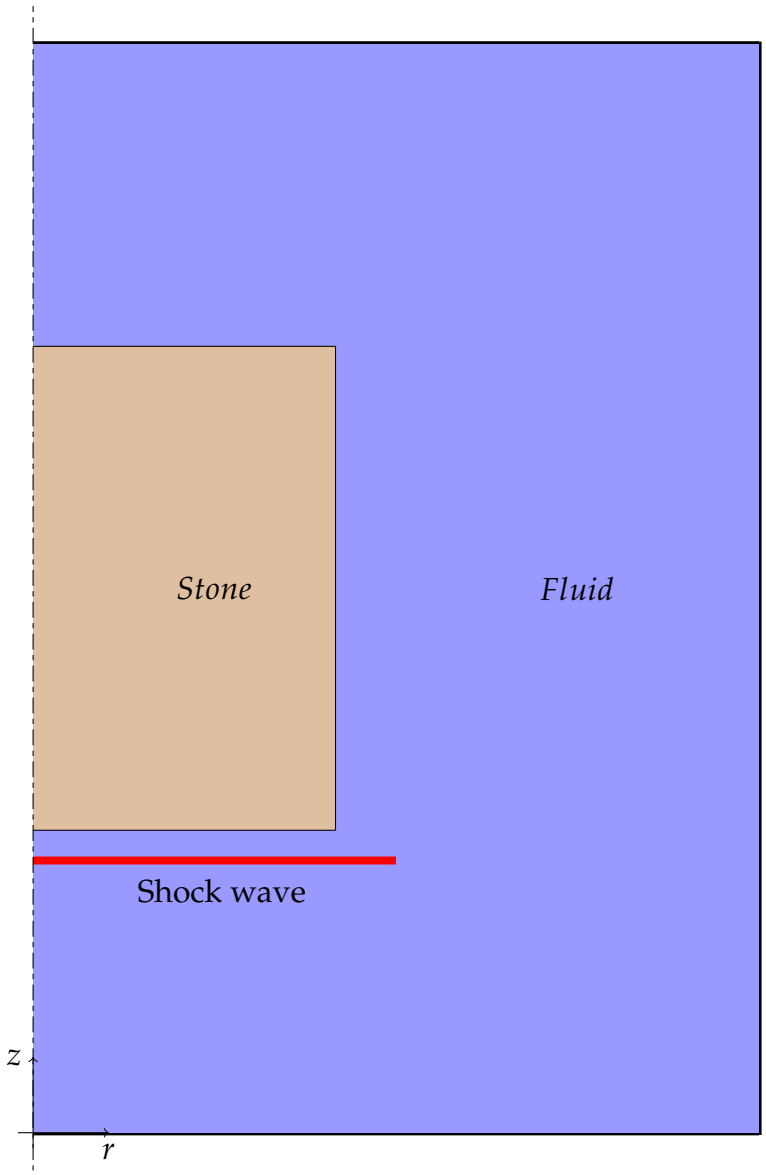

FIGURE 3.6: The simulation domain, where here the stone is cylindrical but can also be spherical.

The stone here is chosen as a Begostone model stone and its material properties for the simulation are given in table 3.3 [25].

The waveform was modeled the same way as in the original paper by using the following equation:

TABLE 3.3: Material properties of the Begostone model stone[25].

Density (kg/m^3)	Bulk modulus (GPa)	Shear modulus (GPa)
2174	30.890	11.221

$$p_s(r,t) = p_0(1 + tanh(t/t_{RT}))exp(-t/t_L)cos(2\pi f_L t + \pi/3)exp(-(r/r_g)^2) \quad (3.1)$$

where t_{RT} controls the rise time, t_L and f_L control the pulse temporal shape, and r_G is the spatial width of the focus. From table 3.2, both shock waves were modeled and are shown in fig. 3.7.

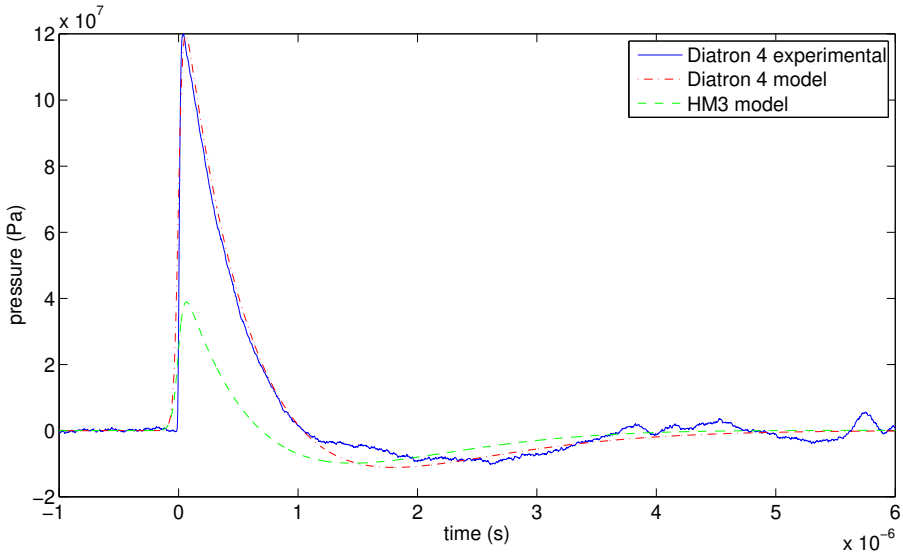

FIGURE 3.7: Shock wave for the Diatron 4 and HM3 lithotripter. —— Diatron 4 shock wave measured with fiber optic hydrophone, -·-·- Diatron 4 shock wave modeled using (3.1), - - - HM3 shock wave modeled using (3.1)

As in the original paper, the maximum shear stress τ and the maximum tensile stress σ_t in the stone are used to evaluate the potential damages that the shock wave can generate into the stone. A comparison of both lithotripters shock waves was made for cylindrical stones of diameter 3 mm to 13 mm, with the cylinder length always 1 mm longer than its diameter, and for spherical stones of diameter between 3 mm to 13 mm. The maximum shear and tensile stress for any instant in relation to the diameter is shown in fig. 3.8 for the cylindrical stones and in fig. 3.9 for the spherical stones.

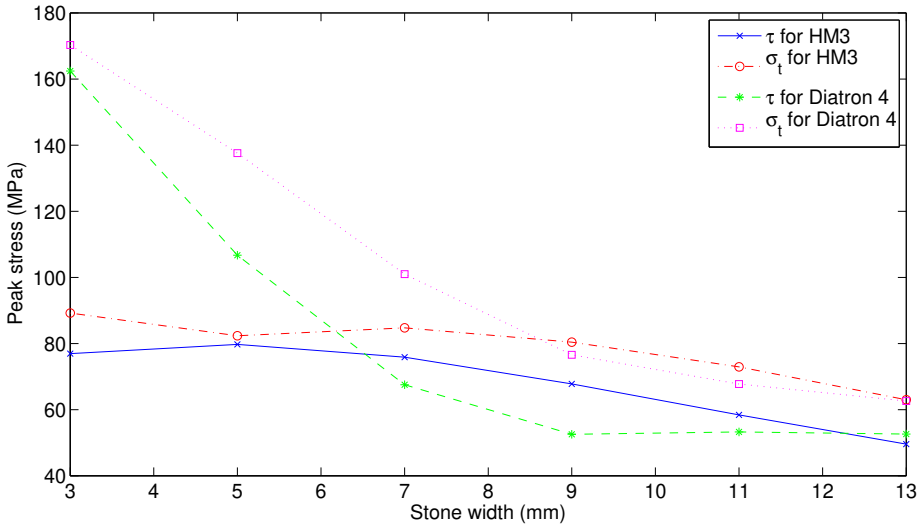

FIGURE 3.8: Peak shear and tensile stresses inside cylindrical stones exposed to HM3 and Diatron 4 shock wave in relation to the width of the stones.

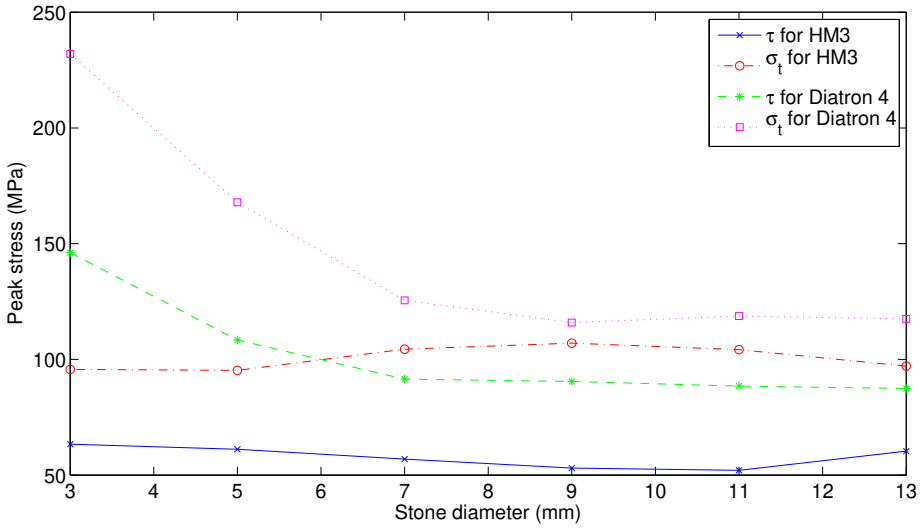

FIGURE 3.9: Peak shear and tensile stresses inside spherical stones exposed to HM3 and Diatron 4 shock wave in relation to the diameter of the stones.

As described originally, the peak shear and tensile stresses do not vary much in relation to the size of the stone when treated with the HM3 shock wave, whereas in the case of the Diatron 4 shock wave the peak stresses are very high for small stones and tend toward similar values than the HM3 for large stones. This is because for small stones, the width of the focus allows the dynamic squeezing phenomenon to happen, which generates very high shear and tensile stresses, while for larger stones, spallation is the main source of tensile stress and the high

pressure gradient of the focus is the main source of shear stress. These phenomena are illustrated in fig. 3.10.

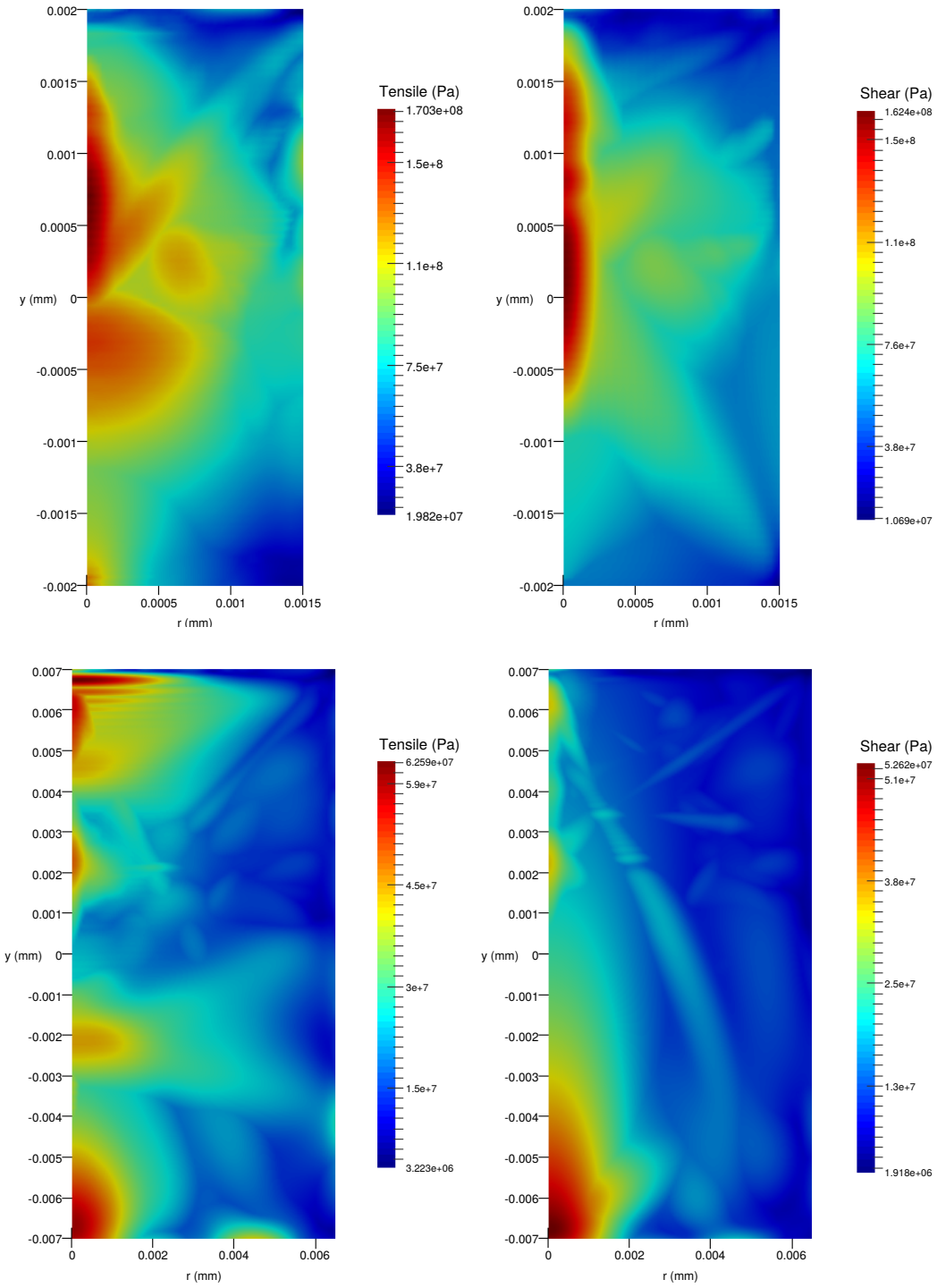

FIGURE 3.10: Maximum peak tensile and shear stresses during treatment a with a Diatron 4 shock wave. Top: cylindrical stone of diameter 3 mm and length 4 mm. Bottom: cylindrical stone of diameter 13 mm and length 14 mm.

In the case of stones treatment with HM3 shock waves, the main cause for the stresses inside the stone is always the dynamic squeezing for every size of stone due to the very large focus width, as shown in fig. 3.11.

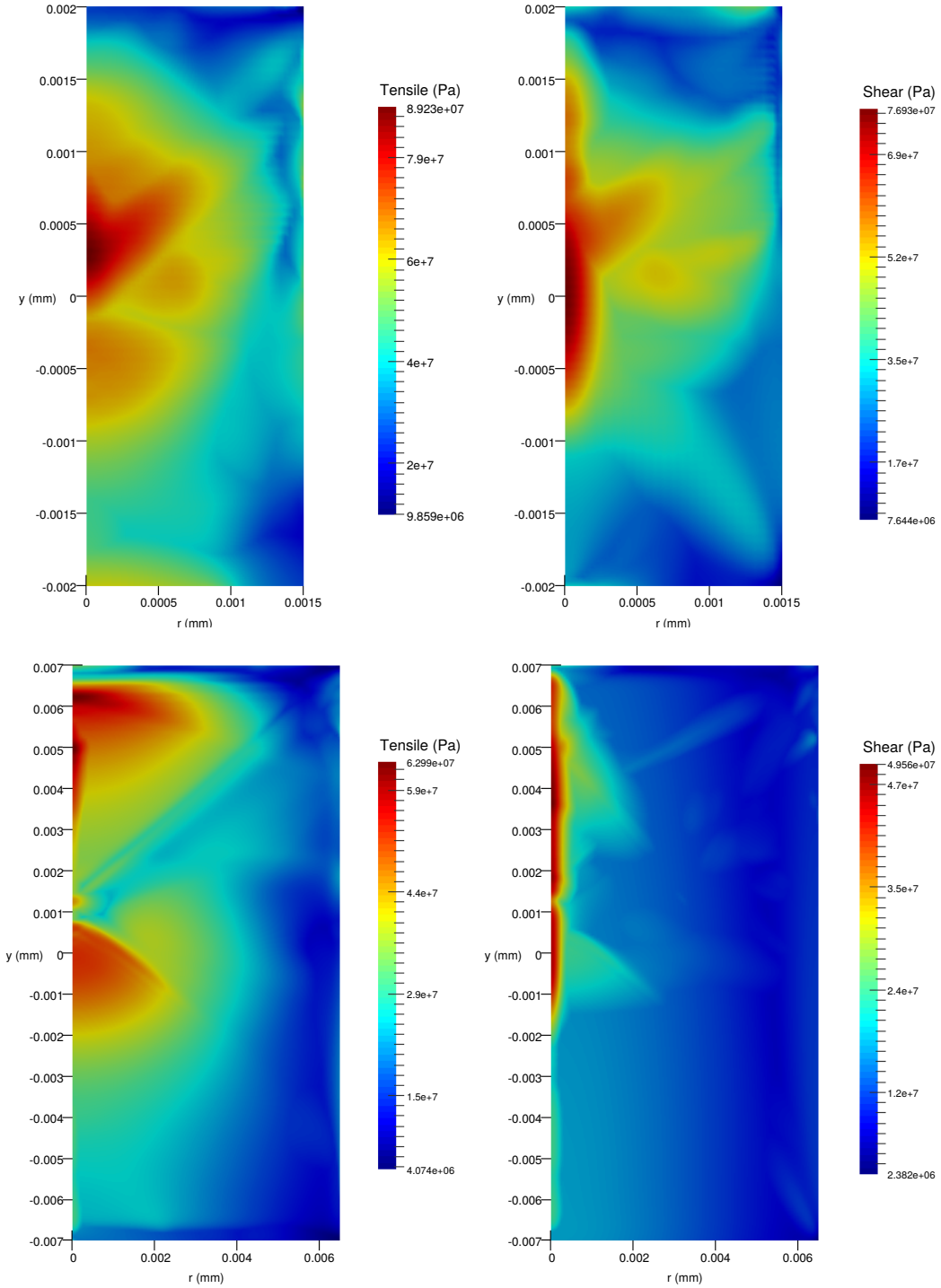

FIGURE 3.11: Maximum peak tensile and shear stresses during treatment with a HM3 shock wave. Top: cylindrical stone of diameter 3 mm and length 4 mm. Bottom: cylindrical stone of diameter 13 mm and length 14 mm.

In terms of peak tensile and shear stresses, the narrow focus high pressure lithotripter (here the Diatron 4) is more advantageous compared to a wide focus low pressure lithotripter (here the *Dornier* HM3) for stones that have a width smaller than about twice its focal width, mostly because in this range the dynamic squeezing phenomenon is happening. For larger cylindrical stones, the differences in terms of stress values are not significant between the two lithotripters, while the narrow focus yields higher shear stress for the spherical stones, as shown in fig. 3.12. However, the HM3 lithotripter yields slightly larger area exposed to high stresses inside the large stones compared to the diatron 4 where most of the stress is concentrated on the distal and proximal faces of the stones, as seen in figs. 3.10 and 3.11, which may play an important role in the fragmentation of the stone.

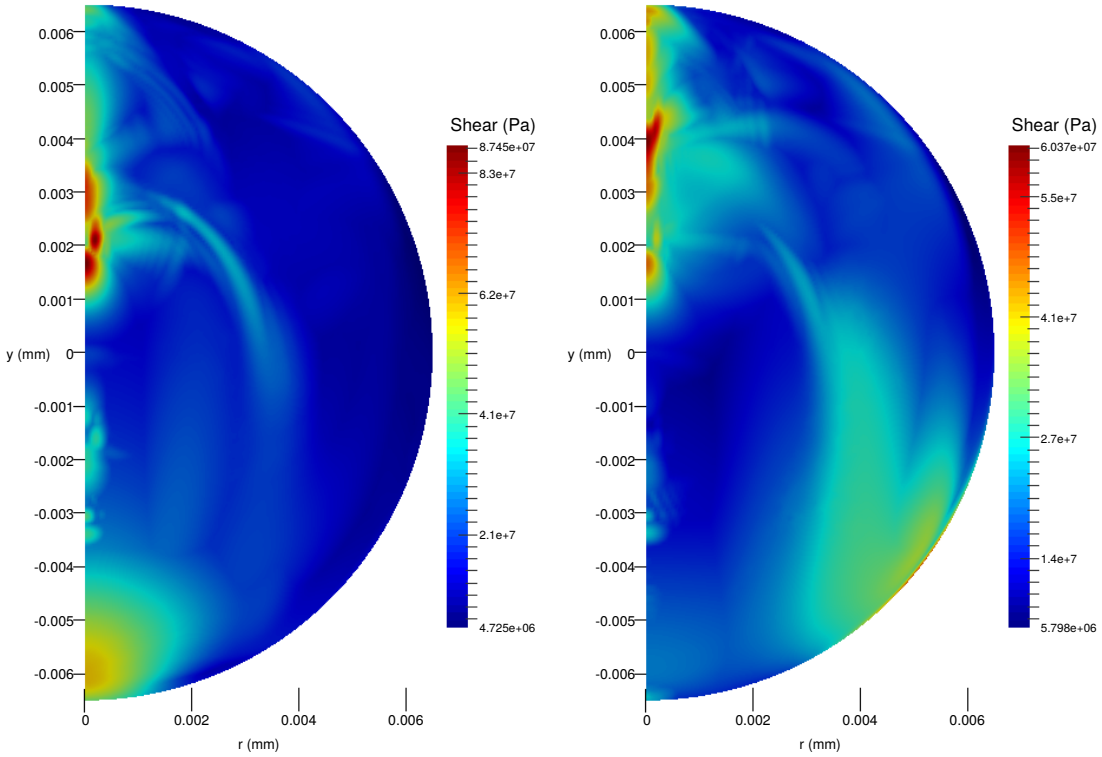

FIGURE 3.12: Maximum peak shear stress. Left: treatment with a Diatron 4 shock wave. Right: treatment with a HM3 shock wave.

Overall, from these simulations, it can be concluded that the dynamic squeezing phenomenon yields much higher tensile and shear stresses than the others mechanical phenomena, as observed on the small stones exposed to the Diatron 4 shock wave. However, it is also hard to conclude on a real difference in efficiency between narrow focus high pressure lithotripters and wide focus low pressure lithotripters in term of mechanical stress inside the stone, as if the shock wave arrives in an optimal position into a normal sized stone in lithotripsy, *i.e.* between 5 to 10 mm wide, both kinds of lithoripters yield similar values. As such, in this thesis no restrictions were made on which kind of focal characteristics the new lithotripter will have.

3.3.2 Piezoelectric lithotripter

The piezoelectric lithotripter available at *EDAP-TMS* was the LT02, which was commercialized in the early 1990's. It consists of 105 circular piezoelectric elements of central frequency 400 kHz and diameter 37.3 mm which are set on a spherical support of radius 430 mm. The electrical feeding circuit delivers a pulse up to 6 kV into the ceramics. The main characteristic of the LT02 compared to classical electroconductive lithotripters is that its *in-vitro* fragmentation is much finer than any other lithotripter: instead of yielding stone fragments between 1 to 4 mm in size, the LT02 comminutes most of the stone into submillimeter fragments powder with only a few fragment with a size comprised between 1 and 2 mm. While it seems to be an advantage as the fragments are easily evacuated in the urine and are less likely to produce another stone, the treatment time was much longer than with a traditional lithotripter. For comparison, the LT02 need around 3000 shock waves *in-vitro* for a complete communition of a plaster of Paris cylinder model stone of diameter 13 mm and length of 14 mm, while the Diatron 4 and 5, which are electroconductive lithotripters, need around 300 shock waves for the same stone.

At the time, this kind of communition was considered as a characteristic of piezoelectric lithotripters. Measurements of the focus of the LT02 and experiments to try to reproduce and understand the phenomenon behind the LT02 fragmentation process were made in this section.

Due to its age, no recent measurements of the focal characteristics of the LT02 were made in decades. As such, measurements using a fiber optic hydrophone were made with the FOPH 2000 from *RP-acoustics*, whose characteristics are presented in table 3.4.

TABLE 3.4: Technical data of the *RP-acoustics* fiber optic hydrophone FOPH 2000.

Spatial Resolution:	100 μm
Pressure range:	-60 MPa to 400 MPa
Rise time:	3 ns
Accuracy:	± 5 %
Bandwidth:	DC to 150 MHz

A fiber optic hydrophone allows very high pressure to be measured with great accuracy, but unfortunately the glass fiber tip is also very fragile when exposed to cavitation. From experience, acoustic waves with a negative pressure inferior to -20 MPa destroy the fiber tip rapidly. In order to have the best accuracy, the hydrophone calibration parameters, needed for later deconvolution, are measured before and after the experiments to ensure that the fiber tip was not damaged during the experiments.

Since the negative pressure was very high, the focus characteristics presented in table 3.5 were measured with a needle hydrophone at full power. A plot of the LT02 shock waves in relation to the voltage setting are shown in fig. 3.13.

TABLE 3.5: -6 dB focus characteristics of the LT02

Frequency (kHz)	width (mm)	length (mm)	Max pressure (MPa)
400	1.6	28	148

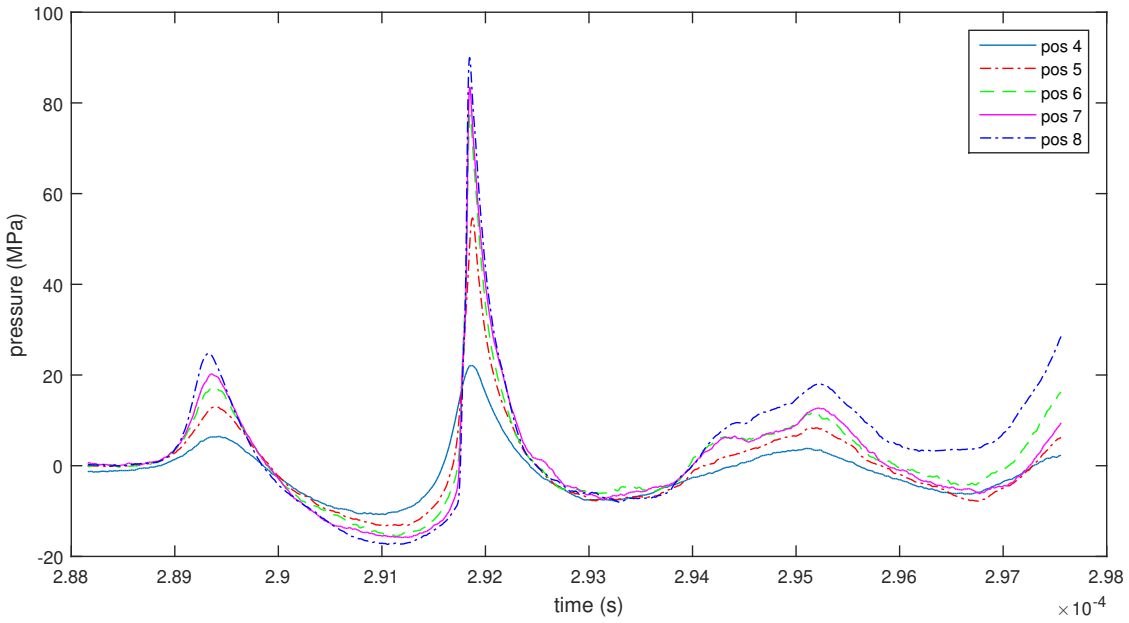

FIGURE 3.13: Pressure measured with the FOPH 2000 at the focal point of the LT02 lithotripter. The legend gives the power output, which is linearly divided in 13 different positions.

The main observation that can be made about the waveform of the LT02 is that the second positive peak pressure is much higher than the first peak positive pressure, which is not usual for a lithotripter. The first peak negative pressure is also unusually high, reaching almost -20 MPa at only 62% power output (the peak negative pressure for electroconductive lithotripters usually floors at -10 MPa). This waveform can be explained by two things: first, as seen in fig. 3.14, each piezoelectric element sends a burst rather than a single pulse, the second pulse having a positive peak pressure almost equal to the first one.

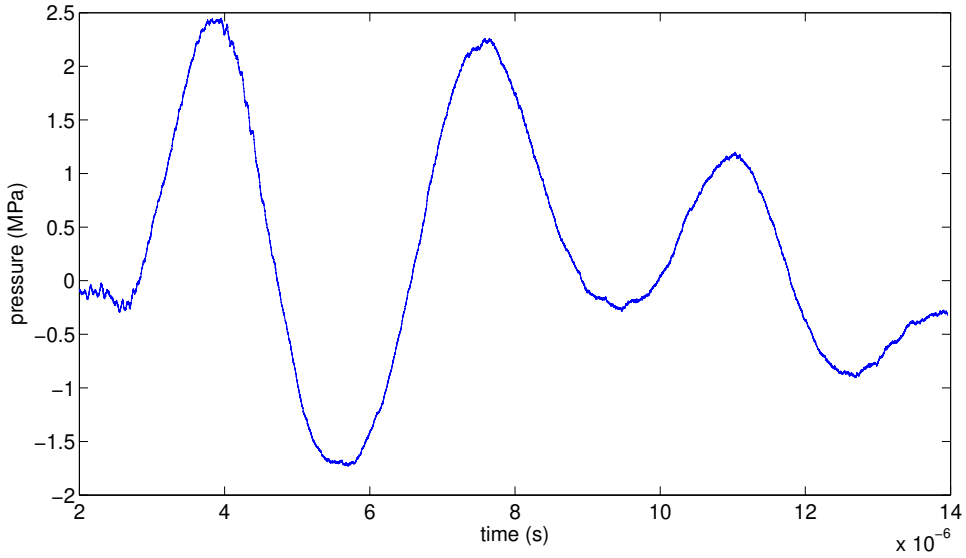

FIGURE 3.14: Surface pressure of one piezoelectric element of the LT02 measured with the fiber optic hydrophone.

Second, the pulses from each element need to travel about 430 mm (the radius of the piezoelectric elements spherical holder) before reaching the focus of the lithotripter. As the circular elements have a diameter of 37.3 mm and a frequency of 400 kHz, the wave travels a distance that is well beyond its near field limit, which means the pressure will decay rapidly, even more so for the first pulse as the other pulses profit from the edge wave pressure of the previous pulse added to them. This means that the second peak pressure of each element will be higher than the first when the beams of different elements crosses each other, resulting in the waveform fig. 3.13.

At the focus of the lithotripter, the first positive peak pressure is almost negligible compared to the second positive peak pressure, and this waveform could be seen as an inverted classical lithotripsy shock wave with the negative pressure first followed by the positive pressure. This kind of inverted lithotripsy shock wave was already studied [138], [139], with the difference that the minimum negative pressure was around -10 MPa, at least half of what the LT02 is capable at maximum voltage. The result of this study showed a reduced cavitation effect due to the forced collapse of the bubbles by the high peak positive pressure. A more recent study showed that, while the forced collapse happens, another phenomenon called liquid jetting is also present, where bubbles exposed to high positive pressure form another smaller bubble due to the squeezing of the shock wave [140]. However here, due to the high negative pressure, this waveform is more likely to yield the results presented in histotripsy where the positive peak pressure following a negative peak pressure high enough to generate a bubble cloud itself is reflected as a negative pulse, extending the existing bubble cloud [122], as detailed in the preceding chapter and illustrated in fig. 2.11. In the lithotripsy case, the pressure arriving onto the proximal face of the stone is partly reflected (without phase inversion), resulting in a negative pressure even

higher on the proximal face of the stone than measured here. This means that the cavitation threshold (around -24 MPa in water at this frequency) is crossed and the presence of a dense bubble cloud on the proximal face of the stone is certain. Therefore, the hypothesis that the LT02 lithotripter main communition mechanism is cavitation is made here, as the dense bubble cloud generated by the first negative pressure almost completely shields the following peak positive pressure and the first peak positive pressure is too low for a narrow focus lithotripter to be really impactful on the stone fragmentation.

In order to validate this hypothesis, another spherical support with a radius of 230 mm for the LT02 elements was built, supporting up to 40 elements. This shock wave generator is shown in fig. 3.15 and the waveforms for different voltages at its focus are shown in fig. 3.16.

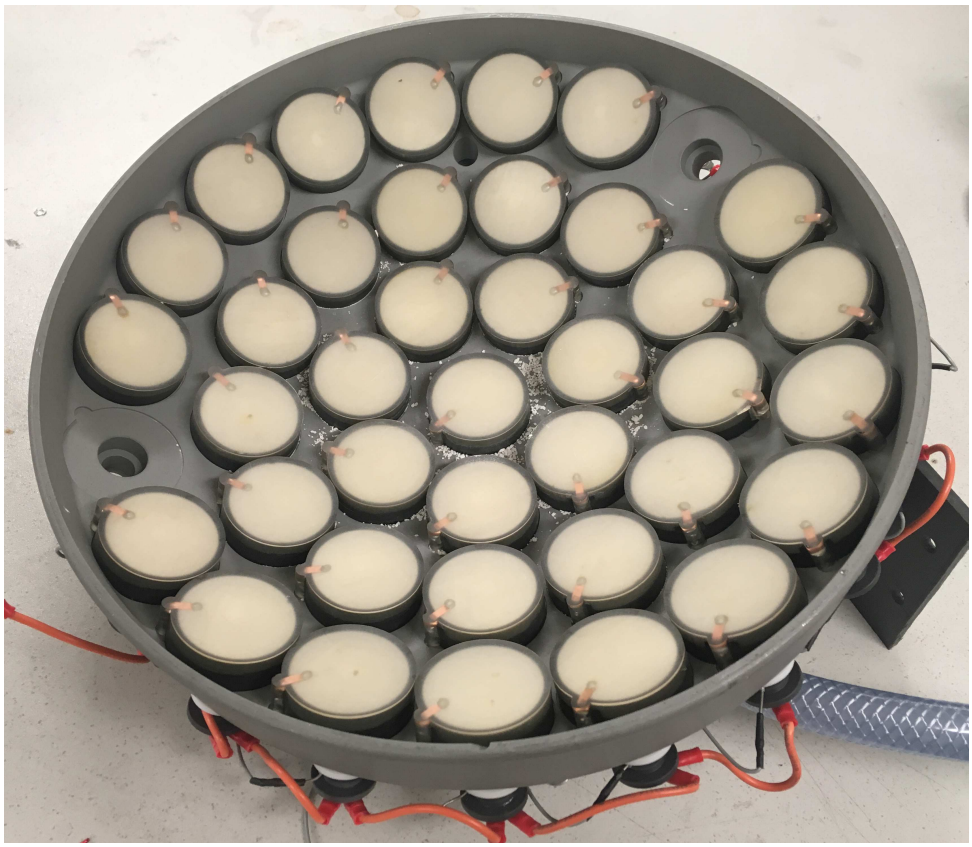

FIGURE 3.15: Support for 40 LT02 piezoelectric elements.

In each case (positive and negative voltage), the focal diameter is almost constant around 2 mm and the focal axial length around 20 mm. Trial treatments onto plaster of Paris cylindrical model stones (13 mm diameter, 14 mm length) were made in order to compare the efficiency between the two waveforms. The trial treatments were realized in degassed water by placing the stones at the focus of the lithotripter in a basket with 2 mm holes. The number of shocks until total comminution is used as comparison between both treatments. An average of 6000 shocks at a PRF of 2 Hz were needed to completely break the model stones with a +5 kV pulse as voltage input, while even after more than 7500 shocks at 2

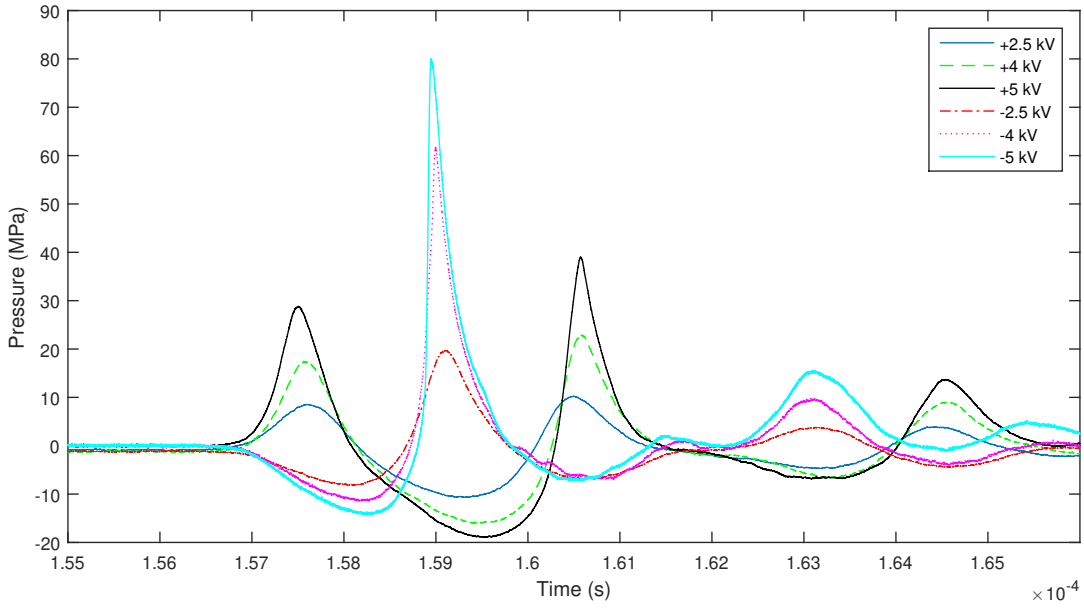

FIGURE 3.16: Waveform for different input pulsed voltage at the focus of the new LT02 elements supports.

Hz PRF the model stone did not completely break with a -5 Kv voltage input. A photo of four model stones after 7500 shocks at a 2 Hz PRF with a -5 kV voltage is shown fig. 3.17.

FIGURE 3.17: Remains of four stones after treatment of more that 7500 shocks at a 2 Hz PRF with a -5 kV input voltage pulse.

In the case of the +5 kV voltage pulse treatment (*i.e.* the waveform close to a traditional ESWL treatment), a mix of fragments with sizes between 1 and 2 mm and submillimeter powder was produced during the communition of the stone, in a very similar manner of the LT02 fragmentation. Meanwhile, the -5 kV

treatment (*i.e.* the reverted waveform) only produced submillimeter powder. In another experiment, the damage caused by both waveforms at equivalent negative pressure (+3.8 kV/-5 kV) and same number of shock waves exposure was made and is shown in fig. 3.18.

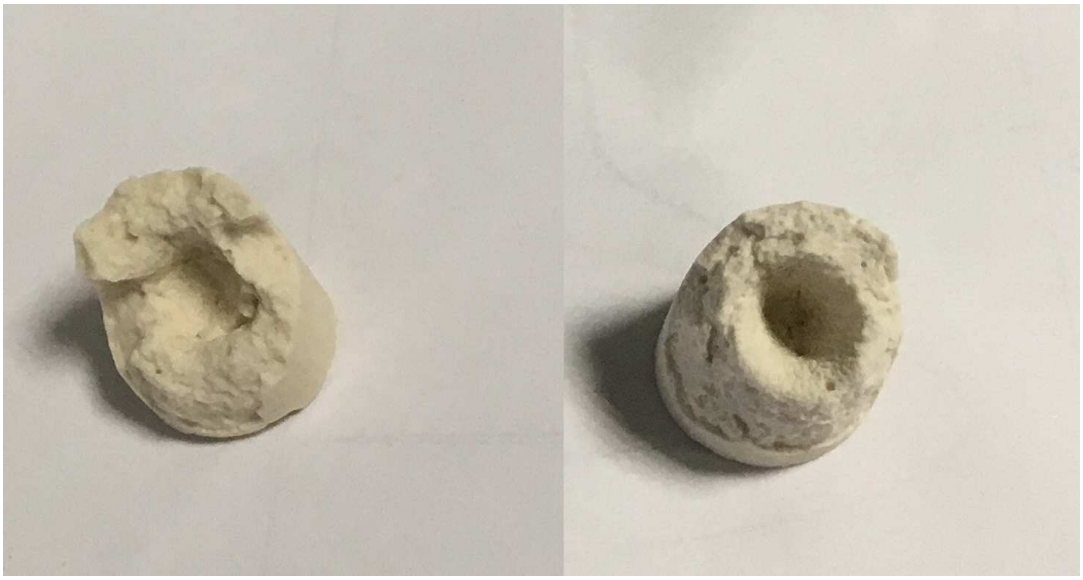

FIGURE 3.18: Left: model stone after 3000 shocks at 2 Hz PRF, +3.8 kV; right: model stone after 3000 shocks at 2 Hz PRF, -5 kV.

The model stone treated with -5 kV presents an almost perfect hole in its center of a diameter close to focal diameter, and is almost intact everywhere else, whereas the stone treated with +3.8 kV also presents a similar hole but coarser and is more damaged around it. The damages caused by the -5 kV pulse is also very similar to the cavitational damages in stones exposed by histotripsy bursts [141]. All of those observations support the original hypothesis that a high negative pressure shields the stone almost completely, meaning that, in order to have a faster stone communition with the LT02, the first positive peak pressure should be higher. The second positive peak pressure could also generate a large bubble cloud farther behind the stone (toward the lithotripter) that could potentially be harmful for the surrounding tissue. However, after decades of treatments with the LT02, no injuries outside the ones observed in other lithotripters were observed.

To conclude, in regards to the fragmentation efficiency in shock wave lithotripsy, the shock wave should be composed of a positive pressure first followed by a negative pressure, in that order, and everything after that will have no apparent effect of the comminution process due to the bubble shielding generated by the negative pressure. As such, in the case of the piezoelectric lithotripters presented here, efforts should be made to maximize the first peak pressure and lower the amplitude of the other pulses following it.

3.4 Conclusion

The numerical simulation and experiments presented in this chapter opened the path for multiple works presented in the next chapters. First, in order to optimize the efficiency of a piezoelectric lithotripter based on the *EDAP-TMS* LT02, a full optimization of the piezoelectric elements composing it is made in the next chapter. Then, a confocal setup, using optimized lens focused piezoelectric transducers presented in chapter 5, that could allow to try new focal characteristics, is designed and presented in chapter 6.

Chapter 4

Finite element optimization of piezoelectric transducer

4.1 Introduction

Multi-element piezoelectric transducers are now widely used in shock wave generators to fragment kidney stones (lithotripsy) or for ablating soft tissues (histotripsy). These elements are usually dimensioned to work in steady-state. However, for these applications, only one to ten pulses long bursts are emitted. Thus, most of the signal is sent while the piezoelectric transducers vibrate in a transient state. Another problem that emerges from using piezoelectric transducers in lithotripsy and histotripsy is the very high voltage applied over a short time in order to create a shock wave, meaning that the ceramic is under high stress and the delivery circuit used is different than the one used in steady-state regime.

This work follows the preliminary experiments made on the *EDAP-TMS* LT02 piezoelectric lithotripter presented in the preceding chapter and aims at optimizing the design of these elements. A transient finite element model of a piezoelectric circular element is presented. It includes its epoxy and plastic casing, the surrounding water and its discharge circuit (a RLC circuit). The model is then used in parametric optimization of the circuit components (the value of the inductor and resistor that yield the higher output) and the epoxy parameters (mechanical and geometrical) front and back layers.

Piezoelectricity

The piezoelectric phenomenon is defined as the conversion of mechanical energy into electrical energy (called the direct effect of piezoelectricity) and reciprocally (the indirect effect). The piezoelectric effect is presented by 2 coupled equations that bind the electrical variables (the electric charge displacement $\mathbf{D}$ or the electrical field $\mathbf{E}$) and the mechanical variables (the strain $\mathbf{S}$ or the stress $\mathbf{T}$). The constitutive relation in stress-charge form is presented here in (4.1), as given in the IEEE Standard on Piezoelectricity [142].

$$\begin{cases} \mathbf{T} = \mathbf{c}^{\mathbf{E}} \cdot \mathbf{S} - \mathbf{e}^{t} \cdot \mathbf{E} \\ \mathbf{D} = \mathbf{e} \cdot \mathbf{S} + \boldsymbol{\varepsilon}^{S} \cdot \mathbf{E} \end{cases} \tag{4.1}$$

TABLE 4.1: Parameters used in the piezoelectric constitutive equations

Symbol	Meaning	Type
$\mathbf{D}$	Electric charge density in $\frac{C}{m^2}$	Electric
$\mathbf{E}$	Electric field in $\frac{N}{C}$	
ε^S	Electric permittivity in $\frac{F}{m}$	
$\mathbf{S}$	Strain in $\frac{m}{m}$	Mechanical
$\mathbf{T}$	Stress in $\frac{N}{m^2}$	
$\mathbf{c}^\mathbf{E}$	Stiffness in $\frac{N}{m^2}$	
$\mathbf{e}$	Piezoelectric coupling in $\frac{C}{m^2}$	Piezoelectric

Infinitesimal deformations are considered and thus the strain tensor $\mathbf{S}$ is defined as

$$\mathbf{S} = \frac{1}{2}\left(\nabla\mathbf{u} + (\nabla\mathbf{u})^t\right) \tag{4.2}$$

where $\mathbf{u}$ is the displacement vector.

The quasielectrostatic approximation of the electromagnetic equation is used to describe the electric and magnetic field of a piezoelectric material. Thus, the electric field vector $\mathbf{E}$ derives from a scalar potential ϕ:

$$\mathbf{E} = -\nabla\phi \tag{4.3}$$

and the electric displacement field $\mathbf{D}$ is defined as for an insulator:

$$\nabla \cdot \mathbf{D} = 0 \tag{4.4}$$

The dynamic behaviour of the piezoelectric material is defined by the equation of motion (here without body forces):

$$\nabla \cdot \mathbf{T} = \rho\frac{\partial^2\mathbf{u}}{\partial t^2} \tag{4.5}$$

where ρ is the density of the material.

Linear elasticity

The solid parts of the transducers (the ceramic support and the resin) can be described using the dynamic linear elasticity theory, which consists of the equation of motion (4.5), and the constitutive model, that is defined by Hooke's law for isotropic and homogeneous material:

$$\mathbf{T} = 2\mu\mathbf{S} + \lambda tr(\mathbf{S})I \tag{4.6}$$

where μ and λ are the Lamé constants, and I is the second-order identity tensor.

Fluid

Since one of the objectives is to obtain the pressure field in a region close to the surface of the transducer, the non-linear effects and the absorption can be assumed negligible, and thus the fluid is modeled using the lossless linear acoustic equation:

$$\frac{\partial^2 p}{\partial t^2} - c^2 \nabla^2 p = 0 \tag{4.7}$$

where p is the pressure and c the small pressure sound speed.

Fluid-structure interface

The coupling between the surface of the transducer and the acoustic fluid is given by [143], [144]:

$$\frac{\partial p}{\partial n} + \rho \frac{\partial^2 \mathbf{u}}{\partial t^2} \cdot \mathbf{n} = 0 \tag{4.8}$$

for the fluid boundary condition, and inside the solid domain, the boundary condition is

$$\mathbf{T} \cdot \mathbf{n} + p\mathbf{n} = 0 \tag{4.9}$$

where $\mathbf{n}$ is the outward (in relation to the solid domain) unit normal at the interface.

RLC circuit

In order to generate a shock wave with only a few transducers, very high voltage is applied to the piezoelectric material. In order to deliver this kind of voltage, a serial RLC circuit is used, with a previously charged capacitor as a source and an inductance and resistor controlling the charge/discharge period. The charge/discharge loop of this circuit can be modelled as in fig. 4.1.

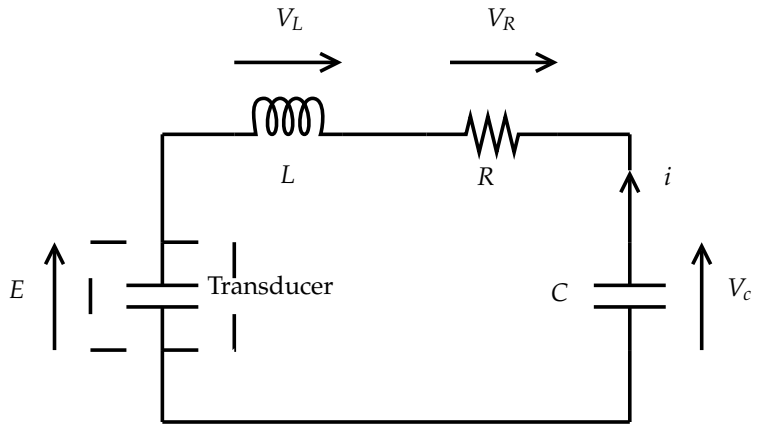

FIGURE 4.1: The modelled transducer.

The differential equation describing this circuit is:

$$V_c - Ri - L\frac{\mathrm{d}i}{\mathrm{d}t} = E \tag{4.10}$$

defining the circuit total charge q as $i = -\frac{\mathrm{d}q}{\mathrm{d}t}$ gives:

$$V_c + R\frac{\mathrm{d}q}{\mathrm{d}t} + L\frac{\mathrm{d}^2q}{\mathrm{d}t^2} = E \tag{4.11}$$

knowing that the capacitor C is charged such as $q_0 = CV_C$ at $t = 0$ and using the charge conservation of the circuit $q(t) + q_C(t) = q_0$ yields:

$$LC\frac{\mathrm{d}^2q}{\mathrm{d}t^2} + RC\frac{\mathrm{d}q}{\mathrm{d}t} - q = CE - q_0 \tag{4.12}$$

This equation can be linked to the piezoelectric constitutive equation by noting that, on the surface of the ceramic:

$$\mathbf{D} \cdot \mathbf{n} = -\frac{q}{A_p} \tag{4.13}$$

where A_p is the area of the piezoceramic linked to the circuit and $\mathbf{n}$ is the outward unit normal.

4.2 Problem formulation

The transducers used here are taken from the LT02 lithotripter, by *EDAP-TMS*, shown in fig. 4.2.

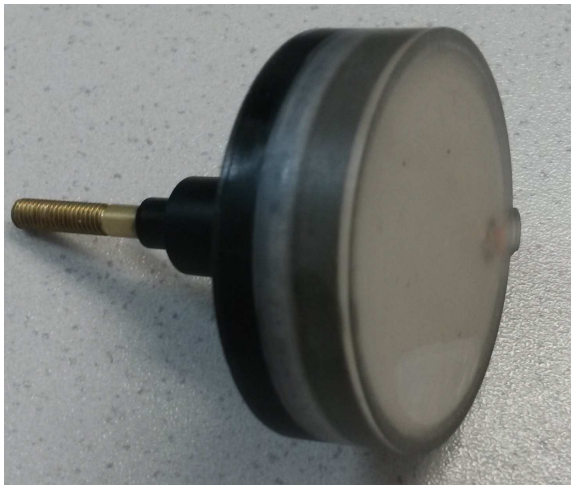

FIGURE 4.2: The LT02 piezoelectric transducer.

Each transducer is composed of a plastic molded support, a piezoceramic disc, and is held all together by an epoxy resin (that acts as both backing and front layer). The model is shown in fig. 4.3.

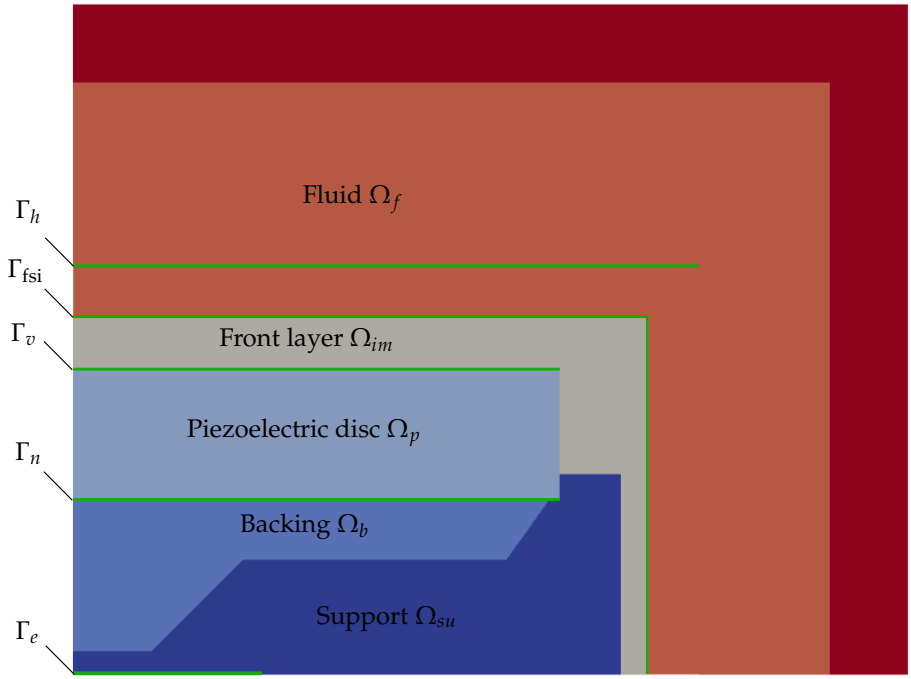

FIGURE 4.3: The modeled transducer.

The equations governing the whole transducer are :

$$
\begin{cases}
\rho \ddot{u}_i - T_{ij,j} = 0 & \text{in } \Omega_{su} \cup \Omega_b \cup \Omega_p \cup \Omega_{im} \times I, \quad (4.14)\\
T_{ij} = 2\mu S_{ij} + \lambda S_{kk}\delta_{ij} & \text{in } \Omega_{su} \cup \Omega_b \cup \Omega_{im} \times I, \quad (4.15)\\
T_{ij} = c^E_{ijkl} S_{kl} + e_{kij}\phi_{,k} & \text{in } \Omega_p \times I, \quad (4.16)\\
D_i = e_{ikl} S_{kl} - \varepsilon^S_{ik}\phi_{,k} & \text{in } \Omega_p \times I, \quad (4.17)\\
D_{i,i} = 0 & \text{in } \Omega_p \times I, \quad (4.18)\\
\ddot{p} - c^2 p_{,ii} = 0 & \text{in } \Omega_f \times I, \quad (4.19)\\
p_{,i} n_i + \rho_f \ddot{u}_i n_i = 0 & \text{on } \Gamma_{\text{fsi}} \times I, \quad (4.20)\\
T_{ij} n_i + p n_i = 0 & \text{on } \Gamma_{\text{fsi}} \times I, \quad (4.21)\\
LC\ddot{q} + RC\dot{q} - q = C\phi - q_0 & \text{on } \Gamma_v \times I, \quad (4.22)\\
D_i n_i A_p = -q & \text{on } \Gamma_v \times I, \quad (4.23)\\
\phi = \lambda_m, \quad \lambda_m \in \mathbb{R} & \text{on } \Gamma_v \times I, \quad (4.24)\\
u_i = 0 & \text{on } \Gamma_e \times I, \quad (4.25)\\
\phi = 0 & \text{on } \Gamma_n \times I, \quad (4.26)\\
u_i(\mathbf{x}, 0) = \dot{u}_i(\mathbf{x}, 0) = 0 & \text{in } \Omega_{su} \cup \Omega_b \cup \Omega_p \cup \Omega_{im}, \quad (4.27)\\
\phi(\mathbf{x}, 0) = 0 & \text{in } \Omega_p, \quad (4.28)\\
p(\mathbf{x}, 0) = \dot{p}(\mathbf{x}, 0) = 0 & \text{in } \Omega_f, \quad (4.29)\\
q(0) = \dot{q}(0) = 0 & \text{on } \Gamma_v, \quad (4.30)
\end{cases}
$$

where the letter $\Omega \subset \mathbb{R}^d$, $d \in [1,2,3]$ represents a spatial domain and $\partial\Omega$ represents its entire boundary, $I =]0,T]$ is the time interval of interest and $\mathbf{x}$ is a vector such as $\mathbf{x} \in \Omega$.

In this partial differential equation (PDE) problem, (4.14) is the equation of motion without body forces, (4.15) is Hooke's law, (4.16),(4.17),(4.18) are the piezoelectric constitutive equations, (4.19) is the linear lossless acoustic equation, (4.20) and (4.21) are the fluid-structure interface coupling, (4.22) is the equation of the feeding circuit, (4.23) is the coupling between the charge at the surface of the piezoceramic and the charge in the feeding circuit, (4.24) is to ensure that the electric potential is constant on the surface of the piezoceramic linked to the feeding circuit, (4.25),(4.26) are the boundary conditions and (4.27),(4.28),(4.29),(4.30) are the initial conditions. Also, it should be noted that the parameters ρ, μ and λ are not spatially constant and depend of each domain.

4.2.1 Weak formulation

In order to get a numerical solution of the problem using the finite element method, the problem needs to be written in weak form. By inserting (4.15) in (4.14), multiplying by a test function and integrating over the domains, the linear elastic problem can be written as: find $u_i \in U$ such that $\forall v_i \in \hat{U}$, in the solid domain $\Omega_s = \Omega_{su} \cup \Omega_b \cup \Omega_p \cup \Omega_{im}$,

$$\int_{\Omega_s} \rho \ddot{u}_i v_i \, \mathrm{d}x - \int_{\Omega_s} T_{ij,j} v_i \, \mathrm{d}x = 0 \tag{4.31}$$

where U and $\hat{U}$ are the trial and test spaces defined as:

$$U = \{u_i \in H^1(\Omega_s) : u_i = 0 \text{ on } \Gamma_e\}, \tag{4.32}$$

$$\hat{U} = \{v_i \in H^1(\Omega_s) : v_i = 0 \text{ on } \partial\Omega_s\}. \tag{4.33}$$

where H is the Sobolev space and the notation $\partial\Omega$ means the complete boundary of the domain Ω.

By integrating by part, applying the divergence theorem and injecting the boundary condition (4.21), (4.31) becomes:

$$\int_{\Omega_s} \rho \ddot{u}_i v_i \, \mathrm{d}x + \int_{\Omega_s} T_{ij} v_{i,j} \, \mathrm{d}x + \int_{\Gamma_{\text{fsi}}} p v_i n_i \, \mathrm{d}s = 0 \tag{4.34}$$

Considering symmetric stress and strain tensors, we can write $v_{i,j} = \frac{1}{2}(v_{i,j} + v_{j,i})$, and then assimilate it to the strain tensor defined in (4.2). Thus, (4.34) can be written as:

$$\int_{\Omega_s} \rho \ddot{u}_i v_i \, \mathrm{d}x + \int_{\Omega_s} T_{ij} S_{ij}(v) \, \mathrm{d}x + \int_{\Gamma_{\text{fsi}}} p v_i n_i \, \mathrm{d}s = 0 \tag{4.35}$$

In the non piezoelectric part of the domain, the stress tensor is calculated using Hooke's law (4.15), and therefore the weak form in that domain is :

$$\int_{\Omega_s \setminus \Omega_p} \rho \ddot{u}_i v_i \, \mathrm{d}x + \int_{\Omega_s \setminus \Omega_p} \left(2\mu S_{ij}(u) + \lambda S_{kk}(u)\delta_{ij}\right) S_{ij}(v) \, \mathrm{d}x + \int_{\Gamma_{\text{fsi}}} p v_i n_i \, \mathrm{d}s = 0 \tag{4.36}$$

and in the piezoelectric domain, the constitutive equation (4.16) is injected in (4.35) (and the Neumann boundary condition is removed since the piezoelectric domain is not in contact with the fluid):

$$\int_{\Omega_p} \rho \ddot{u}_i v_i \, \mathrm{d}x + \int_{\Omega_p} c^E_{ijkl} S_{kl}(u) S_{ij}(v) \, \mathrm{d}x + \int_{\Omega_p} e_{kij} \phi_{,k} S_{ij}(v) \, \mathrm{d}x = 0 \tag{4.37}$$

For the electrical problem inside the piezoceramic, the variational problem reads: find $\phi \in \Phi$ such that $\forall \psi \in \hat{\Phi}$,

$$\int_{\Omega_p} D_{i,i} \psi \, \mathrm{d}x = 0 \tag{4.38}$$

where Φ and $\hat{\Phi}$ are the trial and test space defined as:

$$\Phi = \{\phi \in H^1(\Omega_p) : \phi = 0 \text{ on } \Gamma_n\}, \tag{4.39}$$

$$\hat{\Phi} = \{\psi \in H^1(\Omega_p) : \psi = 0 \text{ on } \partial\Omega_p\}. \tag{4.40}$$

Integrating by part, applying the divergence theorem on (4.38), injecting the constitutive equation (4.17) and the boundary condition (4.23) yields:

$$\int_{\Omega_p} e_{ikl} S_{kl}(u) \psi_{,i} \, \mathrm{d}x - \int_{\Omega_p} \varepsilon^S_{ik} \phi_{,k} \psi_{,i} \, \mathrm{d}x - \int_{\Gamma_v} \frac{q}{A_p} \psi \, \mathrm{d}s = 0 \tag{4.41}$$

The boundary condition (4.24) is enforced using a lagrange multiplier $\lambda_m \in \mathbb{R}$ and its test function Λ_m:

$$\int_{\Gamma_v} (\phi - \lambda_m) \Lambda_m \, \mathrm{d}s + \int_{\Gamma_v} (\phi - \lambda_m) \psi \, \mathrm{d}s = 0 \tag{4.42}$$

The feeding circuit equation that serves as a boundary condition, which is also an ordinary differential equation, can be written in weak form, with $q \in \mathbb{R}$ and its test function ξ as:

$$LC\ddot{q}\xi + RC\dot{q}\xi - q\xi - C\lambda_m \xi = -q_0 \xi \tag{4.43}$$

The acoustic fluid problem reads: for $p \in P$ and $\forall w \in \hat{P}$,

$$\int_{\Omega_f} \ddot{p} w \, \mathrm{d}x - \int_{\Omega_f} c^2 p_{,ii} w \, \mathrm{d}x = 0 \tag{4.44}$$

where P and $\hat{P}$ are the trial and test spaces defined as:

$$P = \{p \in H^1(\Omega_f)\}, \tag{4.45}$$
$$\hat{P} = \{w \in H^1(\Omega_f) : w = 0 \text{ on } \partial\Omega_f\}. \tag{4.46}$$

Integrating by part, applying the divergence theorem on (4.44) and injecting the boundary condition (4.20) (and remembering that in that boundary condition the normal is inward while the normal in the divergence theorem is outward) yields:

$$\int_{\Omega_f} \ddot{p} w \,\mathrm{d}x + \int_{\Omega_f} c^2 p_{,i} w_{,i} \,\mathrm{d}x - \int_{\Gamma_{\text{fsi}}} \rho_f c^2 \ddot{u}_i n_i w \,\mathrm{d}s = 0 \tag{4.47}$$

Finally, the variational problem in mixed formulation for the complete transducer reads: find $(u_i, p, \phi, q, \lambda_m) \in [U, P, \Phi, \mathbb{R}, \mathbb{R}]$ such that $\forall (v_i, w, \psi, \xi, \Lambda_m) \in [\hat{U}, \hat{P}, \hat{\Phi}, \mathbb{R}, \mathbb{R}]$:

$$\begin{aligned}
&\int_{\Omega_s} \rho \ddot{u}_i v_i \,\mathrm{d}x + \int_{\Omega_s \setminus \Omega_p} \left(2\mu S_{ij}(u) + \lambda S_{kk}(u)\delta_{ij}\right) S_{ij}(v) \,\mathrm{d}x + \int_{\Gamma_{\text{fsi}}} p v_i n_i \,\mathrm{d}s + \\
&\int_{\Omega_p} c^E_{ijkl} S_{kl}(u) S_{ij}(v) \,\mathrm{d}x + \int_{\Omega_p} e_{kij} \phi_{,k} S_{ij}(v) \,\mathrm{d}x + \\
&\int_{\Omega_p} e_{ikl} S_{kl}(u) \psi_{,i} \,\mathrm{d}x - \int_{\Omega_p} \varepsilon^S_{ik} \phi_{,k} \psi_{,i} \,\mathrm{d}x - \int_{\Gamma_v} \frac{q}{A_p} \psi \,\mathrm{d}s + \\
&\int_{\Gamma_v} (\phi - \lambda_m) \Lambda_m \,\mathrm{d}s + \int_{\Gamma_v} (\phi - \lambda_m) \psi \,\mathrm{d}s + \\
&\int_{\Omega_f} \ddot{p} w \,\mathrm{d}x + \int_{\Omega_f} c^2 p_{,i} w_{,i} \,\mathrm{d}x - \int_{\Gamma_{\text{fsi}}} \rho_f c^2 \ddot{u}_i n_i w \,\mathrm{d}s + \\
&L C \ddot{q} \xi + R C \dot{q} \xi - q \xi - C \lambda_m \xi = -q_0 \xi
\end{aligned} \tag{4.48}$$

4.2.2 Temporal discretization

The discretized time integration for a timestep Δt and for a generic variable q is realised using a Newmark-β method, presented as follows:

$$\begin{cases}
\dot{q}_{n+1} = \dot{q}_n + (1-\gamma)\,\Delta t \ddot{q}_n + \gamma \Delta t \ddot{q}_{n+1} & (4.49) \\
q_{n+1} = q_n + \Delta t \dot{q}_n + \Delta t^2 \left(\frac{1}{2} - \beta\right) \ddot{q}_n + \Delta t^2 \beta \ddot{q}_{n+1} & (4.50)
\end{cases}$$

where γ and β are two real parameters of the Newmark method, and the subscripts n and $n+1$ represent the function at the time t and $t + \Delta t$, respectively. In order to have an unconditionally stable scheme, the trapezoidal rule ($\gamma = \frac{1}{2}$ and $\beta = \frac{1}{4}$) is used here.

4.2.3 Finite element implementation

Once the problem is well formulated, the time discretized weak formulation of the problem is solved using FEniCS (at the time 1.6.0) [145], [146]. The open source FEniCS project is a collection of tools aiming to automate solution of differential equations by the finite element method.

In the following sections, the problem is considered 2D axisymmetric. The finite element used here is a linear continuous Lagrange (CG_1) triangle, and due to the mixed formulation used, each node of the element has 6 degrees of freedom, which are $(u_1, u_2, p, \phi, q, \lambda_m)$. So, even if some of the DoFs are unused on part of the domain, they are considered during the assembly, which leads to bigger system matrix than a non mixed formulation. The main advantage of using a mixed formulation here is for an easier implementation of the various couplings. Also, block matrix preconditioning is still rudimentary on FEniCS, and due to the complexity of the problem using a direct solver will not be considered.

The axisymmetry is implemented by writing (4.48) in vector notation, expressing the different tensors as vectors by exploiting the symmetry of the strain and stress tensors, using the cylindrical coordinate (r, θ, z) (and thus $\mathrm{d}x = r\,\mathrm{d}r\,\mathrm{d}\theta\,\mathrm{d}z$) and then using the property of axysimmetry $\frac{\partial}{\partial\theta} = 0$ to effectively remove the coordinate θ from the problem (by integrating on θ and then dividing by 2π). More detail about this process can be found in the book [147]. Therefore, the problem in vector notation is:

$$\begin{aligned}
&\int_{\Omega_s} \rho\{v\}^T\{\ddot{u}\}\,\mathrm{d}x + \int_{\Omega_s\setminus\Omega_p} \{S(v)\}^T[C_s]\{S(u)\}\,\mathrm{d}x + \int_{\Gamma_{\text{fsi}}} \{v\}^T p\{n\}\,\mathrm{d}s + \\
&\int_{\Omega_p} \{S(v)\}^T[c^E]\{S(u)\}\,\mathrm{d}x + \int_{\Omega_p} \{S(v)\}^T[e]^T\{\mathrm{grad}(\phi)\}\,\mathrm{d}x + \\
&\int_{\Omega_p} \{\mathrm{grad}(\psi)\}[e]\{S(u)\}\,\mathrm{d}x - \int_{\Omega_p} \{\mathrm{grad}(\psi)\}[\varepsilon^S]\{\mathrm{grad}(\phi)\}\,\mathrm{d}x - \int_{\Gamma_v} \psi\frac{q}{A_p}\,\mathrm{d}s + \\
&\int_{\Gamma_v} (\phi - \lambda_m)\,\Lambda_m\,\mathrm{d}s + \int_{\Gamma_v} (\phi - \lambda_m)\,\psi\,\mathrm{d}s + \\
&\int_{\Omega_f} \ddot{p}w\,\mathrm{d}x + \int_{\Omega_f} c^2\{\mathrm{grad}(w)\}^T\{\mathrm{grad}(p)\}\,\mathrm{d}x - \int_{\Gamma_{\text{fsi}}} \rho_f c^2 w\{\ddot{u}\}^T\{n\}\,\mathrm{d}s + \\
&LC\ddot{q}\xi + RC\dot{q}\xi - q\xi - C\lambda_m\xi = -q_0\xi \qquad (4.51)
\end{aligned}$$

where the matrices are defined as:

$$[C_s] = \begin{bmatrix} 2\mu+\lambda & \lambda & \lambda & 0 \\ \lambda & 2\mu+\lambda & \lambda & 0 \\ \lambda & \lambda & 2\mu+\lambda & 0 \\ 0 & 0 & 0 & \mu \end{bmatrix}$$

$$[C^E] = \begin{bmatrix} C^E_{11} & C^E_{12} & C^E_{13} & 0 \\ C^E_{12} & C^E_{22} & C^E_{13} & 0 \\ C^E_{13} & C^E_{13} & C^E_{33} & 0 \\ 0 & 0 & 0 & C^E_{44} \end{bmatrix}$$

$$[e] = \begin{bmatrix} 0 & 0 & 0 & e_{15} \\ e_{31} & e_{31} & e_{33} & 0 \end{bmatrix}$$

$$[\varepsilon^S] = \begin{bmatrix} \varepsilon^S_{11} & 0 \\ 0 & \varepsilon^S_{33} \end{bmatrix}$$

and the vectors as:

$$\{S(u)\} = \begin{Bmatrix} S_{rr} \\ S_{\theta\theta} \\ S_{zz} \\ 2S_{r\theta} \end{Bmatrix} = \begin{bmatrix} \frac{\partial}{\partial r} & 0 \\ \frac{1}{r} & 0 \\ 0 & \frac{\partial}{\partial z} \\ \frac{\partial}{\partial z} & \frac{\partial}{\partial r} \end{bmatrix} \begin{Bmatrix} u_r \\ u_z \end{Bmatrix} = [B_u]\{u\}$$

$$\{\text{grad}(\phi)\} = \begin{Bmatrix} \frac{\partial}{\partial r} \\ \frac{\partial}{\partial z} \end{Bmatrix} \phi = \{B_\phi\}\phi$$

Since the data published by the piezoceramic supplier are not always in the stress-charge form (see (4.1)), conversion formulae between the different forms can be found in the IEEE Standard on Piezoelectricity [142]. The problem is solved using an iterative solver (PETSc, [148]), and the fastest solver was found to be the biconjugate gradient stabilised method in combination to the Hypre BomerAMG preconditioner [149]. Due to the presence of lagrange multipliers, the relative tolerance had to be set unusually low (10^{-12}) in order to have an accurate result.

4.2.4 Electrical pre-stress

The feeding circuit also allows to set an initial stress to the piezoceramic in order to get a higher pressure output of the transducer. In order to do this, a RLC circuit with a slow discharge period is used, and thus almost no pressure is generated in the surrounding fluid during this discharge. This process can be simulated easily by solving the problem only in the solid domain Ω_s in static regime (see (4.52)), with the electrical boundary set as $\phi = \text{HT}^+$ on Γ_v. The result is then injected as initial conditions and the problem is solved as usual.

$$\begin{aligned} &\int_{\Omega_s \cap \Omega_p} \{S(v)\}^T [C_s] \{S(u)\} \, \mathrm{d}x + \\ &\qquad \int_{\Omega_p} \{S(v)\}^T [c^E] \{S(u)\} \, \mathrm{d}x + \int_{\Omega_p} \{S(v)\}^T [e]^T \{\text{grad}(\phi)\} \, \mathrm{d}x + \\ &\int_{\Omega_p} \{\text{grad}(\psi)\} [e] \{S(u)\} \, \mathrm{d}x - \int_{\Omega_p} \{\text{grad}(\psi)\} [\varepsilon^S] \{\text{grad}(\phi)\} \, \mathrm{d}x = 0 \end{aligned} \quad (4.52)$$

4.3 Experimental measurements

In order to validate the model presented in the preceding section, experimental measurements of the surface pressure of the *EDAP-TMS* LT02 piezoelectric

transducer were made using a fiber optic hydrophone (FOPH 2000, from *RP-Acoustics*). The main advantages here of a fiber optic hydrophone are its very low spatial resolution (supplier gives 100 μm), allowing a precise mapping of the pressure field and its very large bandwidth (DC to 150 MHz), and the main disadvantage is its low pressure resolution, which is $\pm 0.7\,MPa$, while the pressure field to be measured has values around 1 to 3 MPa. This problem can be compensated by averaging the measurements, here using one hundred measurements per spatial point, since the repeatability of piezoelectric transducers is extremely high.

The feeding circuit used for the measurements consists of two capacitor C1 and C2 that are charged by two high voltage power supplies, and can then be discharged into the piezoelectric elements by closing the high voltage switches T1 and T2. The discharge time was controlled by a RL circuit. The complete feeding circuit is shown in fig. 4.4. The pre-stress part was not used for the measurement and thus T1 was always left open.

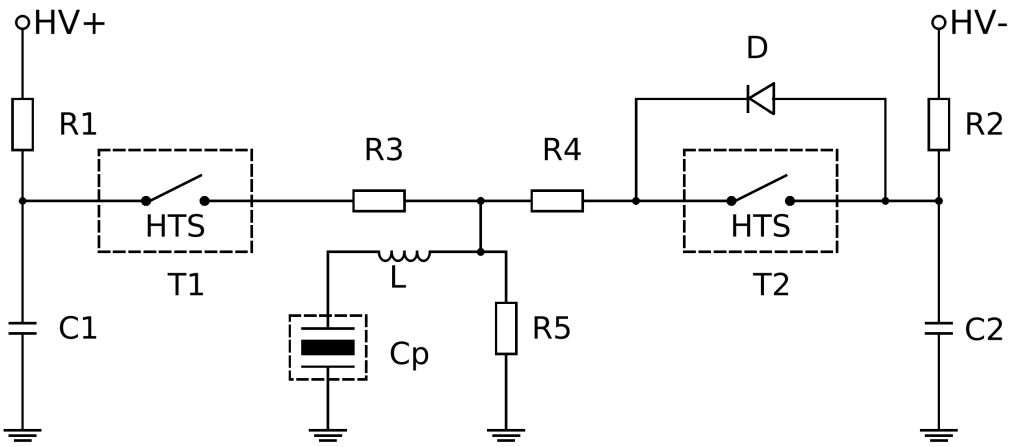

FIGURE 4.4: The experimental feeding circuit.

All measurements were averaged directly by the *LeCroy* oscilloscope and thereafter deconvoluted.

4.4 Model validation

The objective of this section is to evaluate how well the model of section 4.2 reproduces the pressure field measured out of an *EDAP-TMS* LT02 transducer.

4.4.1 Material properties and electrical configuration

The support of the LT02 transducer is molded with a *Synres Almoco* 3535 glass fiber reinforced plastic with a Young's modulus of 16.5 GPa, a density of 2000 $kg.m^{-3}$ and a Poisson coefficient of 0.3, the backing and front layer are both made of *Araldite* 2020 epoxy with a Young's modulus of 2.4 GPa, a density of

$1100\,kg.m^{-3}$ and a Poisson coefficient of 0.3, and the fluid is simple degassed water ($c = 1500\,m.s^{-1}$, $\rho_f = 1000\,kg.m^{-3}$. The piezoelectric material is a PZT-403 from *Morgan Technical Ceramics*, whose properties are detailed in table 4.2.

TABLE 4.2: Properties of the PZT 403.

$\rho(kg/m^3)$	$S_{11}^E(m^2/N)$	$S_{33}^E(m^2/N)$
7600	$13.3 \cdot 10^{-12}$	$16.8 \cdot 10^{-12}$
K_{33}^T	$d_{31}(pC/N)$	$d_{33}(pC/N)$
1350	135	315

As for the circuit, the capacitor was set as $C = 0.1\,\mu F$, the total circuit resistance as $R \approx 80\,\Omega$ and the inductance as $L = 41.7\,\mu H$. The voltage of the capacitor at $t = 0$ was $4\,kV$.

4.4.2 The pressure field

The calculated and the measured pressure fields are shown in fig. 4.5.

The measurements were made with a resolution of $1\,mm$, and at an approximate distance of $5\,mm$ to the surface of the transducer. The mesh size seed of the simulation was $50\,\mu m$ and the time step was $\Delta t = 30\,ns$, and the result contour is made of values taken at the Γ_h line, at $5\,mm$ of the surface of the transducer. The domain Ω_f was chosen large enough to avoid acoustic reflection on the boundaries coming back into the transducer or the line Γ_h.

4.4.3 The electrical boundary

The measured and calculated electrical potentials at the surface of the piezoceramic (λ_m in the model) are shown in fig. 4.6.

4.4.4 Discussion

The comparisons show that, while there are some distinct differences between the experimental measurements and the numerical model, the model and the measurements are in overall good agreement. The differences can be explained by several reasons, the first being the complexity of the model: 4 different materials are used, each one having its own variability of properties, mainly the piezoelectric one with an error margin comprised between 5 to 20 % unless proper parameters identification is made [150]. Also, the measurements were made using an instrument that has a $0.7\,MPa$ resolution, and while averaging over hundreds of measurements greatly compensates this gap, there is still an uncertainty over the validity of the measurements.

The objective behind the elaboration of this model was to allow an iterative design, or ideally a parametric optimization, and use it to build a transducer that is fully adapted to its projected use. And this model enables this, as it allows to visualize the impact of all parameters on every system variable, like the pressure

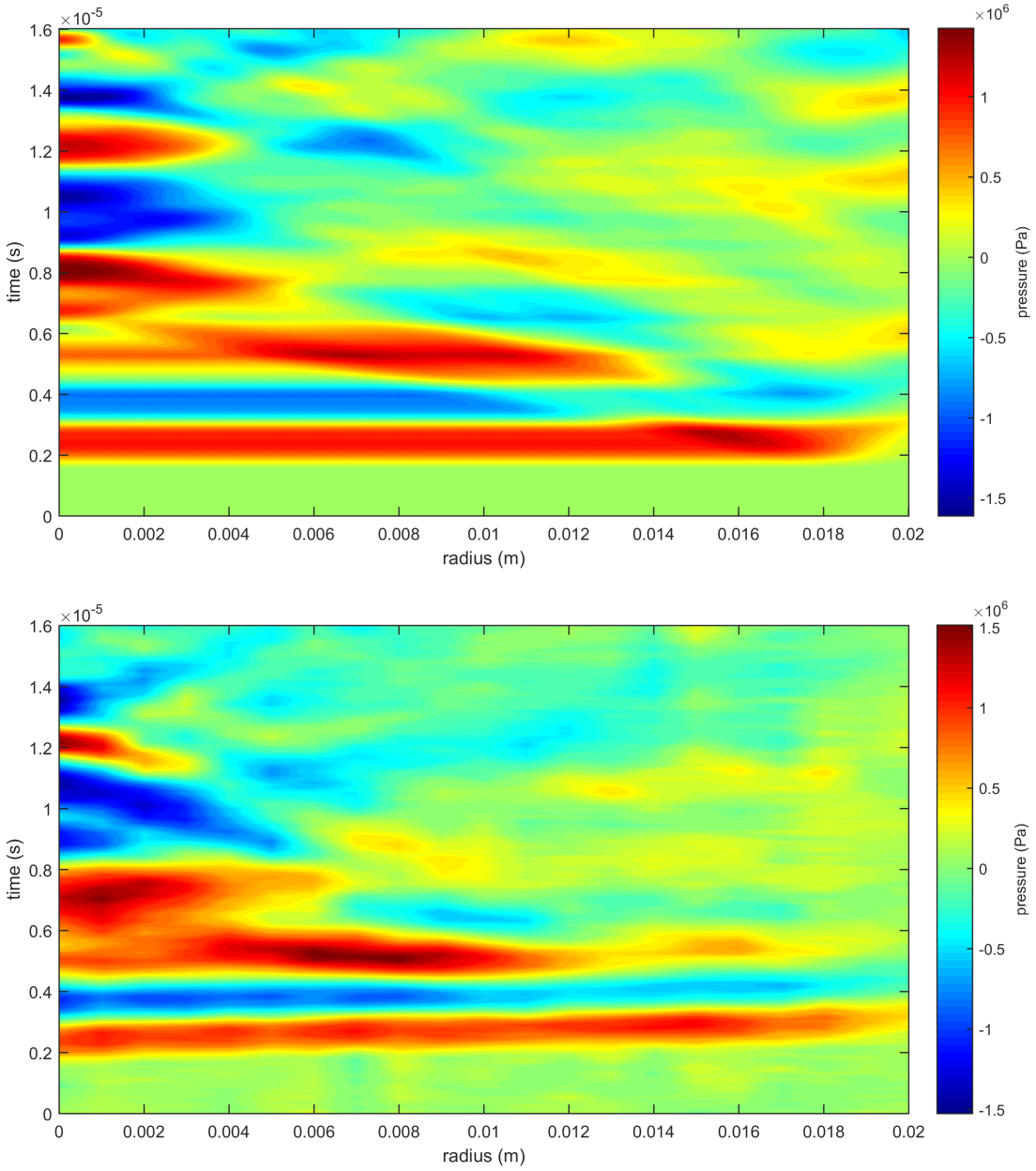

FIGURE 4.5: The calculated pressure field (top) and the measured pressure field (bottom).

field and the electrical boundary as shown earlier, but also the stress inside the solid domain like in fig. 4.7, where in that case the maximum Von Mises stress is close to the estimated yield strength of the PZT-4 (31.2 MPa [151]), the current (fig. 4.8) and the particle velocity (fig. 4.9).

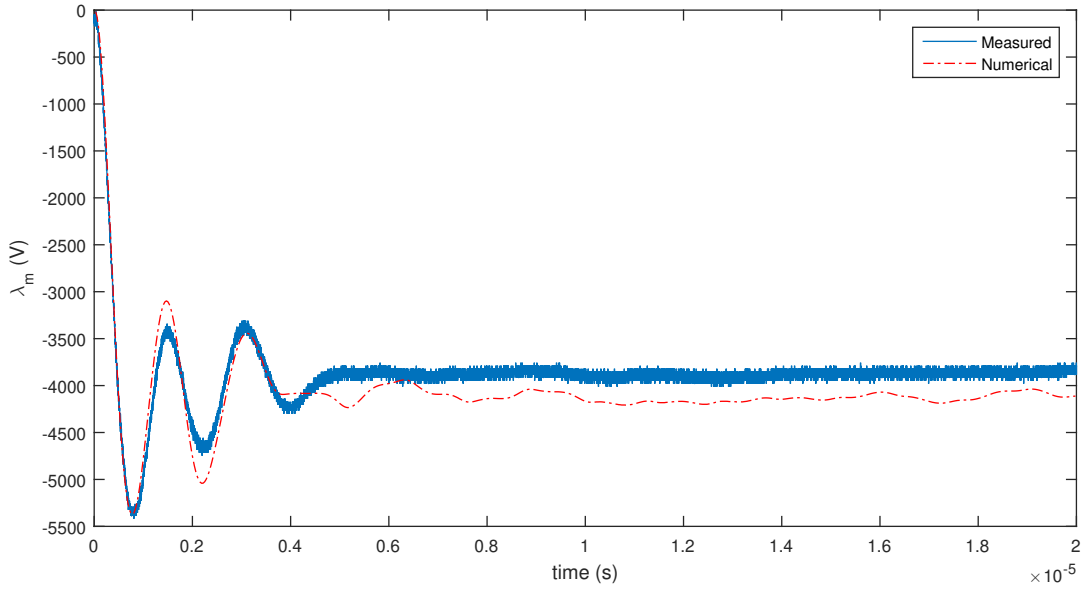

FIGURE 4.6: The electrical potential at the boundary Γ_v.

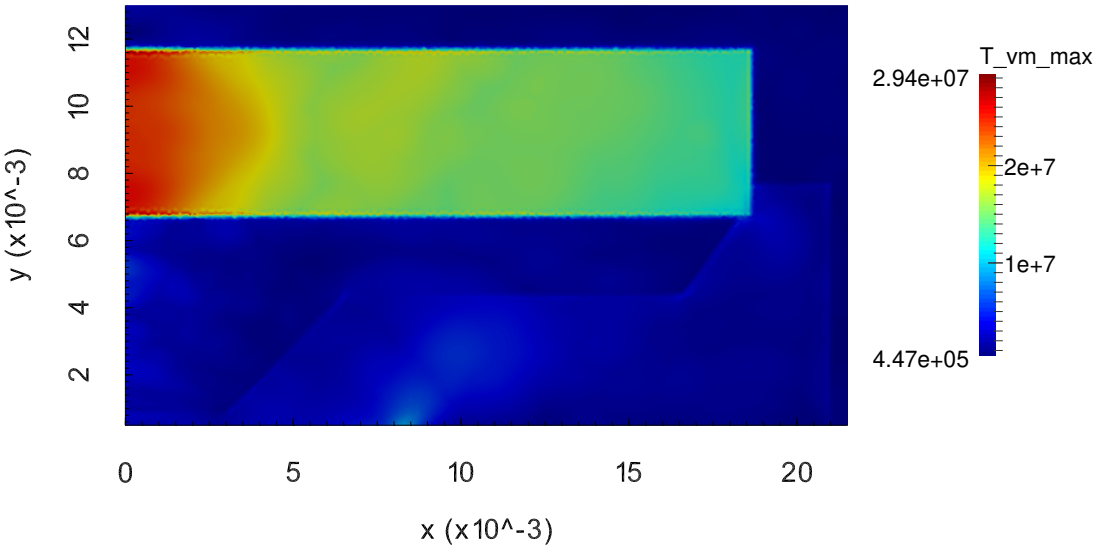

FIGURE 4.7: Maximum Von Mises stress in the solid domain.

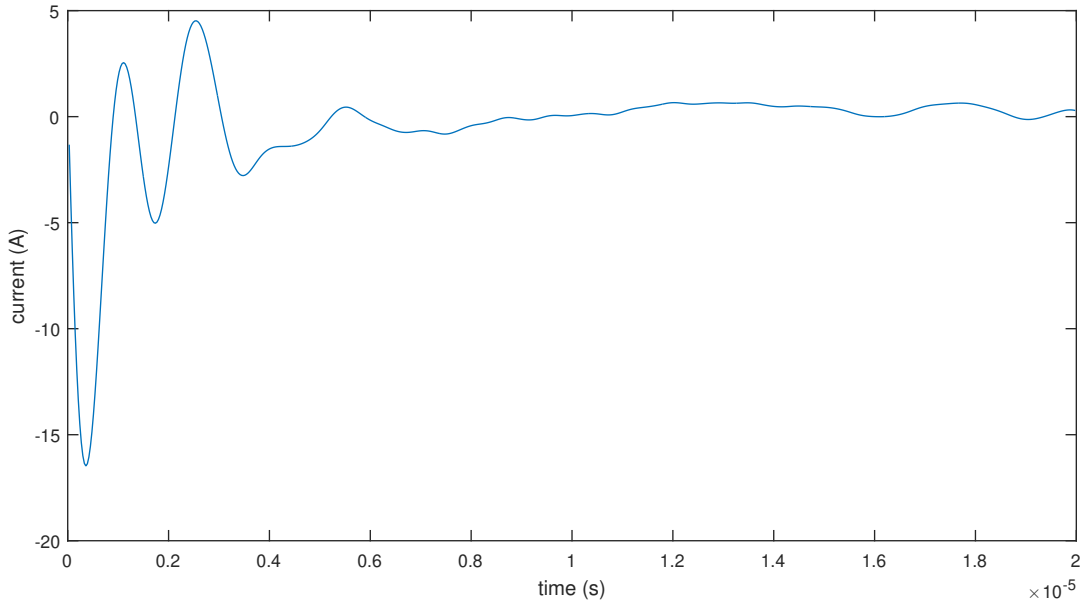

FIGURE 4.8: Current in the feeding circuit.

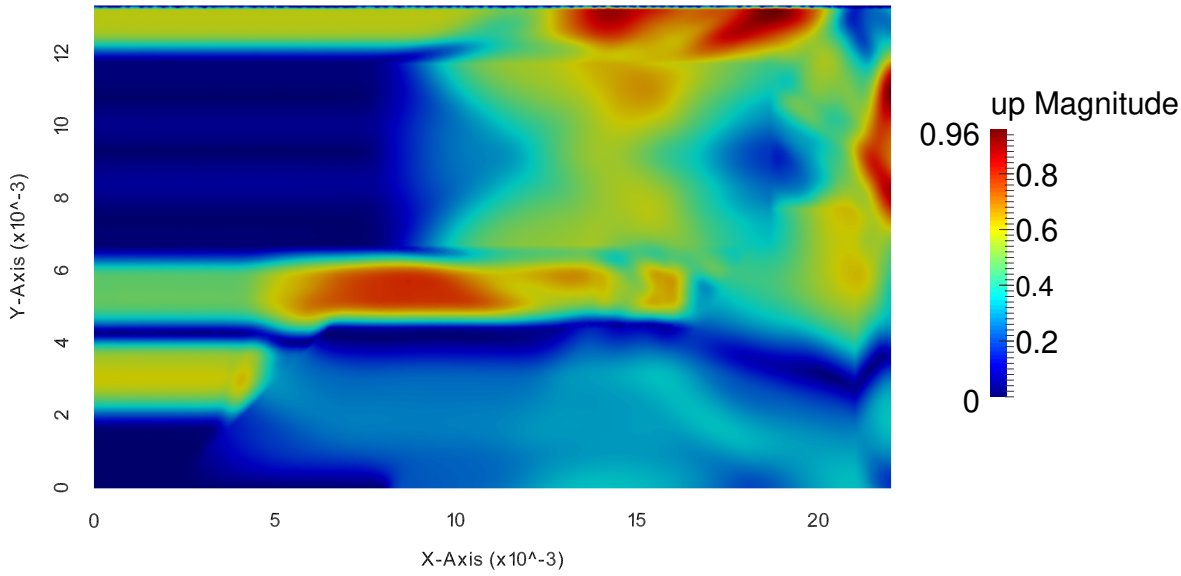

FIGURE 4.9: Magnitude of the particle velocity ($\|\dot{\mathbf{u}}\|$) at $t = 3\,\mu s$ in the solid domain.

4.5 Parametric optimization

The objective of a parametric optimization is to find the minimum (or maximum) of a real function, called objective function or functional, for a certain set of parameters. The optimization problem can be generalized as:

$$\begin{aligned} \underset{\mathbf{m}}{\text{minimize}} \quad & J(\mathbf{y}, \mathbf{m}) \\ \text{subject to} \quad & F(\mathbf{y}, \mathbf{m}) = 0 \\ & g(\mathbf{y}, \mathbf{m}) \geq 0 \end{aligned}$$

In our problem, $\mathbf{y}$ represents a vector of resulting field values (*e.g.* u_i, p, q), $\mathbf{m}$ is the vector of parameters (*e.g.* L, R, ...), J is the functional, F represents the PDE problem (*e.g* (4.14) to(4.30)) and g is a vector containing the inequalities constraints (*i.e.* the bounds of the parameters). The functional can also be reduced to a pure function of the parameter by posing $\hat{J}(\mathbf{m}) = J(\mathbf{y}(\mathbf{m}), \mathbf{m})$, which is called reduced functional.

There is a lot of different ways to solve this optimization problem, but since a finite element model exist to solve the PDE problem and seems differentiable on most parameters of interest, a gradient-based optimization algorithm using the adjoint method is considered.

4.5.1 The adjoint method

A gradient-based optimization algorithm uses the first derivative of the reduced functional, *i.e.* $\mathrm{d}\hat{J}(\mathbf{m})/\,\mathrm{d}\mathbf{m}$, to choose the step and direction of the next iteration. Using the chain rule on the functional gradient yields:

$$\frac{\mathrm{d}\hat{J}}{\mathrm{d}\mathbf{m}} = \frac{\partial J}{\partial \mathbf{m}} + \frac{\partial J}{\partial \mathbf{y}} \frac{\mathrm{d}\mathbf{y}}{\mathrm{d}\mathbf{m}} \tag{4.53}$$

While computing $\partial J/\partial \mathbf{m}$ and $\partial J/\partial \mathbf{y}$ is usually simple since J is a closed-form expression depending of $\mathbf{y}$ and $\mathbf{m}$, computing the solution jacobian $\mathrm{d}\mathbf{y}/\,\mathrm{d}\mathbf{m}$ is a very costly operation if the number of parameters is high: it would mean solving M times a problem of the same computational cost of the PDE problem $F(\mathbf{y}, \mathbf{m}) = 0$, where M is the size of the vector $\mathbf{m}$. Instead, the gradient of $\hat{J}$ is rewritten as:

$$\frac{\mathrm{d}\hat{J}}{\mathrm{d}\mathbf{m}} = \frac{\partial J}{\partial \mathbf{m}} - \frac{\partial J}{\partial \mathbf{y}} \left(\frac{\partial F(\mathbf{y}, \mathbf{m})}{\partial \mathbf{y}} \right)^{-1} \frac{\partial F(\mathbf{y}, \mathbf{m})}{\partial \mathbf{m}} \tag{4.54}$$

taking the adjoint of (4.54) yields:

$$\frac{\mathrm{d}\hat{J}}{\mathrm{d}\mathbf{m}}^{*} = \frac{\partial J}{\partial \mathbf{m}}^{*} - \frac{\partial F(\mathbf{y}, \mathbf{m})}{\partial \mathbf{m}}^{*} \frac{\partial F(\mathbf{y}, \mathbf{m})}{\partial \mathbf{y}}^{-*} \frac{\partial J}{\partial \mathbf{y}}^{*} \tag{4.55}$$

then isolating the solution of the inverse jacobian on a vector $\boldsymbol{\lambda}$:

$$\frac{\partial F(\mathbf{y}, \mathbf{m})}{\partial \mathbf{y}}^{*} \boldsymbol{\lambda} = \frac{\partial J}{\partial \mathbf{y}}^{*} \tag{4.56}$$

where $\boldsymbol{\lambda}$ is called the adjoint variable associated to $\mathbf{y}$. The ajoint variable $\boldsymbol{\lambda}$ is first computed and then its inner product with $-\partial F(\mathbf{y}, \mathbf{m})/\partial \mathbf{m}$ is computed in order to obtain the functional gradient needed by the optimization algorithm. The adjoint can also be calculated for time-domain problems (as done here).

In this work, the adjoints are calculated using dolfin-adjoint [152], which also provides an optimization framework [153] and checkpointing for time-domain sensitivity analysis [154].

4.5.2 Optimization of the piezoelectric transducer

In this section, multiple parametric optimization schemes using the finite element model detailed in section 4.2 are developed. While all of them could theoretically be united in one unique multi-objective optimization, the complexity of the functional in order to accurately obtain optimized value for each parameter of interest is too high and the risk of converging to a local minimum is increased. Also, all parameters may not be differentiable, thus requiring a non-gradient based, and therefore slower, optimization algorithm. This will be discussed more in detail later.

First, the parameters that are to be optimized must be selected:

- the values of E and ρ of the matching layer material;
- the discharge time t_p of the circuit;
- the values of E and ρ of the backing resin;
- the thickness h_{im} of the impedance matching layer;
- the values of the discharge circuit resistor R and inductance L.

Then, the characteristics that the optimized transducer should converge to are selected:

- maximum first peak pressure;
- minimum pressure for the rest of the waveform.

Remembering that the functional must be a scalar, the averaged squared pressure, defined as:

$$p_a^2 = \frac{1}{\int_{\Gamma_h} \mathrm{d}s} \int_{\Gamma_h} p^2 \, \mathrm{d}s \tag{4.57}$$

is a good indicator of the total output pressure of the transducer.

The first objective function can be synthesized with the following functional:

$$J_1 = -\int_{\Gamma_h} p^2(t_p + t_t) \, \mathrm{d}s \tag{4.58}$$

where t_t is the time needed for an acoustic wave to travel from Γ_{fsi} to Γ_h, which can be easily determined using the relation $c = \sqrt{M/\rho}$.

The second objective function is:

$$J_2 = \int_{2t_p+t_t}^{t_f} \int_{\Gamma_h} p^2 \, \mathrm{d}s \, \mathrm{d}t \tag{4.59}$$

where t_f is the final time.

Other parameters can be chosen, as, for example, the material of the casing, the shape of the piezoelectric ceramic, the shape of the impedance matching, as

well as other characteristics like the stress inside the ceramics or inside the plastic casing.

Optimization of the material of the impedance matching layer

The properties of the epoxy used in the acoustic impedance matching layer can be modified by adding metal powder, usually either tungsten or alumina. The modified mechanical properties of the epoxy mixture can be accurately calculated using a modified Reuss model from [155]:

$$\begin{aligned} \frac{1}{M} &= \frac{1 - V_f^{im}}{M_e} + \frac{V_f^{im}}{M_f} \\ M_e &= \frac{E_e(1-\nu_e)}{(1+\nu_e)(1-2\nu_e)} \\ M_f &= \frac{E_f(1-\nu_f)}{(1+\nu_f)(1-2\nu_f)} \end{aligned} \tag{4.60}$$

where M is the modified elastic modulus involving the Poisson's ratio as defined in [155], V_f^{im} is the volume fraction of metal powder, and the subscript 'e'and 'f' designate the epoxy and metal powders, respectively. The density of the mixture is calculated using a simple rule of mixture:

$$\rho = (1 - V_f^{im})\rho_e + V_f^{im}\rho_f \tag{4.61}$$

The material properties of the matching layer mostly influences the acoustic field after the first pulse, as the sum of the internal reflections (*i.e.* between the piezoceramic and the epoxy and then between the epoxy and the water) will almost stay constant as long as the epoxy acoustic impedance is bounded between the water and piezoceramic impedance. Therefore, the optimization objective here will be to lower the trailing pulses and as such the functional J_2 (4.59) is to be minimized here.

Optimization of the discharge time of the feeding circuit

Both the inductance L and the resistor R affect both the first peak pressure intensity and the waveform after it, and thus implies the need of multi-objective optimization in order to dimension them accordingly to the desired waveform. Therefore, for the optimization of the other parameters, a second order system approximation of $\phi(t)$, described in this section as $V(t)$, will be used as a boundary condition instead of the RLC circuit model. Once all the mechanical parameters are optimized, the parameters R and L will be fitted to the ideal values of $\phi(t)$.

The piezoelectric ceramic can be, in a simplistic manner, described electrically as a capacitor if not accounting for the mechanical effect, meaning that the voltage at its boundaries connected to the circuit described in section 4.1 can be modeled using a second order system equation response to a step input:

$$V(t) = V_\infty \left[1 - e^{\frac{-\zeta t}{\tau}} \left(\cos\left(\frac{\sqrt{1-\zeta^2}}{\tau} t \right) + \frac{\zeta}{\sqrt{1-\zeta^2}} \sin\left(\frac{\sqrt{1-\zeta^2}}{\tau} t \right) \right) \right] \tag{4.62}$$

where V_∞ is the voltage at $t \to \infty$ (and also the step value), τ is the natural period of oscillation and ζ is the damping. A representative plot of (4.62) is shown in fig. 4.10.

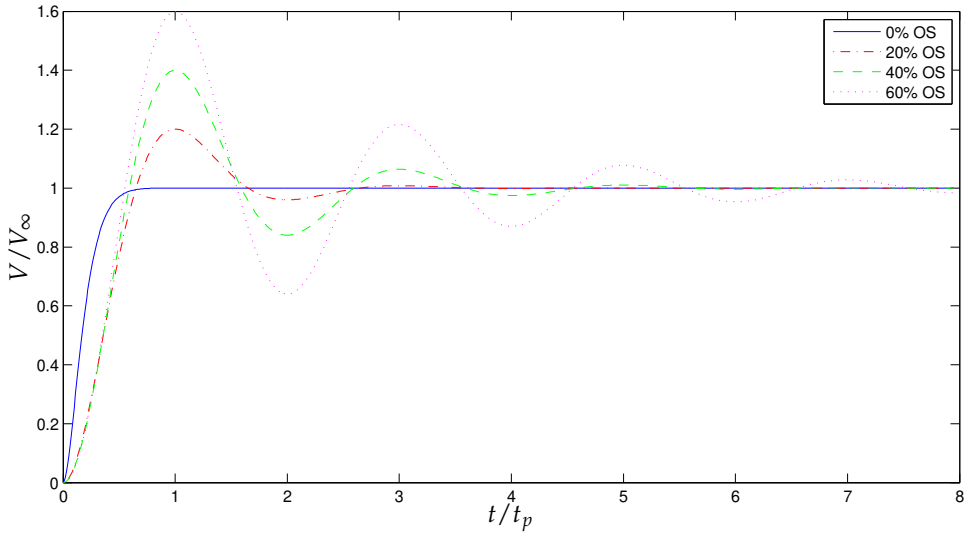

FIGURE 4.10: Second order system representation of $V(t)$ responding to a V_∞ step.

where t_p is the time to first peak, and we can define the overshoot 'OS' as $OS = V(t_p)/V_\infty$. The parameters t_p and OS are linked to (4.62) by:

$$t_p = \frac{\pi\tau}{\sqrt{1-\zeta^2}} \tag{4.63}$$

$$\zeta = \sqrt{\frac{\ln(OS)^2}{\pi^2 + \ln(OS)^2}} \tag{4.64}$$

From fig. 4.10, we can deduce that a high overshoot is beneficial for the first peak pressure, but also detrimental to minimizing the rest of the signal. Thus, ideally, the overshoot should be kept low (*e.g.* under 20%).

The weak form of the model, presented in (4.48), is modified accordingly, replacing the electrical current q with another Lagrange multiplier in order to impose the boundary condition weakly, as it is needed in order to run the optimization on it. Thus, the variational problem becomes: find $(u_i, p, \phi, \lambda_v, \lambda_m) \in [U, P, \Phi, \mathbb{R}, \mathbb{R}]$ such that $\forall (v_i, w, \psi, \Lambda_v, \Lambda_m) \in [\hat{U}, \hat{P}, \hat{\Phi}, \mathbb{R}, \mathbb{R}]$:

$$\int_{\Omega_s} \rho \ddot{u}_i v_i \,\mathrm{d}x + \int_{\Omega_s \setminus \Omega_p} \left(2\mu S_{ij}(u) + \lambda S_{kk}(u)\delta_{ij}\right) S_{ij}(v) \,\mathrm{d}x + \int_{\Gamma_{\text{fsi}}} p v_i n_i \,\mathrm{d}s + \int_{\Omega_p} c^E_{ijkl} S_{kl}(u) S_{ij}(v) \,\mathrm{d}x + \int_{\Omega_p} e_{kij} \phi_{,k} S_{ij}(v) \,\mathrm{d}x + \int_{\Omega_p} e_{ikl} S_{kl}(u) \psi_{,i} \,\mathrm{d}x - \int_{\Omega_p} \varepsilon^S_{ik} \phi_{,k} \psi_{,i} \,\mathrm{d}x + \int_{\Gamma_v} (\phi - \lambda_m) \Lambda_m \,\mathrm{d}s + \int_{\Gamma_v} (\phi - \lambda_m) \psi \,\mathrm{d}s + \int_{\Omega_f} \ddot{p} w \,\mathrm{d}x + \int_{\Omega_f} c^2 p_{,i} w_{,i} \,\mathrm{d}x - \int_{\Gamma_{\text{fsi}}} \rho_f c^2 \ddot{u}_i n_i w \,\mathrm{d}s + (\phi - \lambda_v)\Lambda_v + \lambda_v \psi = V(t)\Lambda_v \quad (4.65)$$

The value of t_p can be optimized using the functional J_1 (4.58) with a fixed OS.

Optimization of the backing material

The optimization of the backing material is made the same way as for the impedance matching material in section 4.5.2, *i.e.* using a modified Reuss model to calculate the volume fraction V_f^b of metal needed. But in this case, the functional used for the optimization is J_2 (4.59) since the backing purpose is to minimize reflection from the other boundary of the piezoelectric ceramic.

Optimization of the thickness of the matching layer

Even with the optimization of the material of the matching layer, internal reflections inside this layer are non negligible and thus its thickness should be chosen accordingly. For this part and with this model, using the adjoint method can be challenging as remeshing between each iteration will be necessary. Thus, in this particular case only, a non-gradient optimization algorithm is used with the functional J_2 (4.59), and the matching layer is modeled with the linear acoustic equation (4.7), using the property $c_s = \sqrt{M/\rho}$, and the distinction between the fluid and the matching layer is made as presented in (4.66)(4.67).

$$\rho = \rho_s + H(y)\left(\rho_f - \rho_s\right) \quad (4.66)$$

$$c = c_s + H(y)\left(c_f - c_s\right) \quad (4.67)$$

where c_s is the sound speed inside the matching layer, c_f is the fluid sound speed, and $H(y)$ is defined as:

$$H(y) = \begin{cases} 0 & \text{if } y < h_{im} + h_0 \\ 1 & \text{if } y \geq h_{im} + h_0 \end{cases} \quad (4.68)$$

where y is the coordinate along the axisymmetric axis, h_{im} is the thickness of the impedance matching layer and h_0 is the coordinate of the boundary Γ_v in fig. 4.3, *i.e.* the interface between the piezoelectric disc and the matching layer. The fluid-structure interface is also set on Γ_v.

Optimization of the circuit components

As all the mechanical parameters are optimized using the second order system voltage boundary condition, the value of the resistor R and the inductance L are to be found in order for the discharge circuit to fit the ideal voltage while accounting for the mechanical effects. As such, the functional should be:

$$J_\phi = \int_0^{t_f} \int_{\Gamma_v} |\phi - V|^2 \, \mathrm{d}s \, \mathrm{d}t \tag{4.69}$$

However, the discharge time t_p should be as accurate as possible, and using the functional (4.69) could lead to a value of t_p that differs in a non-negligible way in order to compensate the mechanical vibration for $t > t_p$. Thus, weight are introduced in the functional:

$$J_\phi = \frac{\lambda_1}{t_p} \int_0^{t_p} \int_{\Gamma_v} |\phi - V|^2 \, \mathrm{d}s \, \mathrm{d}t + \frac{\lambda_2}{t_f - t_p} \int_{t_p}^{t_f} \int_{\Gamma_v} |\phi - V|^2 \, \mathrm{d}s \, \mathrm{d}t \tag{4.70}$$

where λ_1 and λ_2 are two real numbers such as $\lambda_1 > \lambda_2 > 0$.

Discussion

Here, there is a total of six parameters to optimize (V_f^{im}, t_p, V_f^b, h_{im}, R, and L) with three different functionals (J_1, J_2 and J_ϕ). As such, the parameters V_f^{im} and t_p can be optimized together with J_1, V_f^b and h_{im} with J_2 and finally R and L with J_ϕ. All parameters except h_{im} will be optimized using the BFGS algorithm (quasi-Newton method of Broyden, Fletcher, Goldfarb, and Shanno) and h_{im} with a modified Powell method (COBYLA) since $\mathrm{d}\hat{J}_2(h_{im}) / \mathrm{d}h_{im}$ is not available.

As a general rule in optimization, the initial values of each parameters and their bounds should be chosen carefully in order not to converge toward local minimal or unrealistic values:

- The volume fraction V_f should be comprised between 0 and 0.4, as recommended in [155];
- The discharge time t_p should be close to half the inverse of the central frequency of the piezoelectric ceramic disc;
- The thickness of the impedance matching layer should be lower than the wavelength calculated with the piezoelectric disc central frequency;
- The circuit components R and L could be estimated by solving the differential equation resulting of the circuit approximation of the piezoelectric transducer.

4.5.3 Results

Maximizing the first peak pressure

The first optimization run will be toward maximizing the first peak pressure, which is the most important feature of this particular piezoelectric transducer. Here, the value of the overshoot is fixed at 5%, the initial value of t_p is set at $1.25\,\mu s$ and bounded in $[0.5E-6, 2.0E-6]$.

The resulting optimal discharge time value is: $t_p = 0.891\,\mu s$.

Minimizing the pressure after the first peak

As discussed earlier, the pressure emitted by the transducer after the first pulse should be as low as possible. As such, the initial value of V_f^b is set to 0 and bounded in $[0.0, 0.4]$, the initial value of h_{im} is set at $1\,mm$ and bounded in $[0.0005, 0.004]$, and the volume fraction V_f^{im} initial value is set at 0 and bounded in $[0.0, 0.4]$. The materials chosen are the Stycast 2651 epoxy and tungsten powder ($< 1\mu m$), with mechanical properties detailed in table 4.3.

TABLE 4.3: Properties of the Stycast 2651 epoxy and tungsten powder.

$\rho_e(kg/m^3)$	$E_e(GPa)$	$\rho_f(kg/m^3)$	$E_f(GPa)$
1500	5.7	19300	411

The resulting optimal values are: $h_{im} = 2.36\,mm$, $V_f^b = 0.4$, and $V_f^{im} = 0.145$.

Optimization of the circuit components

As the piezoceramic disc is the same as in section 4.4, the initial values are $R = 80\,\Omega$ and $L = 40\,\mu H$, with R bounded in $[10, 300]$ and L in $[10E-6, 200E-6]$. The resulting optimal values are $R = 146.8\,\Omega$ and $L = 47\,\mu H$.

Experimental results

A piezoelectric transducer was build using the results of the preceding optimization. Its plastic casing was designed to allow two different epoxies for the front and backing layer. It was then 3D printed and is shown fig. 4.11.

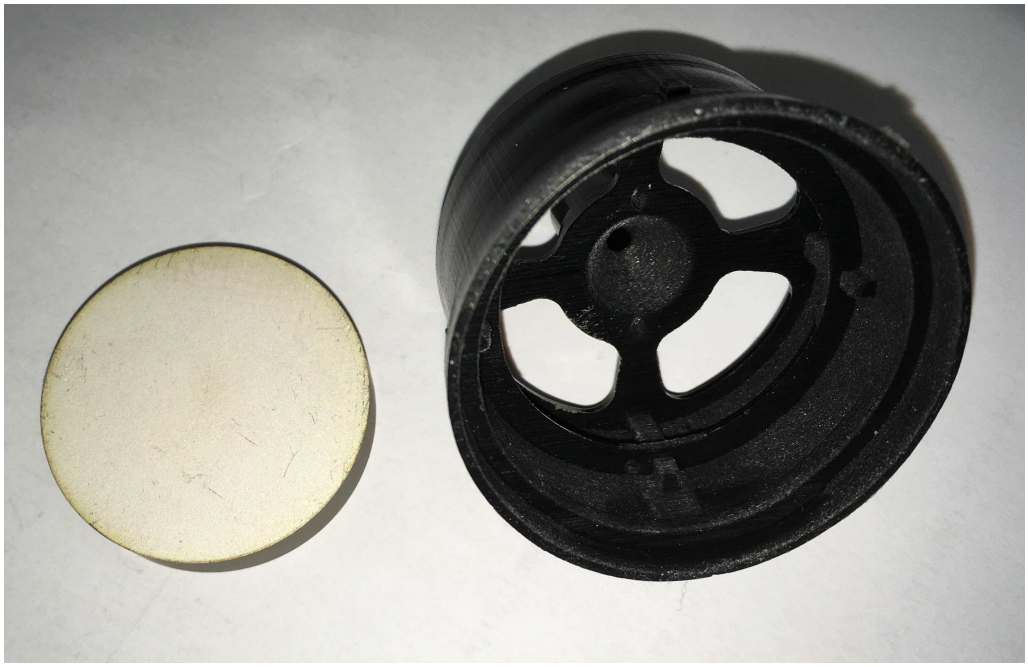

FIGURE 4.11: The 3D printed plastic casing of the transducer.

The piezoceramic disc was first glued to the casing using some raw Stycast 2651 epoxy, and then the front layer was filled with the mixture of 14.5% tungsten and Stycast 2651 and the backing with 40% tungsten and Stycast 2651. The face of the front layer was then machined using a lathe in order to get an accurate layer thickness and have a plane face. A photo of the finished transducer is shown in fig. 4.12.

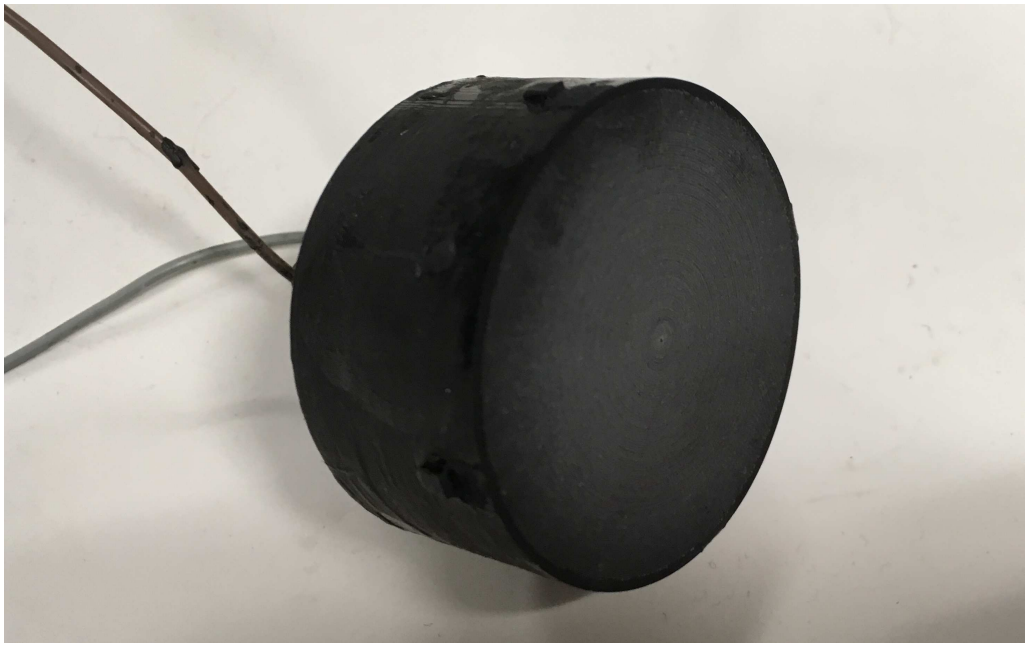

FIGURE 4.12: The finished optimized transducer.

As in section 4.3, measurements of the pressure at approximately 5 mm of the surface of the transducer were made with a fiber optic hydrophone, and then compared to the numerical results. Since the transducer was optimized with the average squared surface pressure, both experimental and numerical p_a^2 are compared in fig. 4.13.

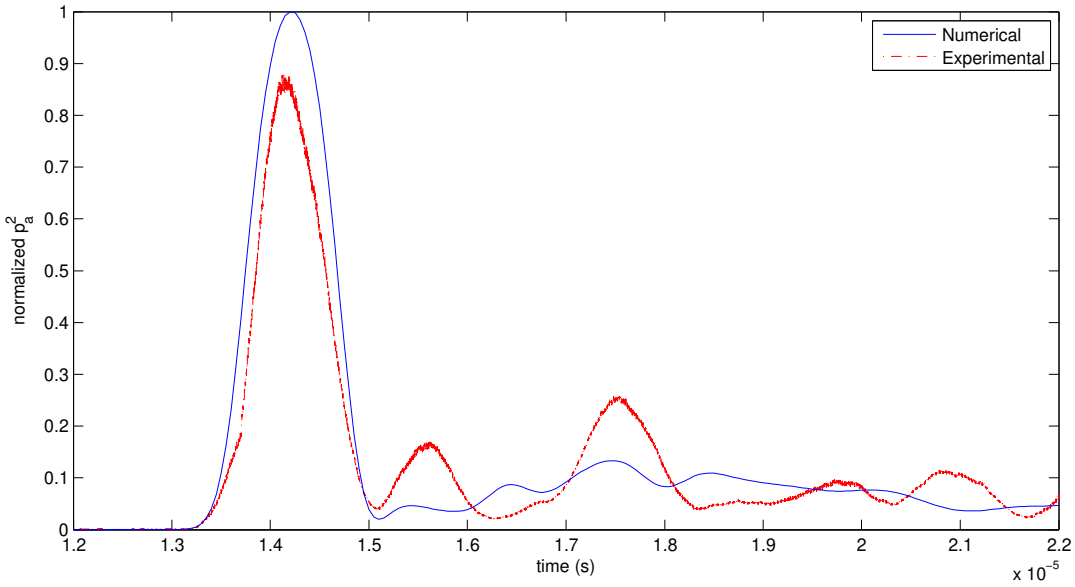

FIGURE 4.13: Normalized squared average surface pressure comparison between numerical and experimental results.

4.6 Discussion and conclusion

The experimental results are overall in good agreement with the optimization, since the transducer has a very low output after the first peak pressure. The difference in first peak pressure amplitude between the numerical and experimental results can be explained by the fact that the model does not account for the damping in the impedance matching layer, as it is mostly unknown and there is no simple and accurate model to account for the powder mixture contained in the epoxy. The effect of the powder mixture on the damping might be higher than expected, even with the very thin thickness of the front layer. The experimental results also show higher than expected pressure output after the first peak pressure, which may be the result of the inaccuracy of the modified Reuss model, but also might be due to air bubbles trapped in the backing epoxy, as the 40% tungsten mixture was very hard to degas properly.

While the optimization yielded a small gain (around 6%) in the first peak pressure maximum output and lowered the pressure peaks after that, those gains are too small to improve significantly a piezoelectric lithotripter based on the *EDAP-TMS* LT02. As discussed in the preceding chapter, the small diameter of the piezoelectric elements compared to the distance between them and the focus is also an important factor in the loss of pressure. A solution is to use focused elements that

are large enough to have the focus of the lithotripter inside their near field. However, larger elements need to be focused in order to have a high enough pressure at the focus of the lithotripter. As such, the next chapter will be dedicated to the optimization of acoustic lens.

Chapter 5

Shape optimization of lens-focused ultrasound transducers

5.1 Introduction

Focused transducers have applications in a wide range of fields such as non-destructive testing, medical imaging and therapy. In most cases, the transducers are made with curved ceramics, that focus the pressure at their geometrical focal point. The main disadvantage of curved ceramics is that they are usually very expensive and long to produce as they are not mass produced and need to meet specific attributes depending on the application.

An alternative is to use flat piezoelectric ceramics and to focus the pressure field with an acoustic lens instead. This method is already in use in, for example, medical imaging [156] and therapy [157]. The advantage of using flat piezoelectric ceramics combined with an acoustic lens over spherically curved elements is mainly economical, as flat ceramics are already produced in a great variety of shapes and sizes, however the trade-off is a lower heat dissipation in the ceramic, which can be problematic in, for example, medical therapy with high intensity transducers where the power output is high. Based on geometric acoustics, the design of such lenses is usually elliptical to avoid the aberration caused by spherical lenses [158], with the major and minor axis depending on the ratio of the sound speed in the propagating liquid and the lens material. However, while easy and fast to calculate, this shape might not be optimal depending on the application.

This chapter focuses on the parametric shape optimization of an acoustic lens combined with a flat piezoelectric ceramic transducer, in order to have the maximum output of pressure over a designated area. The numerical modeling, presented in the next section, is done using the finite element method and accounts for sound attenuation and the fluid-structure interface. The optimization problem is solved using a gradient-based optimization algorithm. In the majority of acoustic-structure problems, the acoustic field, modeled using the wave equation, and the elastic field, modeled with the equation of elasticity, are coupled explicitly by a surface integral on the boundary separating the materials [143]. This formulation was used successfully in multiple acoustic-structure shape optimization problems [159][160], however the main disadvantage of this explicit coupling is that remeshing is necessary after each optimization iteration, which

could be slow and generate some difficulties in case of large change of geometry. Another way of solving acoustic-structure interaction problem is to use a displacement/pressure (referenced as $\mathbf{u}/\mathrm{p}$) mixed finite element formulation [161], which was used in topology optimization of acoustic structure problems [162] as this formulation allows to implement the acoustic-structure interface implicitly (independently of the mesh).

Finally, the last section reports on two lens-focused transducers that were optimized and built. The pressure fields around the focus area were measured. The lenses were easily built using a rapid prototyping method such as 3D printing, but the materials available with this kind of manufacturing method may not be the most efficient for acoustical applications (low sound speed and high sound attenuation due to porosity). To compensate, the method presented here also allows to optimize multiple material lenses, where, for example, the 3D printed part could be filled with other materials like epoxy.

This chapter was published in IEEE Transactions on Ultrasonics, Ferroelectrics and Frequency Control [163].

5.2 Numerical Modeling

5.2.1 The u/p mixed finite element formulation

The governing equations of the $\mathbf{u}/\mathrm{p}$ formulation in the domain $\Omega_{up} \subset \mathbb{R}^d, d \in [2,3]$ without body forces and in harmonic regime are:

$$\omega^2 \rho \hat{\mathbf{u}} + \nabla \cdot \hat{\boldsymbol{\sigma}} = 0 \qquad \text{in } \Omega_{up} \tag{5.1}$$

$$\hat{\boldsymbol{\sigma}} = 2\hat{G}\left(\hat{\boldsymbol{\epsilon}} - \frac{1}{d}\left(\nabla \cdot \hat{\mathbf{u}}\right)\mathbf{I}\right) - \hat{p}\mathbf{I} \qquad \text{in } \Omega_{up} \tag{5.2}$$

$$\hat{p} = -\hat{K}\nabla \cdot \hat{\mathbf{u}} \qquad \text{in } \Omega_{up} \tag{5.3}$$

$$\hat{\boldsymbol{\sigma}} \cdot \boldsymbol{n} = \hat{\boldsymbol{h}} \qquad \text{on } \Gamma_h \tag{5.4}$$

$$\hat{\boldsymbol{u}} = \hat{\boldsymbol{u}}_0 \qquad \text{on } \Gamma_u \tag{5.5}$$

where ω is the angular frequency, ρ is the density, $\mathbf{n}$ is the normal on the boundary, $\hat{\mathbf{u}}$ is the complex displacement vector such as $\mathbf{u}(\mathbf{x},t) = \Re\left[\hat{\mathbf{u}}(\mathbf{x})e^{j\omega t}\right], \mathbf{x} \in \Omega_{up}$ and $j = \sqrt{-1}$, $\hat{\boldsymbol{\sigma}}$ is the stress tensor, $\hat{G}$ and $\hat{K}$ are the complex shear and bulk modulus, respectively, $\mathbf{I}$ the identity tensor, $\hat{p}$ is the complex pressure such as $p(\mathbf{x},t) = \Re\left[\hat{p}(\mathbf{x})e^{j\omega t}\right]$, and $\hat{\boldsymbol{\epsilon}} = \frac{1}{2}\left(\nabla\hat{\mathbf{u}} + (\nabla\hat{\mathbf{u}})^T\right)$ is the linear strain tensor. The boundary $\partial\Omega_{up}$ of the domain Ω_{up} is decomposed in two regions: Γ_u, where the prescribed displacement $\hat{\mathbf{u}}_0$ is imposed, and Γ_h, where the prescribed traction $\hat{\boldsymbol{h}}$ is imposed, such that $\Gamma_u \cup \Gamma_h = \partial\Omega_{up}$ and $\Gamma_u \cap \Gamma_h = \varnothing$. Using complex shear and bulk modulus within Hooke's law (5.2,5.3) allows us to account for the attenuation coefficient at the frequency of interest inside the lens, which can be high for some materials. They can be determined using the relation $\hat{G} = \rho\hat{v_s}^2$ and $\hat{K} = \rho(\hat{v_p}^2 - \frac{4}{3}\hat{v_s}^2)$, where $\hat{v_p}$ and $\hat{v_s}$ are the complex P-wave and S-wave speed at the frequency of interest, respectively.

By injecting (5.3) into (4.6), we can recognize the Hooke's law, and as such (5.1,4.6,5.3) are the classical linear elastic equations. Also, if the shear modulus $\hat{G}$ is set to zero, the Helmholtz equation can easily be found (see [162]). Thus, by using such properties, acoustic-structure interfaces can be defined implicitly.

In order to implement the $\mathbf{u}/\mathrm{p}$ formulation for finite elements, we need to write its variational formulation. First, we define the trial spaces as $\mathcal{V} = \{\hat{\mathbf{v}} \in \boldsymbol{\mathcal{H}}^1(\Omega_{up}) : \hat{\mathbf{v}} = \hat{\mathbf{u}}_0 \text{ on } \Gamma_u\}$ and $\mathcal{Q} = \mathcal{L}^2(\Omega_{up})$, and the test spaces as $\mathcal{V}_o = \{\hat{\mathbf{v}} \in \boldsymbol{\mathcal{H}}^1(\Omega_{up}) : \hat{\mathbf{v}} = 0 \text{ on } \Gamma_u\}$ and $\mathcal{Q}_o = \mathcal{L}^2(\Omega_{up})$, where $\mathcal{L}^2$ is the space of square integrable functions and $\boldsymbol{\mathcal{H}}^1$ is the Sobolev space where both $\hat{\mathbf{v}} \in \boldsymbol{\mathcal{H}}^1$ and its derivative are in $\mathcal{L}^2$. The variational problem is then written by multiplying the balance equation (5.1) by the conjugate of the displacement test function $\hat{\mathbf{v}}$, integrating over the domain Ω_{up}, integrating by part and injecting (4.6), and also multiplying (5.3) by the conjugate of the pressure test function $\hat{q}$ and integrating over the domain Ω_{up} . Finally, the variational problem reads: find $\hat{\mathbf{u}} \in \mathcal{V}$ and $\hat{p} \in \mathcal{Q}$ such that:

$$a(\hat{\mathbf{u}}, \hat{\mathbf{v}}) + b(\hat{p}, \hat{\mathbf{v}}) = L(\hat{\mathbf{v}}) \qquad \forall \hat{\mathbf{v}} \in \mathcal{V}_o \tag{5.6}$$

$$c(\hat{\mathbf{u}}, \hat{q}) + d(\hat{p}, \hat{q}) = 0 \qquad \forall \hat{q} \in \mathcal{Q}_o \tag{5.7}$$

where $a(\hat{\mathbf{u}}, \hat{\mathbf{v}})$, $b(\hat{p}, \hat{\mathbf{v}})$, $c(\hat{\mathbf{u}}, \hat{q})$ and $d(\hat{p}, \hat{q})$ are sesquilinear and $L(\hat{\mathbf{v}})$ is antilinear and defined as:

$$a(\hat{\mathbf{u}}, \hat{\mathbf{v}}) = \int_{\Omega_{up}} 2\hat{G}\hat{\boldsymbol{e}} : \nabla\bar{\hat{\mathbf{v}}}\,\mathrm{d}\mathbf{x} - \int_{\Omega_{up}} \omega^2\rho\hat{\mathbf{u}} \cdot \bar{\hat{\mathbf{v}}}\,\mathrm{d}\mathbf{x} \tag{5.8}$$

$$b(\hat{p}, \hat{\mathbf{v}}) = -\int_{\Omega_{up}} \hat{p}\nabla \cdot \bar{\hat{\mathbf{v}}}\,\mathrm{d}\mathbf{x} \tag{5.9}$$

$$c(\hat{\mathbf{u}}, \hat{q}) = \int_{\Omega_{up}} (\nabla \cdot \hat{\mathbf{u}})\,\bar{\hat{q}}\,\mathrm{d}\mathbf{x} \tag{5.10}$$

$$d(\hat{p}, \hat{q}) = \int_{\Omega_{up}} \frac{\hat{p}}{\hat{K}}\bar{\hat{q}}\,\mathrm{d}\mathbf{x} \tag{5.11}$$

$$L(\hat{\mathbf{v}}) = \int_{\Gamma_p} \hat{\boldsymbol{h}} \cdot \bar{\hat{\mathbf{v}}}\,\mathrm{d}s \tag{5.12}$$

where $\hat{\boldsymbol{e}}$ is the deviatoric strain defined as:

$$\hat{\boldsymbol{e}} = \hat{\boldsymbol{\epsilon}} - \frac{1}{d}(\nabla \cdot \hat{\mathbf{u}})\,\mathbf{I} \tag{5.13}$$

While the boundary conditions for the $\mathbf{u}/\mathrm{p}$ formulation are the same as in the classical elastodynamics formulation, with the prescribed traction boundary set as a Neumann boundary condition and the prescribed displacement boundary set as a Dirichlet boundary condition, some precautions are to be made in the case of $\hat{G} = 0$, where $\mathbf{u} \cdot \mathbf{n} = \hat{u}_n$ has to be defined on the boundary in order to

avoid zero frequency modes, where the case $\hat{u}_n = 0$ is the hard wall (total wave reflection) boundary condition.

5.2.2 Perfectly matched layer for the u/p formulation

Unbounded problems are common in elastodynamics and acoustic problems. An efficient solution to simulate an unbounded domain in finite element analysis is to use an absorbing layer, where the incoming wave will be damped exponentially and thus generate almost no reflection. This method is called perfectly matched layers (PML) and was first introduced by Berenger for electromagnetic waves [164]. Inside the PML domain Ω_{pml}, the coordinates x_i are replaced by their stretched coordinates $\tilde{x}_i$, such as [165]:

$$\tilde{x}_i = \int_0^{x_i} \hat{\lambda}_i(s)\, \mathrm{d}s \tag{5.14}$$

from which we can write:

$$\frac{\partial}{\partial \tilde{x}_i} = \frac{1}{\hat{\lambda}_i} \frac{\partial}{\partial x_i} \tag{5.15}$$

where $\hat{\lambda}_i(x_i)$ is the coordinate stretching function, which we will define as in [166]:

$$\hat{\lambda}(x_i) = 1 + \frac{f_i(x_i)}{\hat{k}} - j\frac{f_i(x_i)}{\hat{k}} \tag{5.16}$$

where f is the attenuation function and $\hat{k}$ the complex wavenumber. Here, since the PML boundaries will be located on the acoustic domain (where the shear modulus G is null) and as we work in monofrequency, we choose the simple attenuation function $f_i(x_i) = \langle x_i - L_i \rangle / a_0$, where $\langle x \rangle = (x + |x|)/2$ and a_0 is chosen in order to have the lowest wave reflection.

In the case of an axisymmetric model (as of here), cylindrical coordinates (r, θ, z) and the properties $\frac{\partial}{\partial \theta} = 0$ and $\mathbf{u}_\theta = 0$ are applied, and therefore the operator $\tilde{\nabla}$, the strain tensor $\hat{\tilde{\boldsymbol{\epsilon}}}$ and the deviatoric strain tensor $\hat{\tilde{\boldsymbol{e}}}$ inside Ω_{pml} become:

$$\tilde{\nabla}\hat{\mathbf{u}} = \begin{bmatrix} \frac{1}{\hat{\lambda}_r}\frac{\partial \hat{u}_r}{\partial r} & 0 & \frac{1}{\hat{\lambda}_z}\frac{\partial \hat{u}_r}{\partial z} \\ 0 & \frac{\hat{u}_r}{\tilde{r}} & 0 \\ \frac{1}{\hat{\lambda}_r}\frac{\partial \hat{u}_z}{\partial r} & 0 & \frac{1}{\hat{\lambda}_z}\frac{\partial \hat{u}_z}{\partial z} \end{bmatrix} \tag{5.17}$$

$$\hat{\tilde{\epsilon}} = \frac{1}{2}\left(\tilde{\nabla}\hat{\mathbf{u}} + \left(\tilde{\nabla}\hat{\mathbf{u}}\right)^T\right) \tag{5.18}$$

$$\hat{\tilde{e}} = \hat{\tilde{\epsilon}} - \frac{1}{d}\left(\tilde{\nabla}\cdot\hat{\mathbf{u}}\right)\mathbf{I} \tag{5.19}$$

Taking account that $\mathrm{d}\tilde{\mathbf{x}} = \frac{\tilde{r}}{r}\hat{\lambda}_r\hat{\lambda}_z\,\mathrm{d}\mathbf{x}$, eqs. 5.8,5.9,5.10,5.11,5.12 inside Ω_{pml} become:

$$\tilde{a}(\hat{\mathbf{u}},\hat{\mathbf{v}}) = \int_{\Omega_{up}}\left[2\hat{G}\tilde{\hat{e}} : \tilde{\nabla}\bar{\hat{\mathbf{v}}} - \omega^2\rho\hat{\mathbf{u}}\cdot\bar{\hat{\mathbf{v}}}\right]\frac{\tilde{r}}{r}\hat{\lambda}_r\hat{\lambda}_z\,\mathrm{d}\mathbf{x} \tag{5.20}$$

$$\tilde{b}(\hat{p},\hat{\mathbf{v}}) = -\int_{\Omega_{up}}\hat{p}\tilde{\nabla}\cdot\bar{\hat{\mathbf{v}}}\frac{\tilde{r}}{r}\hat{\lambda}_r\hat{\lambda}_z\,\mathrm{d}\mathbf{x} \tag{5.21}$$

$$\tilde{c}(\hat{\mathbf{u}},\hat{q}) = \int_{\Omega_{up}}\left(\tilde{\nabla}\cdot\hat{\mathbf{u}}\right)\bar{\hat{q}}\frac{\tilde{r}}{r}\hat{\lambda}_r\hat{\lambda}_z\,\mathrm{d}\mathbf{x} \tag{5.22}$$

$$\tilde{d}(\hat{\mathbf{u}},\hat{q}) = \int_{\Omega_{up}}\frac{\hat{p}}{\hat{K}}\bar{\hat{q}}\frac{\tilde{r}}{r}\hat{\lambda}_r\hat{\lambda}_z\,\mathrm{d}\mathbf{x} \tag{5.23}$$

$$\tilde{L}(\hat{\mathbf{v}}) = 0 \tag{5.24}$$

5.2.3 Model and parametrization

The axisymmetric model used for the parametric shape optimization of the acoustic lens is presented in fig. 5.1, where $\Omega_f \cup \Omega_d = \Omega_{up}$, such that Ω_f is the acoustic medium (hence inside $\hat{G} = 0$) which also includes the area Ω_Φ in which the pressure is to be maximized, and Ω_d is the design subdomain where the lens is to be optimized. The domain Ω_p represents the piezoceramic, modeled using the variational formulation presented by Allik and Hughes [167]. An impedance matching layer could also be introduced at the boundary between Ω_p and Ω_d if desired.

Inside the design subdomain Ω_d, the boundary between two materials 1 and 2 (for example the acoustic fluid and the plastic of the lens), represented by their respective subdomains Ω_1 and Ω_2 is defined implicitly using a level-set function $\psi_{12}(\mathbf{x})$ defined in Ω_d as [168]:

$$\begin{cases} \psi_{12}(\mathbf{x}) = 0 & \text{if } \mathbf{x} \in \partial\Omega_1 \cap \Omega_2 \\ \psi_{12}(\mathbf{x}) < 0 & \text{if } \mathbf{x} \in \Omega_1 \\ \psi_{12}(\mathbf{x}) > 0 & \text{if } \mathbf{x} \in \Omega_2 \end{cases} \tag{5.25}$$

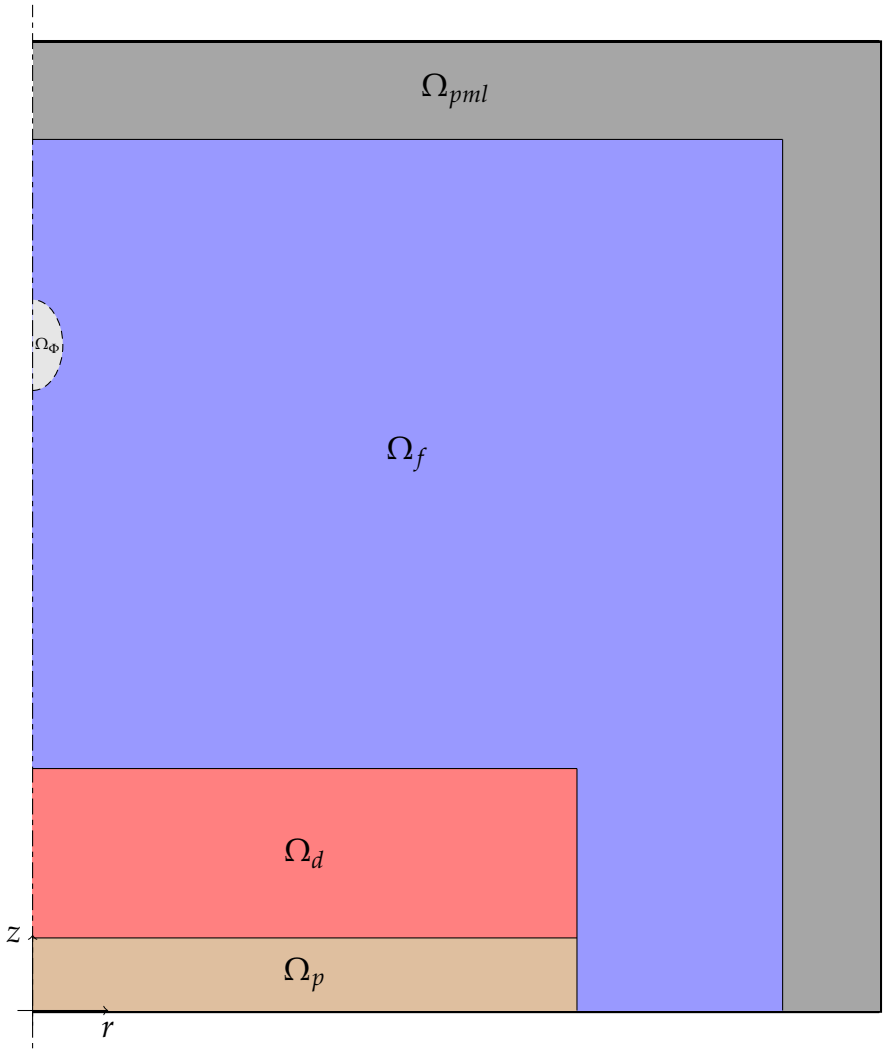

FIGURE 5.1: The simulation domain; Ω_f: acoustic medium, Ω_ϕ: functional area, Ω_d: design region, Ω_{pml}: PML boundaries region, Ω_p: piezoelectric ceramic.

In order to include this boundary inside the weak formulation presented in eqs. 5.8,5.9,5.10, the density ρ, the bulk modulus $\hat{K}$ and shear modulus $\hat{G}$ are defined as:

$$\rho(\mathbf{x}) = \rho_1 + H(\psi_{12}(\mathbf{x}))\,(\rho_2 - \rho_1) \tag{5.26}$$
$$\hat{K}(\mathbf{x}) = \hat{K}_1 + H(\psi_{12}(\mathbf{x}))\,(\hat{K}_2 - \hat{K}_1) \tag{5.27}$$
$$\hat{G}(\mathbf{x}) = \hat{G}_1 + H(\psi_{12}(\mathbf{x}))\,(\hat{G}_2 - \hat{G}_1) \tag{5.28}$$

where ρ_1, $\hat{K}_1$, $\hat{G}_1$ are the density, bulk modulus and shear modulus for the material 1 and ρ_2, $\hat{K}_2$, $\hat{G}_2$ are the density, bulk modulus and shear modulus for the material 2, respectively. The function H is a smooth Heaviside step function defined as :

$$H(\psi) = \begin{cases} 0 & \text{if } \frac{\psi}{\|\nabla\psi\|} < \alpha \\ 1 & \text{if } \frac{\psi}{\|\nabla\psi\|} > \alpha \\ \frac{1}{2} + \frac{3}{4}\left(\frac{1}{\alpha}\frac{\psi}{\|\nabla\psi\|} - \frac{1}{3\alpha^3}\frac{\psi^3}{\|\nabla\psi\|^3}\right) & \text{else} \end{cases} \tag{5.29}$$

where 2α is the width of the implicit boundary, which we set equal to the size of one element. The use of a smooth Heaviside function is important as it allows the evaluation of the sensitivity later during the optimization. It is also possible to introduce more materials inside the design subdomain as, for example, introducing a third material where the boundary between it and material 2 is defined by the level-set function ψ_{23}:

$$\rho(\mathbf{x}) = \rho_1 + H_{12}\,(1-H_{23})(\rho_2-\rho_1) + H_{23}\,(\rho_3-\rho_1) \tag{5.30}$$
$$\hat{K}(\mathbf{x}) = \hat{K}_1 + H_{12}(1-H_{23})\left(\hat{K}_2-\hat{K}_1\right) + H_{23}\left(\hat{K}_3-\hat{K}_1\right) \tag{5.31}$$
$$\hat{G}(\mathbf{x}) = \hat{G}_1 + H_{12}(1-H_{23})\left(\hat{G}_2-\hat{G}_1\right) + H_{23}\left(\hat{G}_3-\hat{G}_1\right) \tag{5.32}$$

where $H_{12} = H\left(\psi_{12}(\mathbf{x})\right)$ and $H_{23} = H\left(\psi_{23}(\mathbf{x})\right)$, and the coefficients of $\psi_{23} = 0$ are carefully bounded in order to avoid any crossing with $\psi_{12} = 0$.

In this article, the boundary between each material is defined using a polynomial of degree n: $P(r) = a_0 + a_1 r + \cdots + a_n r^n$, where the coefficients are to be optimized in order to get the maximum pressure at the focal area Ω_Φ. The choice of a polynomial shape is made as the acoustic lenses are usually of elliptic shape, which can be represented by a low-degree polynomial, and thus lessen greatly the number of parameters for faster optimization. The level-set function ψ is thus defined as:

$$\psi(r,z) = z - P(r) = z - (a_0 + a_1 r + \cdots + a_n r^n) \tag{5.33}$$

5.2.4 Implementation and optimization

The $\mathbf{u}/\mathrm{p}$ variational formulation, along with its PML and the piezoelectric formulation, were implemented using FEniCS (2017.1) [169]. In order to respect the inf-sup condition, appropriate finite elements must be chosen [170]. Here, we use the triangular Taylor-Hood element T6/3-c, with second-order continuous polynomial shape functions for the displacement and first-order continuous polynomial shape functions for the pressure as discontinuity in the pressure field is incompatible with the sensitivity evaluation. This also means that no discontinuity in pressure can exist, because a transition of $G_1 > 0$ to $G_2 = 0$ is not possible, 1 and 2 designating the material on each side of the boundary, 1 being a solid and 2 a fluid. Instead, we have to set $G_2 = \varepsilon G_1$, where ε is small (here we use $\varepsilon = 10^{-2}$) to ensure continuity.

The optimization problem here is to minimize the functional Φ defined as:

$$\Phi = \frac{-1}{\int_{\Omega_\Phi} \mathrm{d}\mathbf{x}} \int_{\Omega_\Phi} \hat{p}\bar{\hat{p}}\, \mathrm{d}\mathbf{x} \tag{5.34}$$

where the design variables are the coefficients of the polynomials in the level-set functions that define the boundaries between the materials inside Ω_d. The domain Ω_Φ represents the area where the maximum output possible for the transducer is desired, which does not necessarily represent the focal point of the transducer, but rather the maximum pressure achievable at this area with the actual setup (thus, the focal point of the transducer is usually slightly closer to the ceramic).

As we wish to use gradient-based optimization, we need to evaluate the derivatives of the functional Φ with respect to the design parameters. This is done with the adjoint method and automatic differentiation using the optimization framework dolfin-adjoint [152], [153], which evaluates automatically the sensitivity from the model implemented earlier in FEniCS. Finally, the optimization problem is solved using sequential quadratic programming, with its implementation *SLSQP* in the SciPy optimization package [171] that allows to set boundaries to the design parameters, which is essential here for multi-material lens design.

5.2.5 Material properties and experimental methods.

The piezoelectric ceramics used here were 37.3 mm diameter discs made of PZT-403 (Morgan Technical Ceramics, UK) with a thickness frequency of 400 kHz. The lenses are 3D printed with either a polyjet printer (Objet 30 Prime, Stratasys, USA) or a FDM (fused deposition modeling) printer (uPrint SE Plus, Stratasys, USA), and attached to the ceramic with an epoxy (Loctite Stycast 2651 MM, Henkel, Germany). In order to have the best acoustical properties, the 3D printers density was set to its maximum and the epoxy was degassed thoroughly (centrifuged 10 min at ∼2500 RPM before the casting and left 10 min at a relative pressure of ∼-0.9 bar after).

Measurements of the P-wave speed and attenuation were made and used for the modeling and optimization. The S-wave speed was calculated considering a 0.35 poisson ratio. The materials properties are listed in table 5.1.

The difference between the polyjet printed and the FDM printed ABS is quite high, and is mainly due to the manufacturing process itself as the FDM printed ABS is more porous.

All pressure field measurements were made with a capsule hydrophone (HGL-0200, Onda Corp, USA) and a computer controlled 3-axis positioning system with a spatial resolution between each measurements of 0.5 mm (the aperture of the hydrophone is 0.2 mm). Since the field measurements were hours long, the transducers were only sending bursts at low voltage and low burst rate in order to avoid any change of material properties due to the heat generated by the piezoelectric ceramic.

TABLE 5.1: Materials properties.

Material	$v_p\,(m/s)$	$v_s\,(m/s)$	$\rho\,(kg/m^3)$	Attenuation (Np/m) at $400\,kHz$
VeroWhitePlus (polyjet)	2375.8	1141.2	1160.0	15.79
ABSplus-P430 (FDM)	1718.7	825.4	1040.0	35.45
Stycast2651mm catalyst 24LV	2655.1	1275.4	1500.0	10.34
Water	1482.0	0.0	1000.0	0.0

5.3 Results

In this section, two lens-focused transducers, one only using ABS for the lens and another with a layer of ABS and a layer of epoxy, were designed for optimal use in ambient temperature water using the method presented in the preceding section, and measurements were made and compared to the numerical model. A photo of both transducer is shown in fig. 5.2:

FIGURE 5.2: Left: single material lens, right: bi-layer lens.

In both cases, the transducers were optimized at the frequency $400\,kHz$ (which corresponds to the thickness mode of the ceramic), with the objective function domain Ω_Φ defined as a ellipse with center on the axisymmetric axis z at a distance of $45\,mm$ to the surface of the piezoelectric ceramic. It was observed that Ω_Φ width (r-axis) did not influence the diameter of the focal beam, whereas its length (z-axis) did impact the length of the focal, thus the major axis (z-axis) and minor axis (r-axis) of the ellipse were set to $2\,mm$ and $1\,mm$, respectively, as we wish to

obtain the most focused beam possible. The design domain Ω_d was set as a rectangle of length 20 mm and height 16 mm for both transducers, which represents the maximum lens dimensions. The elements size for the numerical simulations was set to 0.15 mm, giving 25 elements per wavelength in water.

5.3.1 Single material lens

The transducer presented here was optimized on its boundary between the 3D printed ABS (VeroWhitePlus) and the water, referenced as material 1 and 2, respectively. The lens was attached to the surface of the piezoelectric ceramic (which represents the coordinate $z = 0$) with a layer of 1.9 mm thick epoxy. A fourth degree polynomial was used in the level-set function ψ_{12} and its optimized shape is plotted in fig. 5.3.

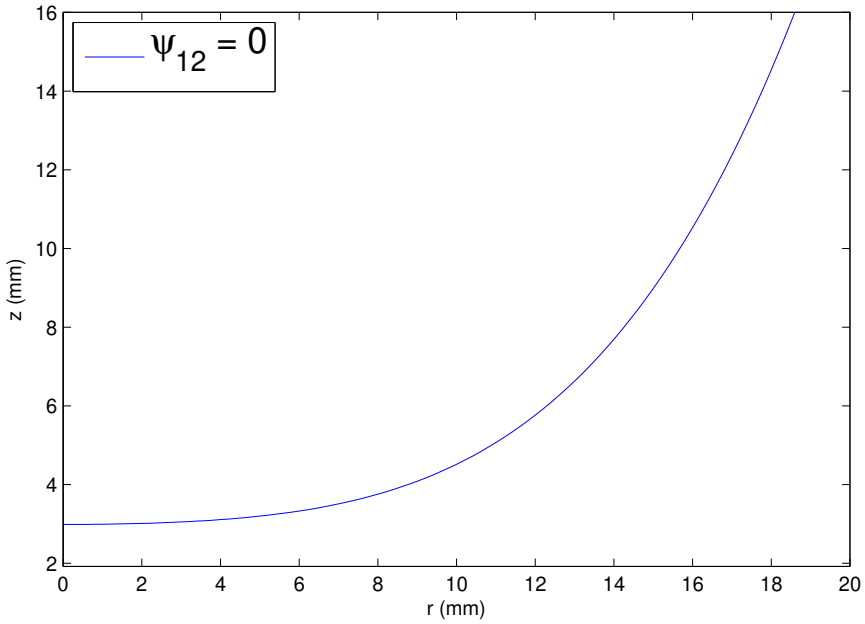

FIGURE 5.3: Optimized polynomial functions of the delimiting level-set functions for the single material lens.

A comparison between the predicted pressure field and the measurements of the built transducer is shown in fig. 5.4, and the focal beam characteristics are detailed in table 5.2.

TABLE 5.2: Numerical and experimental focal beam position and dimensions of the single material lens.

	Peak pressure depth (mm)	-6dB width (mm)	-6dB length (mm)
Numerical	41.3	5.7	34.6
Experimental	39.5	5.5	32.0

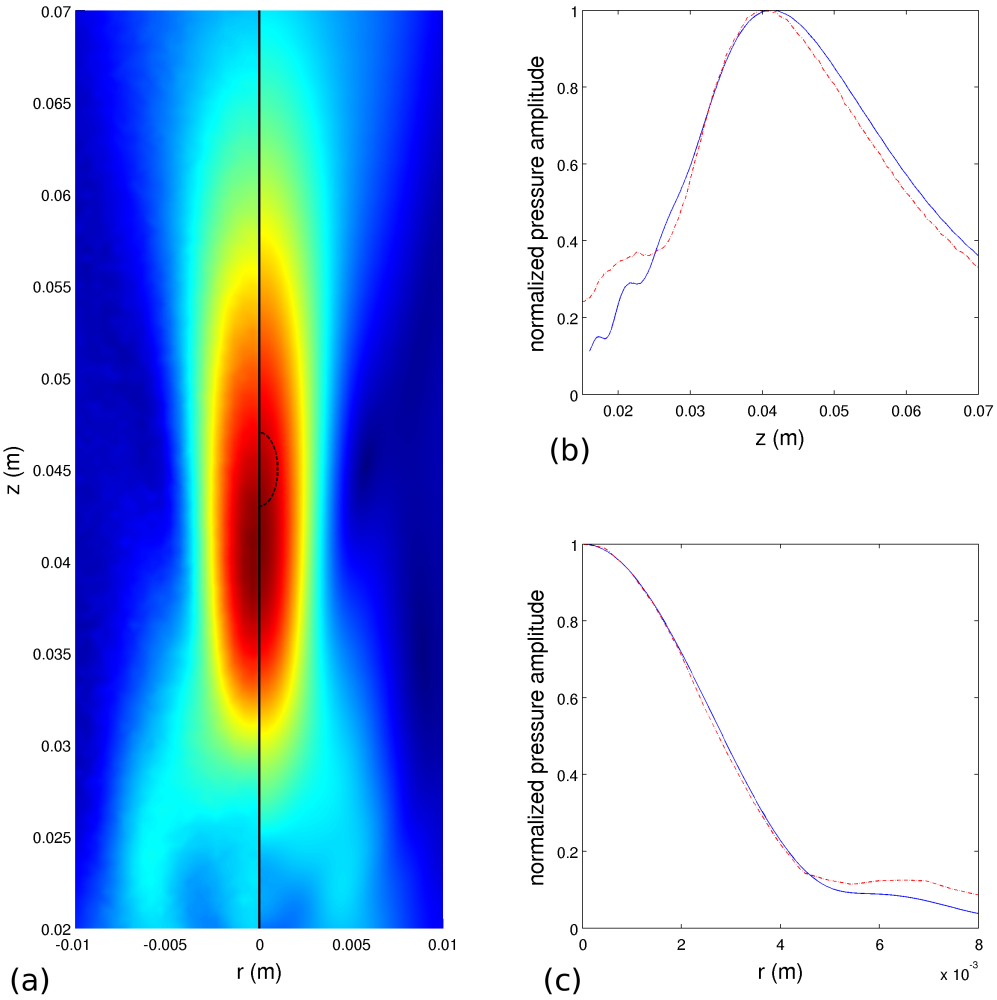

FIGURE 5.4: 2D focal beam comparison for the single material lens. (a) $r<0$: experimental measurements, $r>0$: numerical results, - - - Ω_Φ border. (b) Axial width, —— numerical, -·-·- experimental. (c) Radial width, —— numerical, -·-·- experimental.

5.3.2 Bi-layer lens

Here, the lens was made with two layers of different materials, the epoxy (Stycast 2651 MM) and the FDM printed ABS (ABSplus-P430), referenced as material 1 and 2, respectively, and the ABS shared a boundary with the water, referenced as material 3. Fourth degree polynomials were used in both level-set functions ψ_{12} and ψ_{23}, and their optimized shapes are plotted in fig. 5.5.

A comparison between the predicted pressure field and the measurements of the built transducer is shown in fig. 5.6, and the focal beam characteristics are detailed in table 5.3.

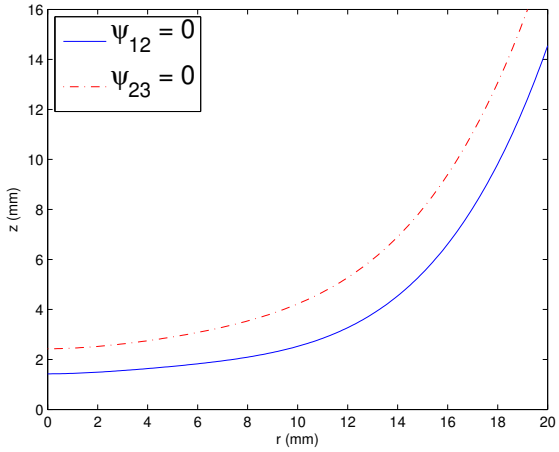

FIGURE 5.5: Optimized polynomial functions of the delimiting level-set functions for the bi-layer lens.

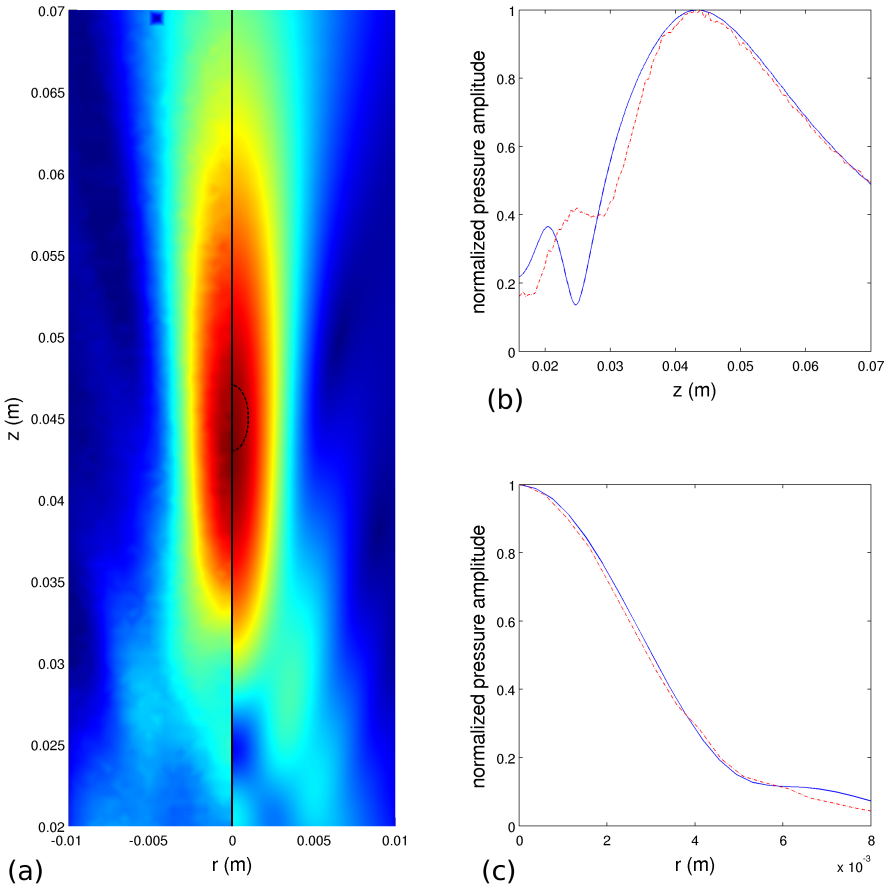

FIGURE 5.6: 2D focal beam comparison for the bi-layer lens. (a) r<0: experimental measurements, r>0: numerical results, - - - Ω_Φ border. (b) Axial width, —— numerical, -·-·- experimental. (c) Radial width, —— numerical, -·-·- experimental.

TABLE 5.3: Numerical and experimental focal beam position and dimensions of the bi-layer lens.

	Peak pressure depth (mm)	-6dB width (mm)	-6dB length (mm)
Numerical	43.6	6.0	40.3
Experimental	43.9	5.9	38.4

5.3.3 Discussion

In both cases, the experiments are in overall good agreement with the numerical results, with some small observable differences. In order to identify the origin of those differences, a comparison between a simulation of the single material lens without attenuation using the $\mathbf{u}/p$ formulation with implicit boundary and a simulation made with COMSOL Multiphysics®(COMSOL AB, Stockholm, Sweden) using linear elasticity for the solid and the Helmholtz equation for the fluid with explicit boundary coupling (i.e. using surface integral) for the fluid-structure interface is shown in fig. 5.7. The simulation using the $\mathbf{u}/p$ formulation with implicit boundary shows a slightly less focused beam and blurry side lobes compared to the simulation with the explicit fluid-structure interface, differences that were also observable experimentally in fig.5.4. Reducing further the element size in the simulation with implicit boundary does not improve the comparison, suggesting that those differences are mainly caused by the imposed continuity of the shear modulus at the implicit boundary between the solid and fluid.

Another source of error is the small variability in properties of both the ABS and the epoxy, and for the bi-layer lens we could also observe small infiltration of epoxy at the base of the FDM printed lens. As expected, the location of the peak pressure is slightly closer to the ceramics than the center of the functional area Ω_Φ, which was set to $z = 45\,mm$ here. The pressure output in the functional area is also 10.6% lower with the bi-layer lens than with the single material lens. This can be attributed to the very high attenuation inside the FDM printed ABS and also a larger focal area.

For both lenses, the optimization was run in two steps: first, the polynomial degree of the level-set functions was set to two and the initial conditions for the optimization were chosen almost randomly. This way, the convergence of the optimization run was fast and unlikely to stop at a local minima. Then, the degree of the polynomial was set to four and its initial value were set to the optimized second degree polynomial. Each optimization run needed between 30 to 50 iterations to converge with a tolerance of 10^{-6}, which represents around 2 to 4 hours on 12 cores on two Intel Xeon E5-2630v3 processors. We can also observe that the optimized FDM printed part of the bi-layer lens is basically a shell that is then filled with epoxy, as the FDM printed ABS has poor acoustical properties compared to the epoxy used here.

Furthermore, a comparison between the optimized single material lens from section 5.3.1 and an elliptically shaped lens designed using the formulas from [158] is shown in fig. 5.8.

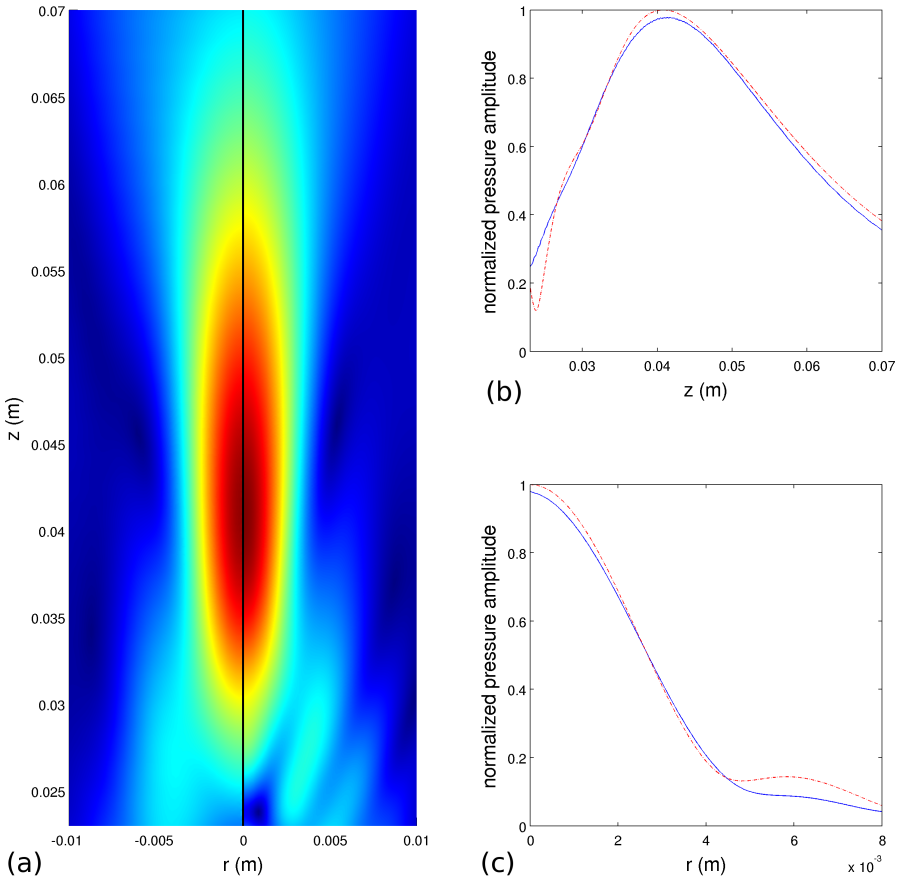

FIGURE 5.7: 2D focal beam comparison between numerical results using the $\mathbf{u}/p$ formulation with implicit boundary and numerical results using linear elasticity for the solid and the Helmholtz equation for the fluid with explicit boundary coupling. (a) $r < 0$: implicit boundary, $r > 0$: explicit boundary. (b) Axial width, —— implicit boundary, - - - - explicit boundary. (c) Radial width, —— implicit boundary, - - - - explicit boundary.

Using the $\mathbf{u}/p$ finite element model presented and validated earlier, a comparison between the focal beam of both transducers is shown in fig 5.9, in which we can observe that the optimized lens presents an overall more focused beam with slightly higher peak amplitude. The pressure gain in the area of the functional described in section 5.3 between the optimized lens and the elliptical lens is 5.1 %.

Therefore, using the optimization scheme to design acoustic lens for focused transducers presented here is beneficial, and can be further modulated by modifying the functional and functional area, depending on the application desired.

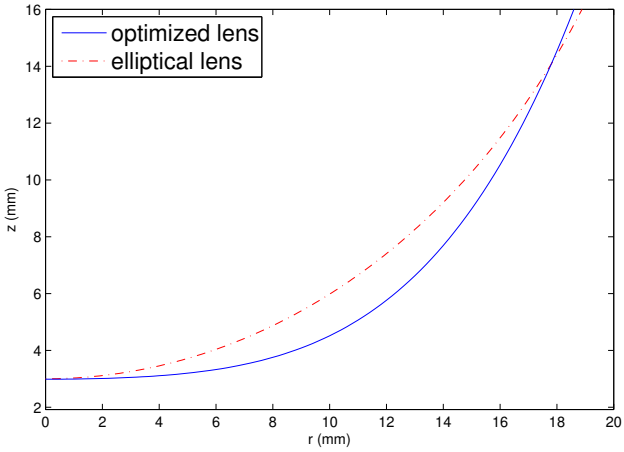

FIGURE 5.8: Comparison of the shape of the optimized single material lens from sec. 5.3.1 and the equivalent elliptical lens.

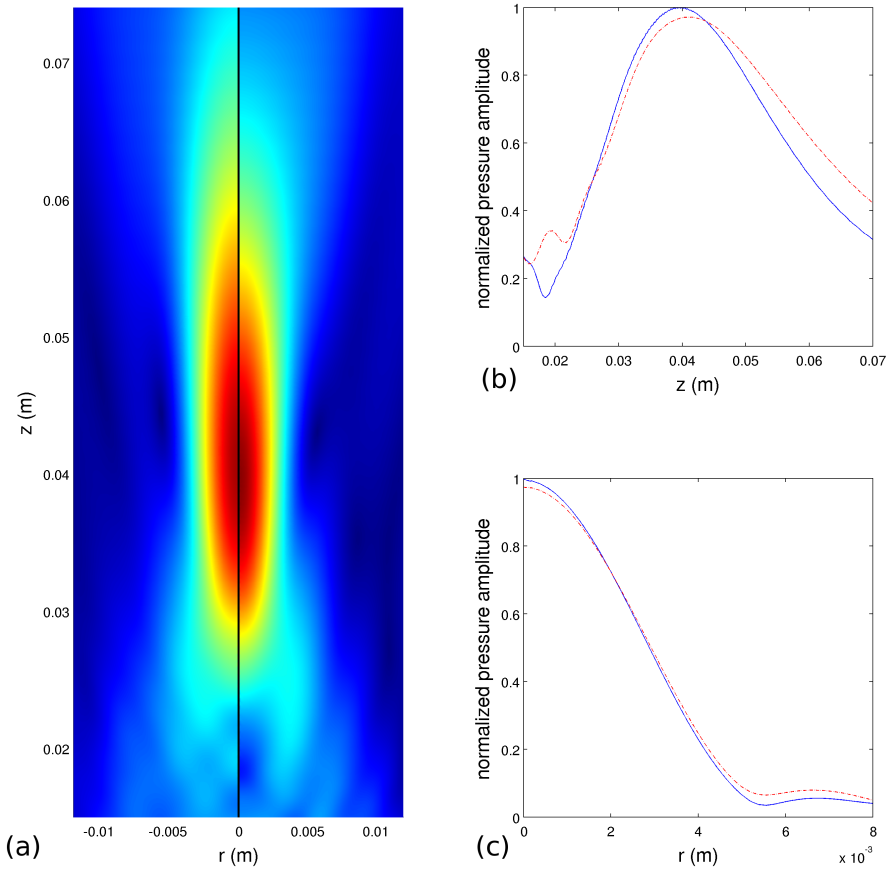

FIGURE 5.9: 2D focal beam comparison between the optimized single material lens and an equivalent elliptical lens. (a) $r<0$: elliptical lens, $r>0$: optimized lens. (b) Axial width, —— optimized lens, -·-·- elliptical lens. (c) Radial width, —— optimized lens, -·-·- elliptical lens.

5.4 Conclusion

The parametric optimization of the shape of an acoustic lens used in a piezoelectric focused transducer was presented. The whole transducer except its piezoelectric part was modeled using a displacement/pressure mixed finite element formulation accounting for sound attenuation, and the axisymmetric unbounded problem was solved by introducing perfectly matched layers to the $\mathbf{u}/p$ formulation. Two optimized transducers were built using different rapid prototyping methods, and showed that the modeling and optimization are both in good agreement with experimental results.

Chapter 6

Confocal lithotripsy

6.1 Introduction

Most of the current piezoelectric lithotripters are made by placing multiple piezoelectric elements inside a spherical recipient, yielding very high peak pressure in a very narrow focal zone at the geometric center of the sphere. As wide focus low pressure lithotripters show better performance, a solution to create a wide focusing with piezoelectric ceramics using a confocal setup is shown in this chapter. A confocal setup consists of multiple focused transducers positioned in a way that their beams cross around their focus, and already have application in medical ultrasound therapy[172]. Interestingly, similar confocal setups, called dual-pulse or tandem lithotripters, were already investigated in lithotripsy, where the main objective was to intensify and localize the cavitation phenomenon generated by the lithotripter with a second shock wave [173]. By setting the propagation axis of the focused transducers in the same plane, a wide focus on one axis could be obtained, while having a very narrow focus on the perpendicular axis. The narrow side would generate a high tensile stress gradient and thus shear stress on a large surface due to its perpendicular wide side, which should be very effective on brittle kidney stones. Here, a confocal setup of this type is evaluated with three focused transducers at different frequencies. Its model stone fragmentation capability *in-vitro* is compared to another confocal setup where four focused transducers are put in a spherical cap as in most piezoelectric lithotripters, thus generating a narrow high pressure focus. Their fragmentation effectiveness is also compared to two commercial lithotripters, one electroconductive and one piezoelectric.

This chapter was submitted for publication in the Journal of the Acoustical Society of America.

6.2 Design and manufacturing

6.2.1 Lens focused transducers

The confocal transducers are composed of multiple independently focused elements, where their focusing is obtained using plastic lenses combined with flat piezoelectric discs. The focal distance of the lenses was chosen to ensure a realistic treatment penetration depth for lithotripsy, and knowing that this focal

distance will shorten with non-linear effect, it was decided that the lenses would have a 200 *mm* focal distance under linear acoustic regime. Since the lens focusing is only efficient inside the near field of the flat piezoelectric disc, the diameter of all piezoceramic discs to be combined with the lenses was set to 92 *mm*. The shape of the lens was then calculated using finite element and parametric shape optimization, as described in the preceding chapter.

In this work three different frequencies are used: 400 kHz, 300 kHz and 220 kHz. The PZT material used for both the 400 and 300 kHz piezoceramics is the Pz27 (Meggit, Denmark), which is a soft PZT (NAVI II). The PZT material used for the 220 kHz piezoceramics is the C-9 (Fuji, Japan), a very soft ceramic, which was required as the thickness of the ceramics would be close to 10 *mm* and our feeding circuit was limited to 10 kV maximum high voltage power supply. However, using soft ceramics for delivering shock wave is not a problem as the ceramics only send a single pulse at a very low pulse repetition frequency (PRF) usually comprised between 0.5 and 2 Hz, and therefore the temperature inside the ceramics stays almost constant even during long treatments.

The 300 kHz ceramic discs were made using the 400 kHz ceramic discs, by drilling multiple holes into them to lower their central frequency, similarly to 1-3 composite. Modal simulation in Comsol was made to tune the size, number and repartition of the holes to reach 300 kHz. The resulting ceramics were made by piercing 131 4.8 mm diameter holes inside 400 kHz ceramic discs, effectively removing 36% of its mass. These holes are then filled with epoxy during the manufacturing of the transducer, and the resulting, composite-like, piezoceramics have a thickness frequency of 300 kHz and a larger bandwidth than the original 400 kHz ceramics.

As the objective was to try multiple confocal setups, the lens focused transducers were designed to be easily mounted and dismounted from the larger confocal lithotripsy transducer, and as such their design was inspired by a previous work by *Kim Y., et al* on modular transducers design [157]. The distance between the lens and the flat ceramic emitting side is chosen as half a wavelength inside the epoxy, in order to minimize the pressure after the first pulse, as in classical lithotripsy the waveform at the focal point is usually a singular pulse. The backing was also filled with the same epoxy in order to lower the reflection, and therefore the stress, inside the ceramic. The lens is 3D printed using a polyjet printer (Objet 30 Prime, Stratasys, USA) with the VeroBlackPlus material, and also serves as housing for the flat piezoceramic disc, with the spaces in-between filled with epoxy (Loctite Stycast 2651 MM, Henkel, Germany) degassed thoroughly by centrifuging it 10 min at ∼2500 RPM after mixing it, and then the filling was divided in 3 steps, where after each step the transducer is left 5 min at a relative pressure of ∼-0.9 bar. The lens has a thread on its side so it can be maintained in position on the transducer scaffold using a corresponding 3D printed nut. Finally, as the whole confocal transducer will be immersed in water during the experimental phase, the wires exit the transducer inside a hose connector to allow a silicone tube to be fitted, protecting the high voltage wires from the surrounding water. Photos of the manufactured transducers are shown in fig. 6.1.

FIGURE 6.1: Left: 300 kHz transducer before the epoxy filling. Right: 220 kHz transducer with its nut.

6.2.2 Transducer confocal setups

Two different confocal setups were studied here: one with three independent transducers aligned in the same plane, thus forming a C-shape, and one with four independent transducers set up in a more traditional spherical shape. The three transducers confocal scaffold was 3D printed in three separate supports for each transducer that can then be joined together. The transducer supports for the side transducers had the possibility to adjust the angle of incidence, while the center one had a thread to adjust the height of the transducer, allowing to try different focal distances and adjust for the non-linear effect. The four transducers confocal support was machined in aluminum with a diameter of 320 mm and a focal distance set to 180 mm. The treatment depth penetration (the maximum distance between the highest point of the confocal setup and its focal point) for the four transducers confocal was 134 mm, while the three transducers confocal was around 100 mm, but its C-shape could fit on the side of the patient during the treatment, thus greatly increasing the treatment depth penetration. Photographs of both confocal setups are shown in fig. 6.2.

The four transducers confocal is clearly not optimized since the ratio between active emitting surface and total surface is low (around 45%). The main objective behind this setup is to make a comparison between high pressure narrow focus lithotripsy, done with the four transducers confocal setup and wide focus low pressure lithotripsy, done with the three transducers confocal setup.

FIGURE 6.2: Top: Three transducers confocal setup. Bottom: Four transducers confocal setup.

6.3 Experimental characterization

6.3.1 Experimental setup

The electrical driving circuit for the transducers is shown in fig. 6.3. Two high voltage power supplies (HV) are used in the circuit, a positive one (T1EP 050 126 p, Technix, Creteil, France) that charges the capacitor C1 and a negative one (T1EP 100 505n, Technix, Creteil, France) that charges the capacitor C2. The capacitor C1 slowly charges the piezoelectric transducer Cp (i.e. with a much longer time than its resonant period) with a moderate high voltage opposite to the polarization in order to compress it when the fast high voltage transistor switch T1 (HTS 161-03,

Behlke, Kronberg im Taunus, Germany) is closed. The switch T1 then opens and shortly after the fast high voltage thyristor switch T2 (HTS 160-500-SCR, Behlke, Kronberg im Taunus, Germany) closes, releasing a very high voltage pulse in the same direction as the polarization of the piezoelectric disc, effectively generating a high surface pressure pulse [174]. The resistor R3 and the coil L control the charging time of the transducer, with R3 set to give a highly overdamped electrical signal, while the resistor R4 and the coil L control the pulse release and are set to give an underdamped electrical signal, with the peak time set to one fourth of the resonant period. While, logically, a critically damped signal would seem ideal in order to get lower pressure after the first peak pressure, it was found both numerically and experimentally that the high voltage overshoot was significantly beneficial to the first peak pressure while the following electrical oscillation were not significantly amplifying the second and third pressure pulses. The switch T2 only closes for a time slightly longer than the peak time, then the piezoelectric transducer Cp slowly discharges itself into the resistor R5 for around 200 ms.

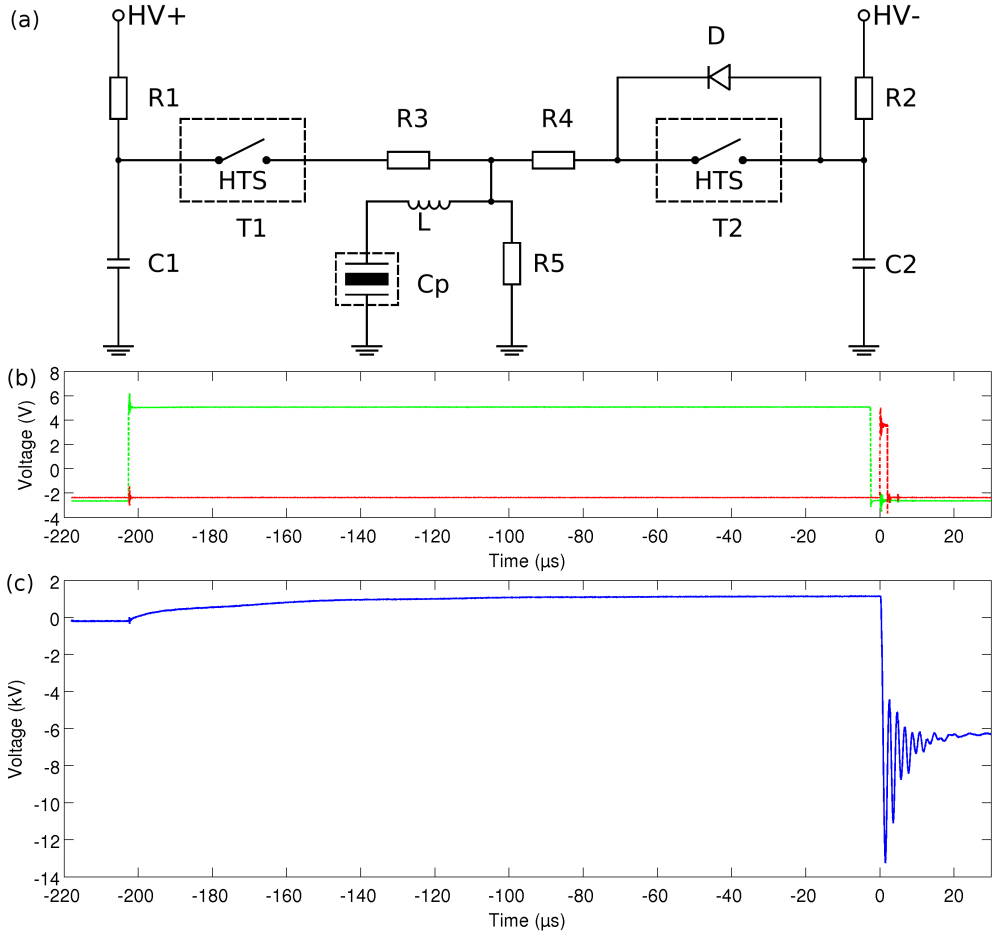

FIGURE 6.3: (a) Diagram of the transducer feeding circuit. (b) Logic signals sent to the high voltage switches, - - - electrical pre-strain logic signal to the T1 switch, -·-·- electrical discharge logic signal to the T2 switch. (c) Voltage applied to a 220 kHz transducer, with HV+ set to 1.5 kV and HV- to -6.5 kV.

In the following sections, all pressure measurements were made with a fiber optic hydrophone (FOPH 2000, RP-acoustics, Leutenbach, Germany) in degassed water (~2 mg/L O_2) and a computer controlled 3-axis positioning system. The focus characteristics presented here are only for the first pulse, i.e. the first peak positive pressure and the first peak negative pressure of the signal, as in some cases outside the focal point of the transducer the second peak positive pressure can be higher than the first one. Also, some measurements were made at lower power than the transducer maximum capability, presented as a percentage of the maximum voltage applicable to the transducer, as at such high pressure the fiber optic would break rapidly. Finally, all of the fiber optic hydrophones measurements are at least averaged 16 times to remove most of the noise characteristic of the hydrophone.

6.3.2 Pressure field of the lens focused transducers

Measurements of the pressure field around the focus of each lens focused transducer of each frequency at similar pressure level were made and are presented in fig. 6.4, where the depth is designated by the z-axis, where the origin is set to the surface of the piezoelectric disc that faces the lens and the r-axis is along the radius of the disc and has origin at its center. The focal beam characteristics of each transducer are detailed in table 6.1.

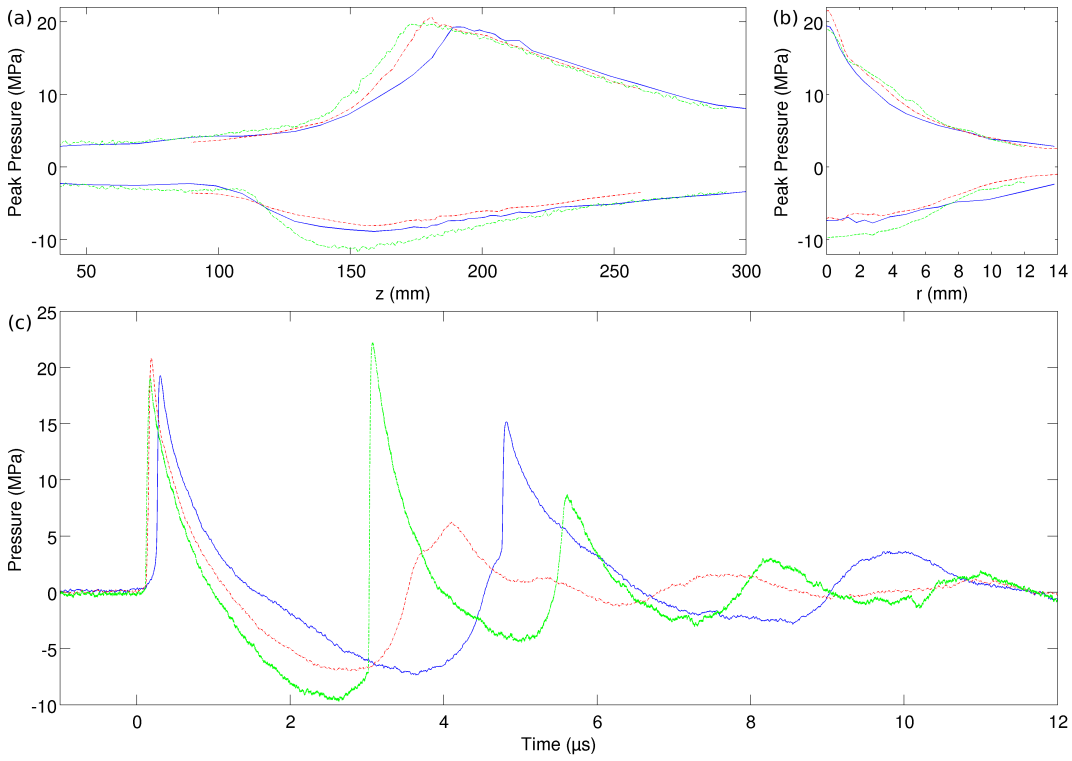

FIGURE 6.4: Acoustic characterization of the lens focused transducers, —— 220 kHz transducer, -·-·- 300 kHz transducer, - - - 400 kHz transducer. (a) Axial length of the focuses. (b) Radial width of the focuses. (c) Waveforms at the focal points.

TABLE 6.1: Focal beam characteristics of the lens focused transducers.

Transducer frequency (kHz)	Peak pressure depth (mm)	-6dB width (mm)	-6dB length (mm)	Peak pressure (MPa)
220	188	6.4	116	$19.3/-7.2$
300	180	7.4	119	$20.7/-6.9$
400	173	8.1	124	$19.7/-9.5$

As for each frequency the transducers are built with a different ceramic disc, the acoustic characteristics vary between them. First, as expected, the higher the frequency the stronger the non-linear effect, as we can notice in fig. 6.4.c with a steeper wavefront at $400\,kHz$ and $300\,kHz$ than at $220\,kHz$, or in fig. 6.4.a where the focal depth of the transducers is $12\,mm$, $20\,mm$ and $27\,mm$ closer to the piezoelectric disc, compared to the linear focal depth of $200\,mm$, at $220\,kHz$, $300\,kHz$ and $400\,kHz$, respectively. The $400\,kHz$ transducer is made with a Navy II piezoelectric ceramic, which has a relatively high resonant behavior, resulting in a very high second and third positive pressure peak, even with a half wavelength impedance matching between the lens and the ceramic, while the $300\,kHz$ transducer, where the piezoelectric disc is similar to a 1-3 composite as one third of its volume is filled with epoxy, presents almost a single pulse waveform due to its rather large bandwidth. Finally, as the $220\,kHz$ piezoelectric disc is made of a very soft PZT material, the second positive pressure peak, which has an amplitude of around two third of the first positive pressure peak, is in-between the 300 and 400 kHz transducers.

6.3.3 Pressure field of the 3 transducers confocal setup

The objective of this confocal setup was to obtain a large focal width, close to the dimension of renal calculi, and therefore the beams of the lens focused transducers cross slightly before before their individual focal depth (between 5 and 15 mm, depending on the frequency). In this section, the three transducers confocal setup z-axis was the same as the z-axis of the middle transducer, while the x-axis was perpendicular to the plane formed by the z-axis of the individual transducers and finally the y-axis was chosen to form a Cartesian coordinate system (i.e. perpendicular to both z and x). The pressure field around the focal point of the confocal setup for the different frequencies were measured and are presented in fig. 6.5, where the direction $z < 0$ point toward the middle transducer, and the characteristics of the focal beams are detailed in table 6.2.

Since the acoustic beam of the different lens focused transducers cross each other slightly before their focal point, the maximum pressure is lower than the sum of the maximum pressure of each transducer, however the resulting beam width on the x-axis is larger, except for the 400 kHz transducers, as the non-linear effect had already heavily reduced the peak pressure depth and thus the

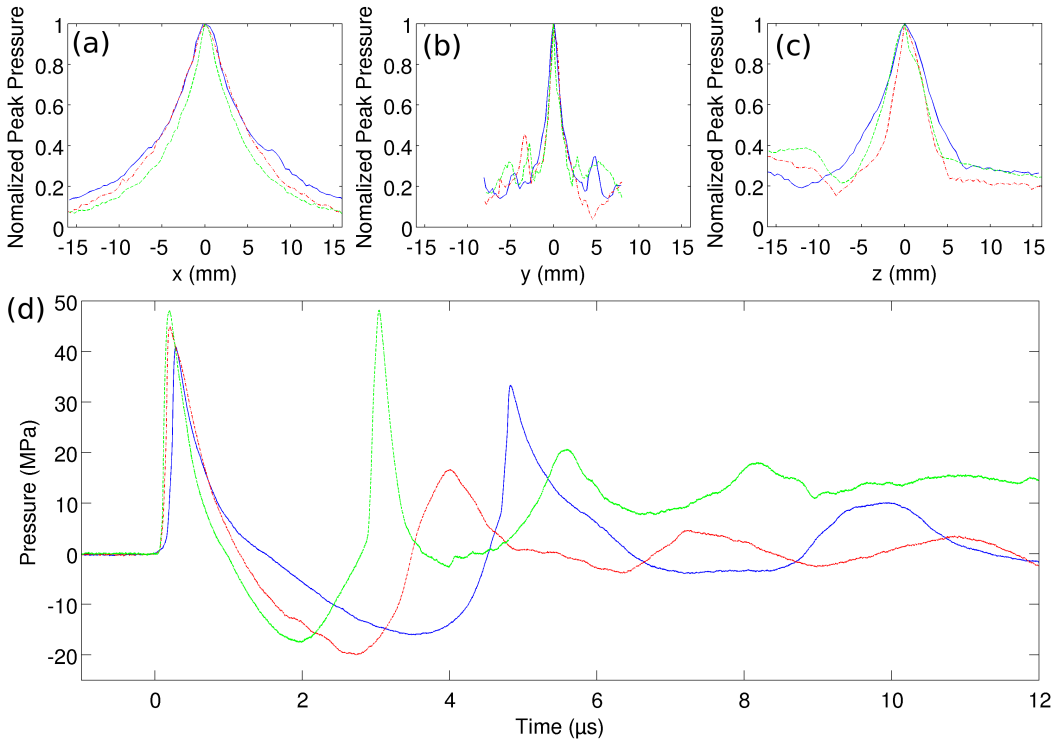

FIGURE 6.5: Acoustic characterization of the three transducers confocal setup, —— 220 kHz transducers, -·-·- 300 kHz transducers, - - - 400 kHz transducers. (a) Width of the focus on the x-axis. (b) Width of the focus on the y-axis. (c) Length of the focus on the z-axis. (d) Waveforms at the focal points.

TABLE 6.2: Focal beam characteristics of the three transducers confocal.

Transducers frequency (kHz)	-6dB x-axis width (mm)	-6dB y-axis width (mm)	-6dB z-axis length (mm)	Peak pressure (MPa)
220	9.6	2.2	8.3	40.9/ − 16.9
300	9.6	1.8	5.6	44.7/ − 19.7
400	7.1	1.7	7.1	48.1/ − 17.2

beams cross relatively closer to their focal point than at the other two frequencies. Another observation is that the wavefronts of the confocal in fig. 6.5.d are less steep than for the individual transducers in fig. 6.4.c while having more than twice the pressure. This phenomenon is characteristic of confocal setup, where the waveforms of each transducer are summed almost linearly [175]. Also, the trade-off of the mobility of the transducer supports is that the axis of propagation of each transducer are not perfectly co-planar, resulting in slightly lower peak pressures than expected. While the x-axis focus width is large, the y-axis focus is very narrow as seen on the pressure field plots for the 220 kHz transducers confocal setup at 80% of its max voltage in fig. 6.6.

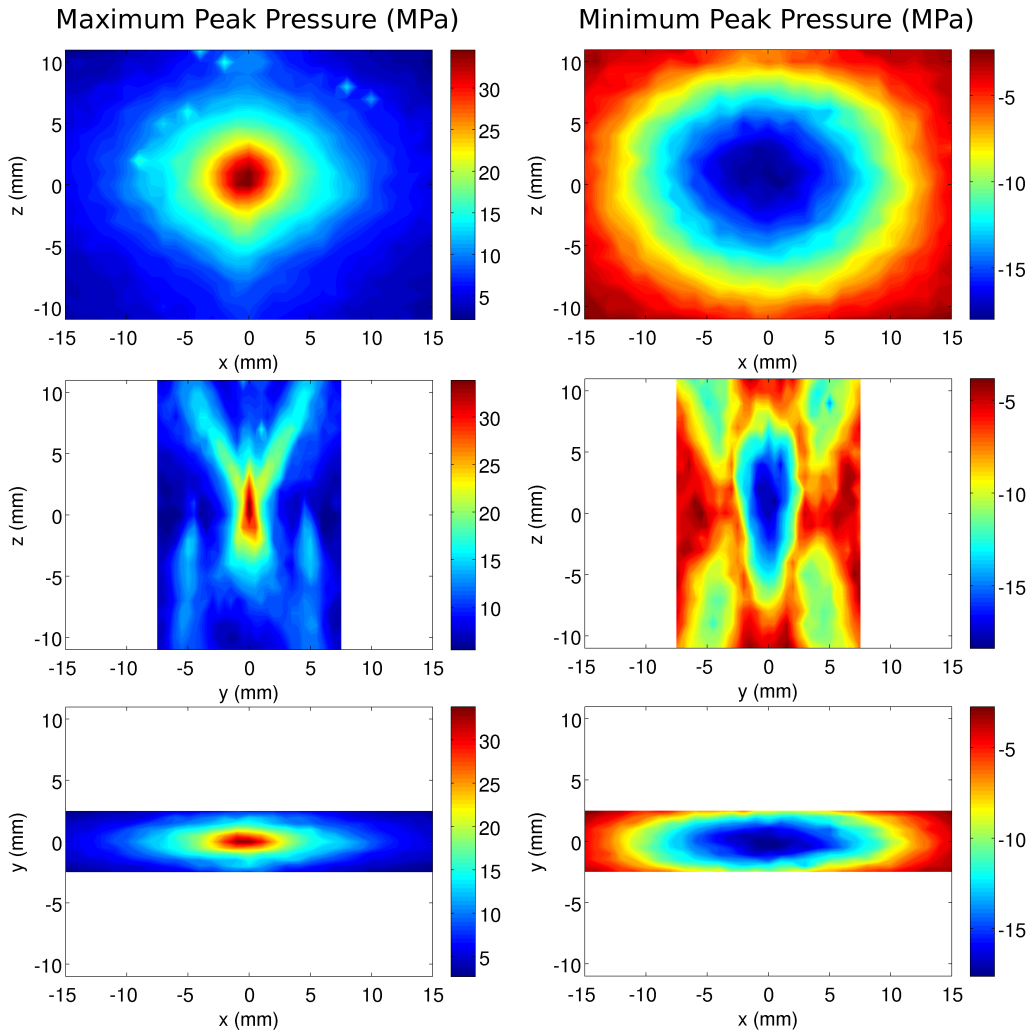

FIGURE 6.6: Pressure field around the focal point of the three 220 kHz transducers confocal. Left: maximum of the first peak positive pressure. Right: minimum of the first peak negative pressure.

The focused beam of peak positive pressure formed by the three transducers confocal setup could therefore be described as a thin disc perpendicular to the plane formed by the transducers axis. The unusually large focused beam formed by the peak negative pressure is the result of the beams crossing before the focal point and the non linearity: as seen in fig.6.1.a, the peak of the negative pressure is located before the peak positive pressure due to the non linearity.

6.3.4 Pressure field of the 4 transducers confocal setup

This confocal setup's main objective was to serve as comparison for the lithotripsy case of narrow focal width and high pressure, and is only used with the 220 kHz transducers. The geometrical focal distance of the bowl was 180 mm, thus the focal beam of the transducers cross 8 mm before their individual focal point, and

the z-axis was chosen as the axisymmetric axis of the bowl. The resulting axisymmetric focal beam is presented in fig. 6.7 and its characteristics are detailed in table 6.3.

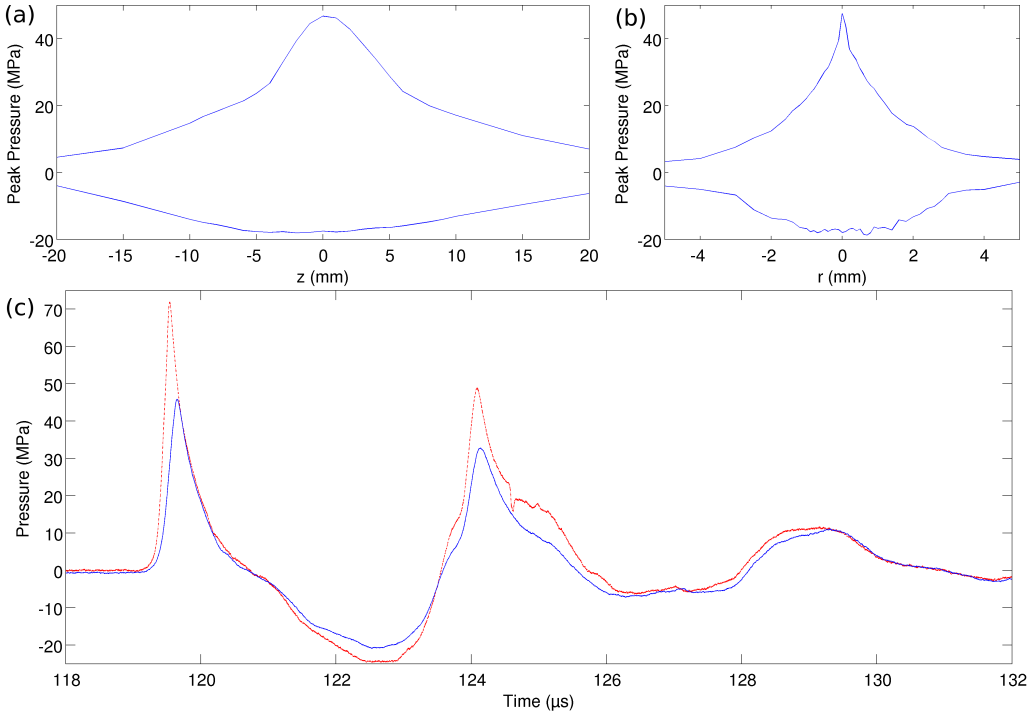

FIGURE 6.7: Acoustic characterization of the four transducers confocal setup, —— 220 kHz transducers at 80% max voltage, -·-·- 220 kHz transducers at max voltage. (a) Axial length of the focus. (b) Radial width of the focus. (c) Waveforms at the focal points.

TABLE 6.3: Focal beam characteristics of the four transducers confocal setup.

Transducers frequency (kHz)	-6dB r-axis width (mm)	-6dB z-axis length (mm)	Peak pressure (MPa)
220	2.1	10.9	$71.9/-24.3$

As expected, this setup presents a very narrow focal width, very similar to the y-axis width of the three transducers setup. As for the three transducers setup, since the individual beam of each transducer cross prefocaly, the wavefront is less steep and the maximum pressure is inferior to the sum of the maximum pressures of the individual transducers.

6.3.5 Discussion

While the three transducers confocal setup does have the expected disc shaped focal volume, the diameter of the disc is unfortunately still too small to trigger the

dynamic squeezing phenomenon (described in [72]) on some stones, as the maximum size of stones treated by ESWL is around 15 mm. Still, the 'cutting' effect desired initially by exposing a large surface to the shear stress generated by the thin y-axis focal width is present and will be evaluated in the next section.

In a classical lithotripter, the depth of the focus can change in relation to the pressure output desired due to the non linear effect, as it is observed here for each independent lens focused transducer. However here, as a result of the confocal setup, the position of the focus of both the three and four transducers confocal setups is the same for every power output of the transducers, as the lens focused transducer acoustic beams always cross each other before their individual focus.

As seen in figs. 6.5.d and 6.7.c, the waveforms at the focus of the confocal setups present a second peak positive pressure of high intensity, a second negative peak pressure and a non negligible third positive peak pressure. In the case of the four 220 kHz transducers confocal setup at full power, the second peak and third positive peak pressure have a pressure equal to 68% and 16% of the first peak, respectively, while the second negative pressure peak have around 25% the amplitude of the first one. In traditional lithotripsy, the focus is usually composed of only one pulse, with maybe a few trailing pulses of almost negligible amplitude. The impact of these pulses on the cavitation and the kidney stone fragmentation will be discussed in the next section.

6.4 Cavitation at the focus of the confocal setups

As the waveform at the focus of the confocal setup is not the traditionally observed single pulse, but is rather halfway between a lithotripsy pulse and an histotripsy burst, observations of the cavitation in the free field and at the surface of a stone are made. The high negative pressure at the focus will generate a rapid growth of the micro bubbles present naturally in fluids (water, urine, blood, ...) or in tissues into large bubbles that will then be impacted by the trailing shock waves.

In the free field, this interaction has been studied experimentally [140], [176], [177] and numerically [178], [179]. When the shock wave hits a single bubble, the side first in contact with the shock wave will collapse sooner than the opposite side, resulting in the creation of a fast liquid jet in the same direction than the shock wave propagation. This jetting is dependent on the size of the bubble in relation to the speed of the shock wave and its wavelength, *i.e.* if the bubble is too small compared to the shock wave speed, the jetting will not occur as both sides of the bubble will be exposed almost instantaneously to the shock wave, while a low period shock wave will generate a weaker jet. The secondary shock wave generated by this forced collapse is also important, and its intensity is dependent on the state of the bubble when the shock wave impacts it: the closer the bubble is to its natural collapse, the stronger the secondary shock wave is and the faster its jet speed is.

The case of a bubble close to a wall was also studied numerically [180]. It was shown that the water hammer created during the jetting can generate a secondary shock wave with local pressure more than ten times superior to the initial shock

wave, and this secondary shock wave can even generate higher pressures on the wall than the initial shock wave, depending on the wall-bubble distance.

Due to the large focal volume, the cavitation in lithotripsy usually consists of large and dense bubble clouds. In 2005, Arora *et al.* studied the influence of a second peak positive pressure on the free field of a lithotripter: although with pressure halved compared to our case, they observed that the bubble cluster had a shorter lifespan if a second peak pressure immediately followed the negative peak pressure of the lithotripsy shock wave [181].

This section focuses on the cavitation dynamics in the free field for both confocal setups, and also the case where a partial reflector (*e.g.* a kidney stone) is at the focus of the setups.

6.4.1 Experimental setup

The confocal setups were placed inside a tank of dimensions 50x80x50 cm and filled with degassed water, and in the time frame of the experiments the gas concentration was always lower than 2.5 mg/L O_2. The minimum distance between the focus and the closest boundary (here the water surface) was 10 cm. Cavitation photographs were captured with a CMOS high speed camera (Phantom V12.1, Vision research, NJ, USA) equipped with a 12x objective lens (Navitar, NY, USA). The backlight illumination was assured by a continuous LED light source. The central frequency of the transducers used in this section is 220 kHz and their power output was always 100%. In the photographs, the confocal setup is at the bottom, out of frame, and thus the acoustic propagation is from bottom to top.

As a human or model stone would break and generate powder during the treatments which render difficult identifying properly the cavitation phenomenon, the treatments were instead made on an epoxy stone. The stone was a rectangle of dimension 14x14x26 mm made with an epoxy (Loctite Stycast 2651 MM, Henkel, Dusseldorf, Germany) mixed with tungsten powder (mass proportion were 75%/25%) in order to elevate its acoustic impedance. The measured acoustic impedance of the loaded epoxy stone was 4.9 Mrayl, which is in the range of human kidney stones (between 4.4 and 9.2 Mrayl [24]).

Due to the tank size limitation, cavitation imaging was only possible in the YZ plan for the three transducers confocal setup.

6.4.2 Free field

As during a lithotripsy treatment many shock waves miss the stone due to the patient movements, imaging the cavitation in the free field case can give an idea of the level of cavitation activity in that specific case. Photographs of the bubble cluster for both setups around 50 μs after the shock wave arrives at the focus and around the time when the maximum bubble radius is reached are shown in fig. 6.8.

In the case of the three transducers setup, the bubble clouds can be easily correlated to the YZ negative pressure field in fig. 6.6, with a large cavitation cloud at the center, four smaller bubble clouds at the side lobes, and since the

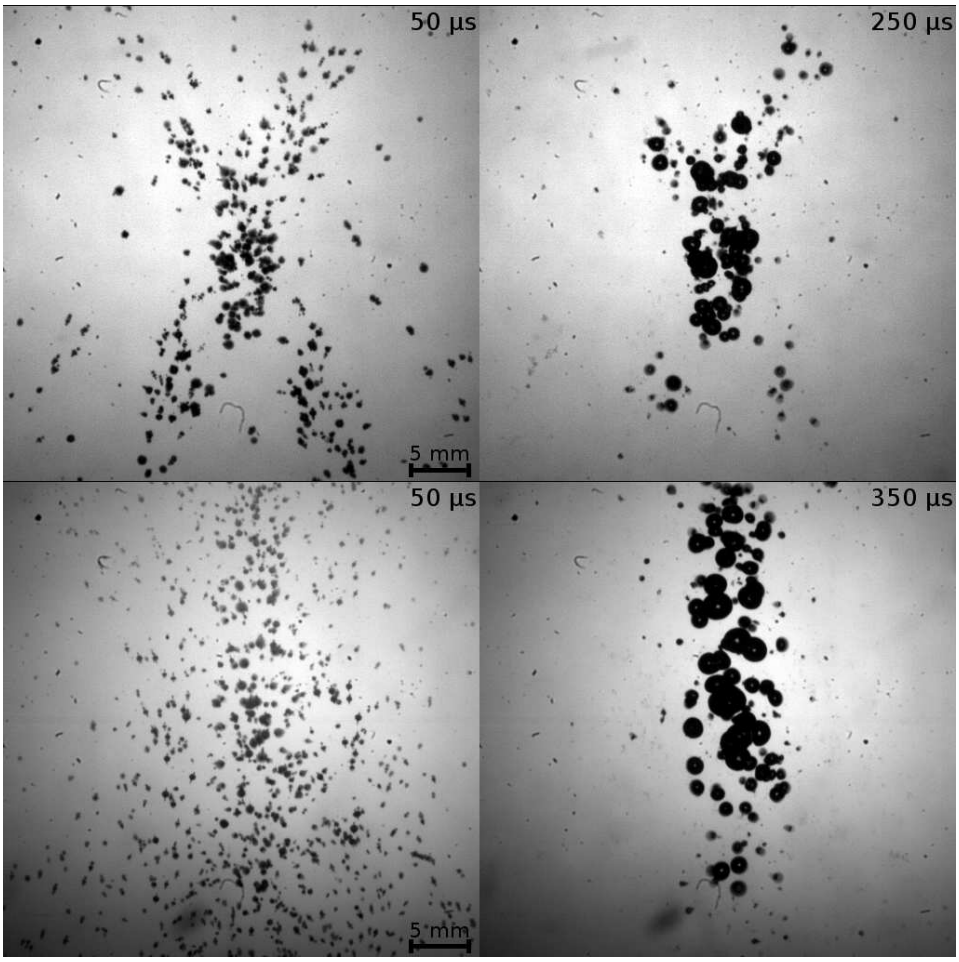

FIGURE 6.8: Photographs of the cavitation generated at the focus of the confocal setups. The size of each frame is 38x38 mm with the focus of the setups centered, and the camera exposure was 47 μs. Top: Three transducers confocal setup. Bottom: Four transducers confocal setup.

whole frame is exposed to a weak negative pressure (around -4 MPa) individual bubbles appear sparsely everywhere else. The largest bubbles are confined in the main lobe, and present a maximum radius of $\sim$1 mm and a lifespan of $\sim$350 μs. Comparatively, the cavitation at the focus of the four transducers setup is dense at the axisymmetric axis and become sparser the further away from the axis. The largest bubbles form a cylinder of diameter $\sim$6.5 mm and height $\sim$30 mm, which is close to the -6 dB characteristic of the negative pressure field, and have a maximum radius of $\sim$1.3 mm and a lifespan of $\sim$450 μs.

In both 50 μs photographs, bubble jetting is clearly visible. Photographs at the focus of the confocal setups about 5 μs after the second shock wave hits the bubbles are shown in fig. 6.9.

Around the center of the focus, the bubble jets are roughly always directed along the closest axis of propagation, or their sum if located in between. This means that, during the treatment, the jetting will be directed toward the stone.

Multiple phenomena can be observed on the time series shown in fig. 6.10.

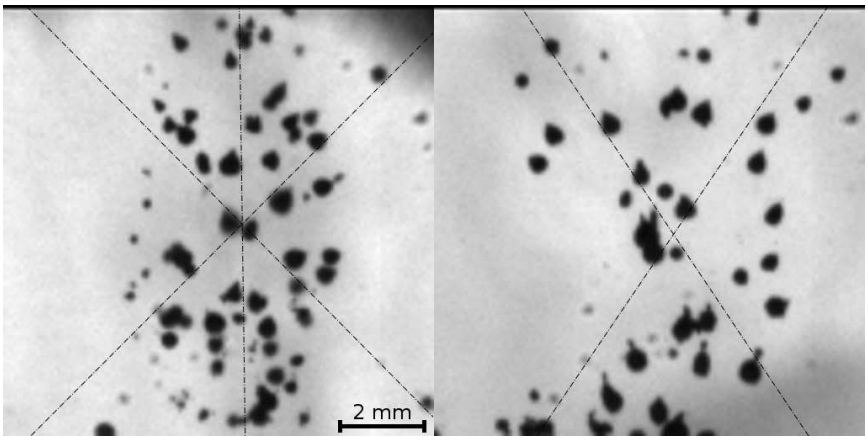

FIGURE 6.9: Photographs with a camera exposure of 1.7 μs of the jetting about 5 μs after the second shock wave. - - -: axis of each individual transducer. Left: Three transducers confocal setup. Right: Four transducers confocal setup.

First, the jetting of bubble 4 and 8 is typical of the jetting of a single bubble due to shock wave exposure as reported in the literature, however here a backward jetting phase is also observable. As reported in most articles on bubble jetting resulting of an interaction with a shock wave, the jetting bubbles move of about one radius in the direction of their jet and some bubbles, namely here bubble 5, do not jet but rather collapse. It is also clear that bubbles 4 and 3 partially shield bubbles 1 and 2, respectively, as their jets are slower and the jet direction of bubble 2 is different than the other bubbles around. The bubble created during the jetting of bubble 4 coalesces rapidly with the closest bubble, here bubble 1, while the jetting of bubble 7 seems to bounce off bubble 6. Finally, during the final collapse of the bubbles (t>293 μs), large bubbles that are in contact with each other collapse simultaneously.

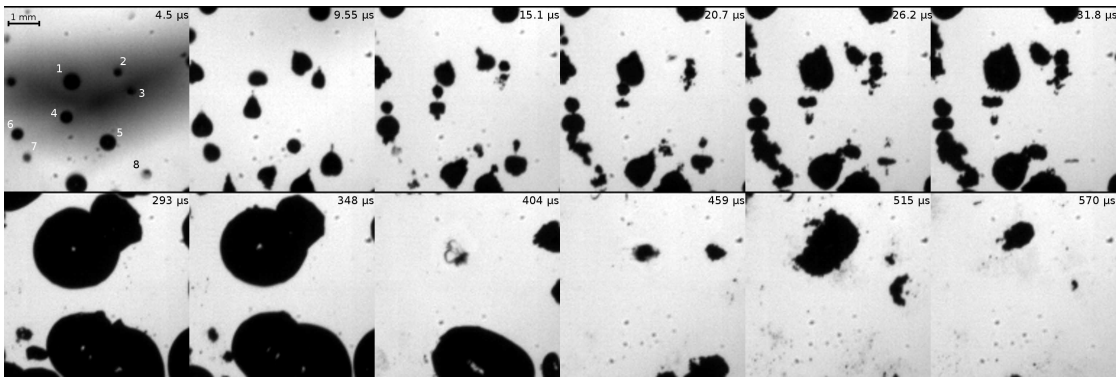

FIGURE 6.10: High speed photographic time series of the cavitation at the focus of the four 220 kHz transducers confocal setup. The time reference t=0 μs is set when the first peak positive pressure is at the center of the focus. Top: Jetting of the bubbles. At t=4.5 μs, the schlieren shadow of the front of the second shock wave is visible. Bottom: Collapse and rebound of the bubbles.

6.4.3 Partial reflector

In this section, the focuses of both setups are set at the surface of the partial reflector, *i.e.* the loaded epoxy stone. Photographs of the bubble cluster at the surface of the stone and around it are shown in fig. 6.11.

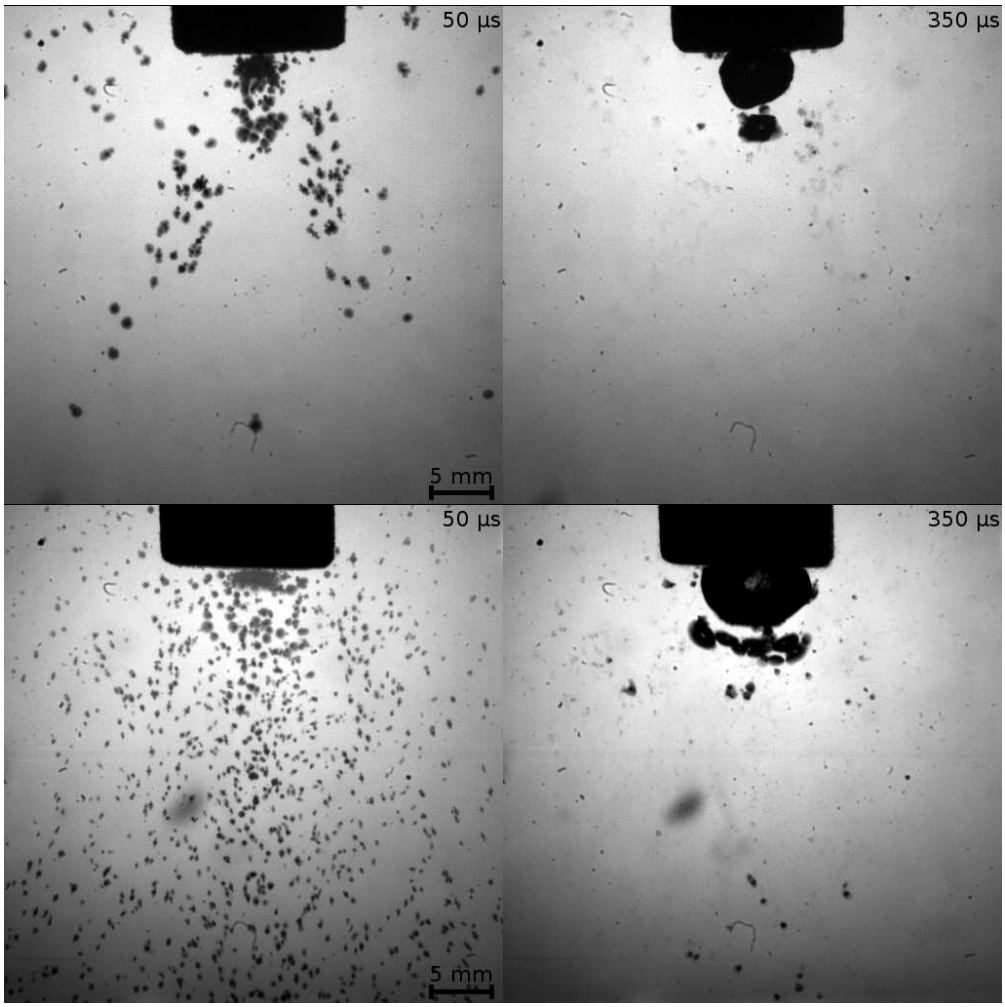

FIGURE 6.11: Photographs of the cavitation field generated in presence of the epoxy stone. The size of each frame is 38x38 mm, and the camera exposure was 47 μs. Top: Three transducers confocal setup. Bottom: Four transducers confocal setup.

In both confocal setups, the bubble cloud spatial and size distribution up to the surface of the stone is almost identical to the one in the free field case. The large bubble cloud visible for both setups at 50 μs on the surface of the stone is due to the impedance mismatch between the stone and the water. It results in a partial reflection of around 53% of the incoming shock wave, and therefore in a small volume in front of the stone, the incoming and reflected waves are summed, thus generating negative pressures up to -26 MPa and -33 MPa for the three transducers and four transducers confocal setups, respectively. These negative pressure values are beyond the intrinsic cavitation threshold, resulting in the creation of

a dense cloud of microbubbles[124]. These microbubbles will then rapidly coalesce and grow into a large bubble cluster, with radius up to ∼2.9 mm and ∼ 4.2 mm for the three transducers and four transducers confocal setups, respectively. These large bubble clusters will then collapse violently onto the surface of the stones, generating a strong jet.

A closer look at these successive phenomena is presented in fig. 6.12 in the case of the four transducers confocal setup. On the first photograph, which correspond to about one period after the first peak positive pressure arrives onto the surface of the stone, a dense microbubble cloud close to the surface of the stone is visible, as well as the schlieren shadow of the front of the second shock wave. This bubble layer implies that the stone is shielded from most of the trailing shock wave. This means that, on a mechanical point of view, the effect of the trailing shock waves on the fragmentation of the stone might be negligible due to cavitation shielding on the proximal face of the stone. The next photographs show the rapid coalescence and growth into a large bubble cluster of the microbubble cloud, which also coalesces with neighboring bubbles. This phenomenon was already reported with a traditional, single pulse lithotripter [79], although with smaller bubble cluster due to lower negative pressure. The growth of the bubble cluster is so intense that the shape of the bubbles away from it is also affected. Finally, the large bubble cluster collapse rapidly on the surface of the stone, creating a fast jet visible in the last photograph. A rebound with dense cavitation cluster that will grow and collapse multiple times is also present on the surface of the stone after the event of the high speed photographic time series. The cavitation activity of the three transducers setup is almost identical, although with a smaller bubble cluster.

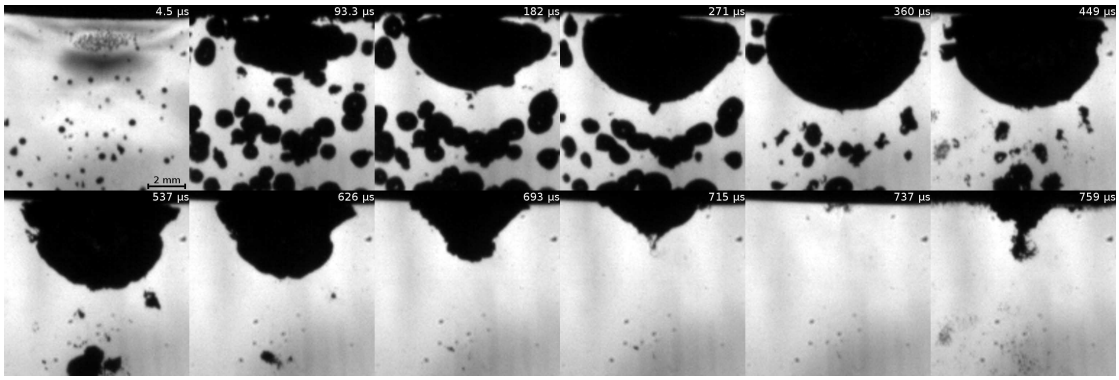

FIGURE 6.12: High speed photographic time series of the cavitation on the surface of the epoxy stone (here on the top side) for the four transducers confocal setup. The time reference t=0 μs is set when the first peak positive pressure arrives at the surface of the stone. The time scale changes for the last 4 pictures to better show the final collapse of the bubble cluster

Bubbles jetting toward the surface of the stone but outside the microbubble cloud after being hit by the trailing shock wave are shown in fig. 6.13. Due to the density of the microbubble cloud and the resolution of the camera, we unfortunately cannot conclude on the jetting of these microbubbles.

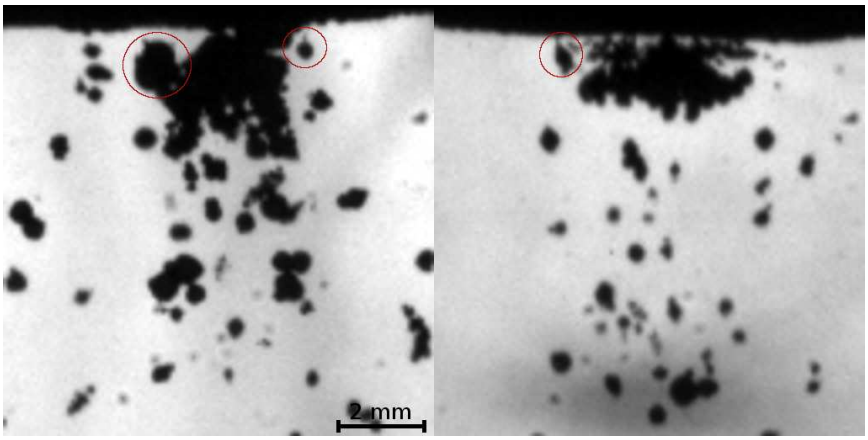

FIGURE 6.13: Photographs of the bubble jetting close to the surface of the loaded epoxy stone after the passage of the second shock wave. The jetting bubbles are circled in red. Left: Three transducers confocal setup. Right: Four transducers confocal setup.

6.4.4 Discussion

Multiple bubble jetting at the bubble cloud generated by both confocal setups due to the trailing shock waves was shown in the free field. The jet of these bubbles is known for being able to pierce elastic membranes and is therefore likely to generate tissue damage [182]. However, the bubbles are hit by the shock wave early in their expansion phase, resulting in minimal secondary shock wave, as well as a reduced bubble lifespan [177]. Such jetting was also observed close to the surface of the stone (fig. 6.13), but considering the above mentioned induced effects, they would have limited impact on the fragmentation of the stone as well.

While the trailing shock waves at the focus of the confocal setups definitively have an impact on the free field cavitation, they only have a limited impact on the fragmentation of the stone due to the bubble shielding at the proximal face of the stone. The cavitation cluster observed at the surface of the stone only differs from traditional lithotripter by its size, due to either the high negative pressure of the confocal setups, by the secondary shock wave, or even both.

6.5 In-vitro artificial stone comminution

6.5.1 Experimental setup

In order to compare the efficiency of each setup, in-vitro artificial stone fragmentation tests were made. The artificial stones were made of BegoStone plaster powder (BEGO, Bremen, Germany) [25], and had a cylindrical shape with a diameter of 13 mm and a length of 14 mm. The artificial stones were always rehydrated with degassed water for at least 24 hours before the fragmentation experiments.

The confocal setups were then immersed in a tank of degassed water ($\sim$2 mg/L O_2). The stone was put in a basket with a 2 mm mesh, the focal point of the setup being positioned at about 5 mm from the bottom of the stone. This location

was determined to be optimal as it allows the maximum stone volume exposure during the whole fragmentation process. The fragments were retrieved by a recipient under the basket during the treatment. The pulse repetition frequency (PRF) of all the treatment was 1 Hz, and the number of pulses until the basket was free of stone fragments served as comparison between the different setups.

The same fragmentation tests were made with two commercial lithotripters from EDAP-TMS for comparison purpose: the Sonolith i-Move and an unreleased piezoelectric model. The i-Move is an electroconductive lithotripter, where a spark is generated at one focus of an ellipsoid, and the piezoelectric lithotripter is made of multiple cylindrical elements that are spherically focused. Their respective acoustic characterization are detailed in table 6.4.

TABLE 6.4: Focal beam characteristics of the commercial lithotripters.

Lithotripter	Pulse frequency (kHz)	-6dB r-axis width (mm)	-6dB z-axis length (mm)	Peak pressure (MPa)
i-Move	∼150	3	35	$100/-10$
Piezoelectric	270	2.4	20	$113/-20$

6.5.2 Results

The fragmentation tests were made for 3 different pressure levels, 80%, 90% and 100% of the maximum voltage input, and on four different setups: the 220, 300 and 400 kHz three transducers confocal setups and the 220 kHz four transducers confocal setup. In each case, the fragmentation was done on four stones (n=4). The number of pulses before complete fragmentation in relation to the maximum positive pressure is shown in fig. 6.14. Results at max pressure are detailed in table 6.5 along with the results for the commercial lithotripters.

One observable difference in fragmentation between the narrow focal lithotripters (four transducers confocal setup, i-Move and piezoelectric) and the 220 kHz three transducers confocal setup is, while the first kind mostly fragment the stones small piece by piece, often leaving large sized pieces in the basket during more than half the treatment time, the second one divides the stones in almost equal sized fragments until they are small enough to pass the 2 mm mesh. No significant differences were found in the fragments size after the treatments between the different lithotripters: a large proportion of the fragments were between 1 mm and 2 mm, with a slightly higher proportion of < 1 mm powder for the 300 kHz and 400 kHz transducers confocal setups, but this is mostly related to the longer treatment time and thus longer exposure to cavitation.

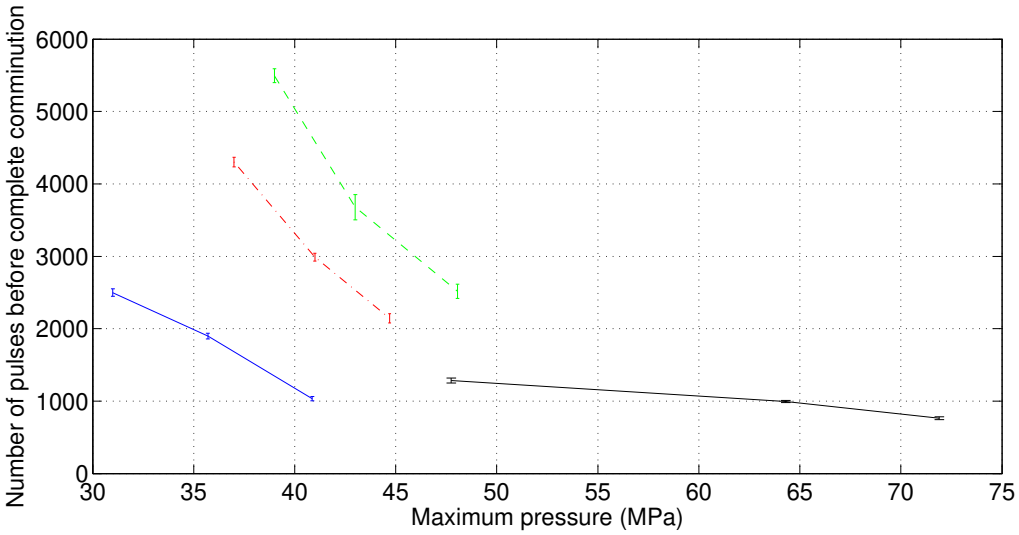

FIGURE 6.14: Number of pulses before complete fragmentation in relation to the maximum pressure, —— Three 220 kHz transducers confocal, -·-·- Three 300 kHz transducers confocal, - - - Three 400 kHz transducers confocal, —— Four 220 kHz transducers confocal

TABLE 6.5: Fragmentation evaluation of the different setups at maximum power.

Lithotripter model	Pulse frequency (kHz)	Peak positive pressure (MPa)	Pulses (n=4) to complete fragmentation ($\leq$2mm)
Three transducers confocal	220 300 400	40.87 44.7 48.06	1034 ± 28 2142 ± 63 2515 ± 99
Four transducers confocal	220	71.9	764 ± 21
EDAP-TMS i-Move	150	100	511 ± 13
EDAP-TMS Piezoelectric	270	113	742 ± 28

6.5.3 Discussion

The first observation that can be made about the three transducers confocal setup from fig. 6.14 is that the fragmentation speed is heavily dependant on the frequency of the transducers: the treatment with the 220 kHz transducers is around 4.7 times faster than with the 400 kHz transducers and around 3.1 times faster than with the 300 kHz transducers at equivalent maximum pressure. This is most likely due to the 220 kHz setup delivering an overall much higher energy to the stone than the other two, mostly a result of the longer period but also due

to the larger focal volume (see table 6.2).

The pressure also plays a very important role in the fragmentation speed, even more so for the three transducers case where, in the 220 kHz case, $\sim$167 more shocks are needed per 1 MPa decrease in maximum focal pressure. As the idea behind the three transducers setup was to generate shear forces by having a strong gradient of tensile stress on one axis of the focus, and considering that the y-axis width does not change much with the pressure (as it should not in the case of a confocal setup) a loss in pressure results in a weaker gradient and thus weaker shear forces inside the stone. Meaning that the opposite might be true, a small increase in pressure may increase the efficiency greatly. Unfortunately, in our case the pressure could not be increased further without risking to break the transducers. Another solution could be to widen even more the x-axis width while keeping those pressure level, with the advantage that dynamic squeezing might participate into the stone comminution and therefore give a sudden increase of efficiency. But even so it is not sure that dynamic squeezing could have a strong impact here as it is normally the result of the acoustic pressure surrounding the whole stone, while here it will only surround it in a plane section.

Meanwhile, the four transducers confocal setup yields results equal to those of a commercial lithotripter. While the low ratio of active surface by the total lithotripsy transducer surface seems like a waste at first, this space could be easily used to place an inline ultrasound imaging probe, and, for example, low pressure transducers to clear the bubble cloud between each shock wave in order to avoid prefocal cavitation while treating stones with high PRF ($>$ 1 Hz) [106].

Chapter 7

Conclusion and future work

Confocal lithotripters using three and four independently lens focused transducers were characterized and their *in-vitro* stone comminution ability was evaluated and compared to commercial lithotripters. While the three transducers confocal setup did not match commercial lithotripter performance, its performance was reasonable considering its smaller than usual overall surface, and its shape may allow for more flexible treatment than the traditional lithotripters. However, the four transducers confocal setup proved to have performance matching commercial lithotripters while freeing a lot of surfaces that can be fitted with other instruments.

More work on optimization can still be done on the prototypes. As an example, one observation that can be made about the lens focused transducers presented here is that the wave emitted by the ceramic has to go through three different interfaces: the interface between the ceramic and the epoxy, the interface between the epoxy and the 3D printed plastic, and finally the interface between the 3D printed plastic and the water. Each interface generates pressure loss due to the different impedances of each material. Since, as shown in chapter 3, only the first positive peak pressure arrives into the stone and a second positive peak did not, to our knowledge, generate more harm during the treatment, it was decided to remove the half-wavelength part of the lens.

As a result, another version of lens focused transducer was made using epoxy directly for the focusing, *i.e.* an epoxy lens is molded directly onto the ceramic. First, the lens, whose shape was recalculated considering it is made of epoxy instead of 3D printed plastic, is 3D printed and used for creating a RTV (room temperature vulcanized) silicone (Bluesil RTV 141, Elkem, Oslo, Norway) mold. Then, a support for the piezoelectric ceramic is 3D printed, which also include a thread for a nut like the previous version. The ceramic is then glued onto 4 small plots into the support. Finally, the support is joined with the silicone mold and the lens and backing is casted using the same degassed epoxy Stycast 2651 MM and catalyst 24LV than before. The mold, support, and resulting transducer are shown in 7.1.

This lens yielded a first positive peak pressure at the focus around 10% higher than the 3D printed lens and around 30% higher second peak positive pressure.

FIGURE 7.1: Left: RTV-141 silicone mold of the lens. Middle: 3D printed support for the ceramic with the ceramic glued in place. Right: the finished transducer.

Bibliography

[1] J. G. Betts, P. DeSaix, E. Johnson, J. E. Johnson, O. Korol, D. H. Kruse, B. Poe, J. A. Wise, M. Womble, and K. A. Young, *Anatomy and Physiology*. http://cnx.org/contents/14fb4ad7-39a1-4eee-ab6e-3ef2482e3e22@8.26: OpenStax, 2016.

[2] P. D. Vize, A. S. Woolf, and J. B. Bard, *The kidney: From normal development to congenital disease*. Academic Press, 2003.

[3] D Schwalb, M Eshghi, J Cord, R Evans, E Braga, I Franco, J Durso, and J. Addonizio, "The minipig as a practical endourologic model", *Journal of Endourology*, vol. 3, no. 1, pp. 85–90, 1989.

[4] A. P. Evan, B. A. Connors, J. E. Lingeman, P. Blomgren, and L. R. Willis, "Branching patterns of the renal artery of the pig", *The Anatomical Record*, vol. 246, no. 2, pp. 217–223, 1996.

[5] F. J. SAMPAIO, M. A. PEREIRA-SAMPAIO, and L. A. FAVORITO, "The pig kidney as an endourologic model: Anatomic contribution", *Journal of endourology*, vol. 12, no. 1, pp. 45–50, 1998.

[6] M. A. Pereira-Sampaio, L. A. Favorito, and F. J. Sampaio, "Pig kidney: Anatomical relationships between the intrarenal arteries and the kidney collecting system. applied study for urological research and surgical training", *The Journal of urology*, vol. 172, no. 5, pp. 2077–2081, 2004.

[7] H. J. Bagetti Filho, M. A. Pereira-Sampaio, L. A. Favorito, and F. J. Sampaio, "Pig kidney: Anatomical relationships between the renal venous arrangement and the kidney collecting system", *The Journal of urology*, vol. 179, no. 4, pp. 1627–1630, 2008.

[8] K. U. KÖHRMANN, W. BACK, J. BENSEMANN, J. FLORIAN, A. WEBER, F. KAHMANN, J. RASSWEILER, and P. ALKEN, "The isolated perfused kidney of the pig: New model to evaluate shock wave-induced lesions", *Journal of endourology*, vol. 8, no. 2, pp. 105–110, 1994.

[9] A Arefiev, F Prat, J. Chapelon, J Tavakkoli, and D Cathignol, "Ultrasound-induced tissue ablation: Studies on isolated, perfused porcine liver", *Ultrasound in medicine & biology*, vol. 24, no. 7, pp. 1033–1043, 1998.

[10] T. Bergsdorf, S Thüroff, and C. Chaussy, "The isolated perfused kidney: An in vitro test system for evaluation of renal tissue damage induced by high-energy shockwaves sources", *Journal of endourology*, vol. 19, no. 7, pp. 883–888, 2005.

[11] M. Szyrach, P Paschenda, M Afify, J Zeng, and R. Tolba, "Resuscitation of warm ischaemia predamaged porcine kidneys by fibrinolytic preflush with streptokinase: Reduction of animal experiments", *Laboratory animals*, vol. 45, no. 2, pp. 63–69, 2011.

[12] C. D. Scales, A. C. Smith, J. M. Hanley, C. S. Saigal, U. D. in America Project, *et al.*, "Prevalence of kidney stones in the united states", *European urology*, vol. 62, no. 1, pp. 160–165, 2012.

[13] J. Uribarri, M. S. Oh, and H. J. Carroll, "The first kidney stone", *Annals of internal medicine*, vol. 111, no. 12, pp. 1006–1009, 1989.

[14] A. P. Evan, "Physiopathology and etiology of stone formation in the kidney and the urinary tract", *Pediatric Nephrology*, vol. 25, no. 5, pp. 831–841, 2010.

[15] F. L. Coe, J. H. Parks, and J. R. Asplin, "The pathogenesis and treatment of kidney stones", *New England Journal of Medicine*, vol. 327, no. 16, pp. 1141–1152, 1992.

[16] O. W. Moe, "Kidney stones: Pathophysiology and medical management", *The lancet*, vol. 367, no. 9507, pp. 333–344, 2006.

[17] G. C. Curhan, W. C. Willett, E. B. Rimm, and M. J. Stampfer, "Family history and risk of kidney stones.", *Journal of the American Society of Nephrology*, vol. 8, no. 10, pp. 1568–1573, 1997.

[18] ——, "A prospective study of dietary calcium and other nutrients and the risk of symptomatic kidney stones", *New England Journal of Medicine*, vol. 328, no. 12, pp. 833–838, 1993.

[19] G. C. Curhan, W. C. Willett, E. B. Rimm, F. E. Speizer, and M. J. Stampfer, "Body size and risk of kidney stones.", *Journal of the American Society of Nephrology*, vol. 9, no. 9, pp. 1645–1652, 1998.

[20] E. N. Taylor, M. J. Stampfer, and G. C. Curhan, "Obesity, weight gain, and the risk of kidney stones", *Jama*, vol. 293, no. 4, pp. 455–462, 2005.

[21] M. Daudon, O. Traxer, P. Conort, B. Lacour, and P. Jungers, "Type 2 diabetes increases the risk for uric acid stones", *Journal of the American Society of Nephrology*, vol. 17, no. 7, pp. 2026–2033, 2006.

[22] F Ebrahimi and F Wang, "Fracture behavior of urinary stones under compression", *Journal of biomedical materials research*, vol. 23, no. 5, pp. 507–521, 1989.

[23] M. Lokhandwalla and B. Sturtevant, "Fracture mechanics model of stone comminution in eswl and implications for tissue damage", *Physics in Medicine & Biology*, vol. 45, no. 7, p. 1923, 2000.

[24] P Zhong, C. Chuong, and G. Preminger, "Characterization of fracture toughness of renal calculi using a microindentation technique", *Journal of materials science letters*, vol. 12, no. 18, pp. 1460–1462, 1993.

[25] Y. Liu and P. Zhong, "Begostone—a new stone phantom for shock wave lithotripsy research (l)", *The Journal of the Acoustical Society of America*, vol. 112, no. 4, pp. 1265–1268, 2002.

[26] J. A. McAteer, J. C. Williams, R. O. Cleveland, J. Van Cauwelaert, M. R. Bailey, D. A. Lifshitz, and A. P. Evan, "Ultracal-30 gypsum artificial stones for research on the mechanisms of stone breakage in shock wave lithotripsy", *Urological research*, vol. 33, no. 6, pp. 429–434, 2005.

[27] E. Esch, W. N. Simmons, G. Sankin, H. F. Cocks, G. M. Preminger, and P. Zhong, "A simple method for fabricating artificial kidney stones of different physical properties", *Urological research*, vol. 38, no. 4, pp. 315–319, 2010.

[28] A. J. Portis and C. P. Sundaram, "Diagnosis and initial management of kidney stones", *American family physician*, vol. 63, no. 7, pp. 1329–1340, 2001.

[29] J. Vieweg, C. Teh, K. Freed, R. A. Leder, R. H. Smith, R. H. Nelson, and G. M. Preminger, "Unenhanced helical computerized tomography for the evaluation of patients with acute flank pain", *The Journal of urology*, vol. 160, no. 3, pp. 679–684, 1998.

[30] I. Boulay, P. Holtz, W. D. Foley, B. White, and F. P. Begun, "Ureteral calculi: Diagnostic efficacy of helical ct and implications for treatment of patients.", *AJR. American journal of roentgenology*, vol. 172, no. 6, pp. 1485–1490, 1999.

[31] N. C. Dalrymple, M. Verga, K. R. Anderson, P. Bove, A. M. Covey, A. T. Rosenfield, and R. C. Smith, "The value of unenhanced helical computerized tomography in the management of acute flank pain", *The Journal of urology*, vol. 159, no. 3, pp. 735–740, 1998.

[32] G. Bandi, R. J. Meiners, P. J. Pickhardt, and S. Y. Nakada, "Stone measurement by volumetric three-dimensional computed tomography for predicting the outcome after extracorporeal shock wave lithotripsy", *BJU international*, vol. 103, no. 4, pp. 524–528, 2009.

[33] A. R. Kambadakone, B. H. Eisner, O. A. Catalano, and D. V. Sahani, "New and evolving concepts in the imaging and management of urolithiasis: Urologists' perspective", *Radiographics*, vol. 30, no. 3, pp. 603–623, 2010.

[34] J. A. Levine, J. Neitlich, M. Verga, N. Dalrymple, and R. C. Smith, "Ureteral calculi in patients with flank pain: Correlation of plain radiography with unenhanced helical ct.", *Radiology*, vol. 204, no. 1, pp. 27–31, 1997.

[35] S. Yilmaz, T Sindel, G Arslan, C Özkaynak, K Karaali, A Kabaalioğlu, and E Lüleci, "Renal colic: Comparison of spiral ct, us and ivu in the detection of ureteral calculi", *European radiology*, vol. 8, no. 2, pp. 212–217, 1998.

[36] A. Rahmouni, R. Bargoin, A. Herment, N. Bargoin, and N. Vasile, "Color doppler twinkling artifact in hyperechoic regions.", *Radiology*, vol. 199, no. 1, pp. 269–271, 1996.

[37] N Chelfouh, N Grenier, D Higueret, H Trillaud, O Levantal, J. Pariente, and P Ballanger, "Characterization of urinary calculi: In vitro study of" twinkling artifact" revealed by color-flow sonography.", *AJR. American journal of roentgenology*, vol. 171, no. 4, pp. 1055–1060, 1998.

[38] W. Lu, O. A. Sapozhnikov, M. R. Bailey, P. J. Kaczkowski, and L. A. Crum, "Evidence for trapped surface bubbles as the cause for the twinkling artifact in ultrasound imaging", *Ultrasound in medicine & biology*, vol. 39, no. 6, pp. 1026–1038, 2013.

[39] R. R. Winkel, A. Kalhauge, and K.-E. Fredfeldt, "The usefulness of ultrasound colour-doppler twinkling artefact for detecting urolithiasis compared with low dose nonenhanced computerized tomography", *Ultrasound in medicine & biology*, vol. 38, no. 7, pp. 1180–1187, 2012.

[40] M. S. Parmar, "Kidney stones", *BMJ: British Medical Journal*, vol. 328, no. 7453, p. 1420, 2004.

[41] J. W. Segura, G. M. Preminger, D. G. Assimos, S. P. Dretler, R. I. Kahn, J. E. Lingeman, and J. N. Macaluso Jr, "Ureteral stones clinical guidelines panel summary report on the management of ureteral calculi", *The Journal of urology*, vol. 158, no. 5, pp. 1915–1921, 1997.

[42] B. R. Matlaga, B. Chew, B. Eisner, M. Humphreys, B. Knudsen, A. Krambeck, D. Lange, M. Lipkin, N. L. Miller, M. Monga, *et al.*, "Ureteroscopic laser lithotripsy: A review of dusting vs fragmentation with extraction", *Journal of endourology*, vol. 32, no. 1, pp. 1–6, 2018.

[43] M. Sofer, J. D. Watterson, T. A. Wollin, L. Nott, H. Razvi, and J. D. Denstedt, "Holmium: Yag laser lithotripsy for upper urinary tract calculi in 598 patients", *The Journal of urology*, vol. 167, no. 1, pp. 31–34, 2002.

[44] A. Breda, O. Ogunyemi, J. T. Leppert, and P. G. Schulam, "Flexible ureteroscopy and laser lithotripsy for multiple unilateral intrarenal stones", *European urology*, vol. 55, no. 5, pp. 1190–1197, 2009.

[45] O. M. Aboumarzouk, M. Monga, S. G. Kata, O. Traxer, and B. K. Somani, "Flexible ureteroscopy and laser lithotripsy for stones> 2 cm: A systematic review and meta-analysis", *Journal of Endourology*, vol. 26, no. 10, pp. 1257–1263, 2012.

[46] B. Altay, B. Erkurt, and S. Albayrak, "A review study to evaluate holmium: Yag laser lithotripsy with flexible ureteroscopy in patients on ongoing oral anticoagulant therapy", *Lasers in medical science*, vol. 32, no. 7, pp. 1615–1619, 2017.

[47] M. Osman, G. Wendt-Nordahl, K. Heger, M. S. Michel, P. Alken, and T. Knoll, "Percutaneous nephrolithotomy with ultrasonography-guided renal access: Experience from over 300 cases", *BJU international*, vol. 96, no. 6, pp. 875–878, 2005.

[48] A Skolarikos, G Alivizatos, and J. De La Rosette, "Percutaneous nephrolithotomy and its legacy", *European urology*, vol. 47, no. 1, pp. 22–28, 2005.

[49] C. Chaussy, E. Schmiedt, B. Jocham, W. Brendel, B. Forssmann, and V. Walther, "First clinical experience with extracorporeally induced destruction of kidney stones by shock waves", *The Journal of urology*, vol. 127, no. 3, pp. 417–420, 1982.

[50] K. Kerbl, J. Rehman, J. Landman, D. Lee, C. Sundaram, and R. V. Clayman, "Current management of urolithiasis: Progress or regress?", *Journal of endourology*, vol. 16, no. 5, pp. 281–288, 2002.

[51] A. Neisius, N. B. Smith, G. Sankin, N. J. Kuntz, J. F. Madden, D. E. Fovargue, S. Mitran, M. E. Lipkin, W. N. Simmons, G. M. Preminger, *et al.*, "Improving the lens design and performance of a contemporary electromagnetic shock wave lithotripter", *Proceedings of the National Academy of Sciences*, p. 201 319 203, 2014.

[52] R. O. Cleveland and J. A. McAteer, "The physics of shock wave lithotripsy", *Smith's textbook on endourology*, vol. 1, pp. 529–558, 2007.

[53] S. Nachef, D. Cathignol, and A. Birer, "Piezoelectric electronically focused shock wave generator", *The Journal of the Acoustical Society of America*, vol. 92, no. 4, pp. 2292–2292, 1992.

[54] J. Tavakkoli, A. Birer, A. Arefiev, F. Prat, J.-Y. Chapelon, and D. Cathignol, "A piezocomposite shock wave generator with electronic focusing capability: Application for producing cavitation-induced lesions in rabbit liver", *Ultrasound in Medicine and Biology*, vol. 23, no. 1, pp. 107–115, 1997.

[55] M. Fink, "Time reversal of ultrasonic fields. i. basic principles", *IEEE transactions on ultrasonics, ferroelectrics, and frequency control*, vol. 39, no. 5, pp. 555–566, 1992.

[56] M. Fink, C. Prada, F. Wu, and D. Cassereau, "Self focusing in inhomogeneous media with time reversal acoustic mirrors", in *Ultrasonics Symposium, 1989. Proceedings., IEEE 1989*, IEEE, 1989, pp. 681–686.

[57] J.-L. Thomas, F. Wu, and M. Fink, "Time reversal focusing applied to lithotripsy", *Ultrasonic imaging*, vol. 18, no. 2, pp. 106–121, 1996.

[58] A. Derode, P. Roux, and M. Fink, "Robust acoustic time reversal with high-order multiple scattering", *Physical review letters*, vol. 75, no. 23, p. 4206, 1995.

[59] A. Derode, A. Tourin, and M. Fink, "Ultrasonic pulse compression with one-bit time reversal through multiple scattering", *Journal of applied physics*, vol. 85, no. 9, pp. 6343–6352, 1999.

[60] M. Fink, "Time-reversal acoustics", in *Journal of Physics: Conference Series*, IOP Publishing, vol. 118, 2008, p. 012 001.

[61] G. Montaldo, P. Roux, A. Derode, C. Negreira, and M. Fink, "Generation of very high pressure pulses with 1-bit time reversal in a solid waveguide", *The Journal of the Acoustical Society of America*, vol. 110, no. 6, pp. 2849–2857, 2001.

[62] G. Montaldo, P. Roux, A. Derode, C. Negreira, and M. Fink, "Ultrasound shock wave generator with one-bit time reversal in a dispersive medium, application to lithotripsy", *Applied physics letters*, vol. 80, no. 5, pp. 897–899, 2002.

[63] G. Montaldo, D. Palacio, M. Tanter, and M. Fink, "Time reversal kaleidoscope: A smart transducer for three-dimensional ultrasonic imaging", *Applied physics letters*, vol. 84, no. 19, pp. 3879–3881, 2004.

[64] ——, "Building three-dimensional images using a time-reversal chaotic cavity", *IEEE transactions on ultrasonics, ferroelectrics, and frequency control*, vol. 52, no. 9, pp. 1489–1497, 2005.

[65] G. Memoli, M. Caleap, M. Asakawa, D. R. Sahoo, B. W. Drinkwater, and S. Subramanian, "Metamaterial bricks and quantization of meta-surfaces", *Nature Communications*, vol. 8, no. 14608, 2017.

[66] N. B. Dhar, J. Thornton, M. T. Karafa, and S. B. Streem, "A multivariate analysis of risk factors associated with subcapsular hematoma formation following electromagnetic shock wave lithotripsy", *The Journal of urology*, vol. 172, no. 6, pp. 2271–2274, 2004.

[67] E. Sylven, S Agarwal, C. Briant, and R. Cleveland, "High strain rate testing of kidney stones", *Journal of Materials Science: Materials in Medicine*, vol. 15, no. 5, pp. 613–617, 2004.

[68] G. Dahake and S. Gracewski, "Finite difference predictions of p-sv wave propagation inside submerged solids. ii. effect of geometry", *The Journal of the Acoustical Society of America*, vol. 102, no. 4, pp. 2138–2145, 1997.

[69] X. Xi and P. Zhong, "Dynamic photoelastic study of the transient stress field in solids during shock wave lithotripsy", *The Journal of the Acoustical Society of America*, vol. 109, no. 3, pp. 1226–1239, 2001.

[70] W. Eisenmenger, "The mechanisms of stone fragmentation in eswl", *Ultrasound in medicine & biology*, vol. 27, no. 5, pp. 683–693, 2001.

[71] R. O. Cleveland and O. A. Sapozhnikov, "Modeling elastic wave propagation in kidney stones with application to shock wave lithotripsy", *The Journal of the Acoustical Society of America*, vol. 118, no. 4, pp. 2667–2676, 2005.

[72] O. A. Sapozhnikov, A. D. Maxwell, B. MacConaghy, and M. R. Bailey, "A mechanistic analysis of stone fracture in lithotripsy", *The Journal of the Acoustical Society of America*, vol. 121, no. 2, pp. 1190–1202, 2007.

[73] W Eisenmenger, X. Du, C Tang, S Zhao, Y Wang, F Rong, D Dai, M Guan, and A Qi, "The first clinical results of "wide-focus and low-pressure" eswl", *Ultrasound in medicine & biology*, vol. 28, no. 6, pp. 769–774, 2002.

[74] E. Tan, K. Tung, and K. Foo, "Comparative studies of extracorporeal shock wave lithotripsy by dornier hm3, edap lt 01 and sonolith 2000 devices", *The Journal of urology*, vol. 146, no. 2, pp. 294–297, 1991.

[75] L. A. Crum, "Cavitation microjets as a contributory mechanism for renal calculi disintegration in eswl", *The Journal of urology*, vol. 140, no. 6, pp. 1587–1590, 1988.

[76] C. C. Church, "A theoretical study of cavitation generated by an extracorporeal shock wave lithotripter", *The Journal of the Acoustical Society of America*, vol. 86, no. 1, pp. 215–227, 1989.

[77] S. Zhu, F. H. Cocks, G. M. Preminger, and P. Zhong, "The role of stress waves and cavitation in stone comminution in shock wave lithotripsy", *Ultrasound in medicine & biology*, vol. 28, no. 5, pp. 661–671, 2002.

[78] A. P. Duryea, W. W. Roberts, C. A. Cain, and T. L. Hall, "Controlled cavitation to augment swl stone comminution: Mechanistic insights in vitro", *IEEE transactions on ultrasonics, ferroelectrics, and frequency control*, vol. 60, no. 2, pp. 301–309, 2013.

[79] Y. A. Pishchalnikov, O. A. Sapozhnikov, M. R. Bailey, J. C. Williams Jr, R. O. Cleveland, T. Colonius, L. A. Crum, A. P. Evan, and J. A. McAteer, "Cavitation bubble cluster activity in the breakage of kidney stones by lithotripter shockwaves", *Journal of endourology*, vol. 17, no. 7, pp. 435–446, 2003.

[80] R. O. Cleveland, R. Anglade, and R. K. Babayan, "Effect of stone motion on in vitro comminution efficiency of storz modulith slx", *Journal of endourology*, vol. 18, no. 7, pp. 629–633, 2004.

[81] M. Orkisz, M. Bourlion, G. Gimenez, and T. A. Flam, "Real-time target tracking applied to improve fragmentation of renal stones in extra-corporeal lithotripsy", *Machine Vision and Applications*, vol. 11, no. 3, pp. 138–144, 1999.

[82] C.-C. Chang, S. Liang, Y. Pu, C. Chen, I Chen, T. Chen, C.-L. KUO, F. Yu, and Z. Chu, "In vitro study of ultrasound based real-time tracking of renal stones for shock wave lithotripsy: Part 1", *The Journal of urology*, vol. 166, no. 1, pp. 28–32, 2001.

[83] C.-C. CHANG, I Manousakas, Y. Pu, S. Liang, C. Chen, T. Chen, F. Yu, W.-H. YANG, Y.-C. TONG, and C. Kuo, "In vitro study of ultrasound based real-time tracking for renal stones in shock wave lithotripsy: Part ii—a simulated animal experiment", *The Journal of urology*, vol. 167, no. 6, pp. 2594–2597, 2002.

[84] M. Pernot, G. Montaldo, M. Tanter, and M. Fink, ""ultrasonic stars" for time-reversal focusing using induced cavitation bubbles", *Applied physics letters*, vol. 88, no. 3, p. 034 102, 2006.

[85] N. R. Owen, M. R. Bailey, L. A. Crum, O. A. Sapozhnikov, and L. A. Trusov, "The use of resonant scattering to identify stone fracture in shock wave lithotripsy", *The Journal of the Acoustical Society of America*, vol. 121, no. 1, EL41–EL47, 2007.

[86] M Kuwahara, K Kambe, K Taguchi, T Saito, S Shirai, and S Orikasa, "Initial experience using a new type extracorporeal lithotripter with an antimisshot control device.", *The Journal of lithotripsy & stone disease*, vol. 3, no. 2, pp. 141–146, 1991.

[87] T. Kishimoto, K. Yamamoto, T. Sugimoto, H. Yoshihara, and M. Maekawa, "Side effects of extracorporeal shock-wave exposure in patients treated by extracorporeal shock-wave lithotripsy for upper urinary tract stone", *European urology*, vol. 12, pp. 308–313, 1986.

[88] J. E. Lingeman, J. Woods, P. D. Toth, A. P. Evan, and J. A. McAteer, "The role of lithotripsy and its side effects", *The Journal of urology*, vol. 141, no. 3, pp. 793–797, 1989.

[89] J. K. Fine, C. Y. Pak, G. M. Preminger, J. W. Segura, and M. Marberger, "Effect of medical management and residual fragments on recurrent stone formation following shock wave lithotripsy", *The Journal of urology*, vol. 153, no. 1, pp. 27–33, 1995.

[90] A. P. Evan, L. R. Willis, J. E. Lingeman, and J. A. McAteer, "Renal trauma and the risk of long-term complications in shock wave lithotripsy", *Nephron*, vol. 78, no. 1, pp. 1–8, 1998.

[91] J. E. Lingeman and T. B. Kulb, "Hypertension following extracorporeal shock wave lithotripsy", *The Journal of Urology*, vol. 137, no. 6, 142A, 1987.

[92] M. Lokhandwalla and B. Sturtevant, "Mechanical haemolysis in shock wave lithotripsy (swl): I. analysis of cell deformation due to swl flowfields", *Physics in Medicine & Biology*, vol. 46, no. 2, p. 413, 2001.

[93] M. Lokhandwalla, J. A. McAteer, J. C. Williams Jr, and B. Sturtevant, "Mechanical haemolysis in shock wave lithotripsy (swl): Ii. in vitro cell lysis due to shear", *Physics in Medicine & Biology*, vol. 46, no. 4, p. 1245, 2001.

[94] D. Howard and B. Sturtevant, "In vitro study of the mechanical effects of shock-wave lithotripsy", *Ultrasound in Medicine and Biology*, vol. 23, no. 7, pp. 1107–1122, 1997.

[95] M. Delius, R. Denk, C. Berding, H.-G. Liebich, M. Jordan, and W. Brendel, "Biological effects of shock waves: Cavitation by shock waves in piglet liver", *Ultrasound in Medicine and Biology*, vol. 16, no. 5, pp. 467–472, 1990.

[96] D. Dalecki, C. H. Raeman, S. Z. Child, and E. L. Carstensen, "A test for cavitation as a mechanism for intestinal hemorrhage in mice exposed to a piezoelectric lithotripter", *Ultrasound in Medicine and Biology*, vol. 22, no. 4, pp. 493–496, 1996.

[97] J. C. Williams Jr, J. F. Woodward, M. A. Stonehill, A. P. Evan, and J. A. McAteer, "Cell damage by lithotripter shock waves at high pressure to preclude cavitation", *Ultrasound in medicine & biology*, vol. 25, no. 9, pp. 1445–1449, 1999.

[98] L. R. Willis, A. P. Evan, B. A. Connors, Y. Shao, P. M. Blomgren, J. H. Pratt, N. S. Fineberg, and J. E. Lingeman, "Shockwave lithotripsy: Dose-related effects on renal structure, hemodynamics, and tubular function", *Journal of endourology*, vol. 19, no. 1, pp. 90–101, 2005.

[99] B. A. Connors, A. P. Evan, L. R. Willis, P. M. Blomgren, J. E. Lingeman, and N. S. Fineberg, "The effect of discharge voltage on renal injury and impairment caused by lithotripsy in the pig", *Journal of the American Society of Nephrology*, vol. 11, no. 2, pp. 310–318, 2000.

[100] J. A. McAteer, A. P. Evan, J. C. Williams Jr, and J. E. Lingeman, "Treatment protocols to reduce renal injury during shock wave lithotripsy", *Current opinion in urology*, vol. 19, no. 2, p. 192, 2009.

[101] A. P. Evan, J. A. McAteer, B. A. Connors, P. M. Blomgren, and J. E. Lingeman, "Renal injury during shock wave lithotripsy is significantly reduced by slowing the rate of shock wave delivery", *BJU international*, vol. 100, no. 3, pp. 624–628, 2007.

[102] Y. A. Pishchalnikov, J. A. McAteer, and J. C. Williams Jr, "Effect of firing rate on the performance of shock wave lithotriptors", *BJU international*, vol. 102, no. 11, pp. 1681–1686, 2008.

[103] C. E. Brennen, "Fission of collapsing cavitation bubbles", *Journal of Fluid Mechanics*, vol. 472, pp. 153–166, 2002.

[104] Y. A. Pishchalnikov, J. C. Williams Jr, and J. A. McAteer, "Bubble proliferation in the cavitation field of a shock wave lithotripter", *The Journal of the Acoustical Society of America*, vol. 130, no. 2, EL87–EL93, 2011.

[105] O. A. Sapozhnikov, V. A. Khokhlova, M. R. Bailey, J. C. Williams Jr, J. A. McAteer, R. O. Cleveland, and L. A. Crum, "Effect of overpressure and pulse repetition frequency on cavitation in shock wave lithotripsy", *The Journal of the Acoustical Society of America*, vol. 112, no. 3, pp. 1183–1195, 2002.

[106] A. P. Duryea, C. A. Cain, H. A. Tamaddoni, W. W. Roberts, and T. L. Hall, "Removal of residual nuclei following a cavitation event using low-amplitude ultrasound", *IEEE transactions on ultrasonics, ferroelectrics, and frequency control*, vol. 61, no. 10, pp. 1619–1626, 2014.

[107] A. P. Duryea, H. A. Tamaddoni, C. A. Cain, W. W. Roberts, and T. L. Hall, "Removal of residual nuclei following a cavitation event: A parametric study", *IEEE transactions on ultrasonics, ferroelectrics, and frequency control*, vol. 62, no. 9, pp. 1605–1614, 2015.

[108] M. S. Pearle, J. E. Lingeman, R. Leveillee, R. Kuo, G. M. Preminger, R. B. Nadler, J. Macaluso, M. Monga, U. Kumar, J. Dushinski, *et al.*, "Prospective, randomized trial comparing shock wave lithotripsy and ureteroscopy for lower pole caliceal calculi 1 cm or less", *The Journal of urology*, vol. 173, no. 6, 2005.

[109] A. E. Perks, G. Gotto, and J. M. Teichman, "Shock wave lithotripsy correlates with stone density on preoperative computerized tomography", *The Journal of urology*, vol. 178, no. 3, pp. 912–915, 2007.

[110] K. J. Weld, C. Montiglio, M. S. Morris, A. C. Bush, and R. D. Cespedes, "Shock wave lithotripsy success for renal stones based on patient and stone computed tomography characteristics", *Urology*, vol. 70, no. 6, pp. 1043–1046, 2007.

[111] J. Bercoff, M. Tanter, and M. Fink, "Supersonic shear imaging: A new technique for soft tissue elasticity mapping", *IEEE transactions on ultrasonics, ferroelectrics, and frequency control*, vol. 51, no. 4, pp. 396–409, 2004.

[112] M. Tanter, J. Bercoff, A. Athanasiou, T. Deffieux, J.-L. Gennisson, G. Montaldo, M. Muller, A. Tardivon, and M. Fink, "Quantitative assessment of breast lesion viscoelasticity: Initial clinical results using supersonic shear imaging", *Ultrasound in medicine & biology*, vol. 34, no. 9, pp. 1373–1386, 2008.

[113] J.-L. Gennisson, T. Deffieux, E. Macé, G. Montaldo, M. Fink, and M. Tanter, "Viscoelastic and anisotropic mechanical properties of in vivo muscle tissue assessed by supersonic shear imaging", *Ultrasound in medicine & biology*, vol. 36, no. 5, pp. 789–801, 2010.

[114] M. D. Sorensen, A. R. Shah, M. S. Canney, O. A. Sapozhnikov, J. M. Teichman, and M. R. Bailey, "Ureteroscopic ultrasound technology to size kidney stone fragments: Proof of principle using a miniaturized probe in a porcine model", *Journal of endourology*, vol. 24, no. 6, pp. 939–942, 2010.

[115] Z. Xu, A. Ludomirsky, L. Y. Eun, T. L. Hall, B. C. Tran, J. B. Fowlkes, and C. A. Cain, "Controlled ultrasound tissue erosion", *IEEE transactions on ultrasonics, ferroelectrics, and frequency control*, vol. 51, no. 6, pp. 726–736, 2004.

[116] Z. Xu, J. B. Fowlkes, E. D. Rothman, A. M. Levin, and C. A. Cain, "Controlled ultrasound tissue erosion: The role of dynamic interaction between insonation and microbubble activity", *The Journal of the Acoustical Society of America*, vol. 117, no. 1, pp. 424–435, 2005.

[117] T. Hall, J. Fowlkes, and C. Cain, "Imaging feedback of tissue liquefaction (histotripsy) in ultrasound surgery", in *Ultrasonics Symposium, 2005 IEEE*, IEEE, vol. 3, 2005, pp. 1732–1734.

[118] Z. Xu, J. B. Fowlkes, and C. A. Cain, "A new strategy to enhance cavitational tissue erosion using a high-intensity, initiating sequence", *IEEE transactions on ultrasonics, ferroelectrics, and frequency control*, vol. 53, no. 8, pp. 1412–1424, 2006.

[119] K. Kieran, T. L. Hall, J. E. Parsons, J. S. Wolf Jr, J. B. Fowlkes, C. A. Cain, and W. W. Roberts, "Refining histotripsy: Defining the parameter space for the creation of nonthermal lesions with high intensity, pulsed focused ultrasound of the in vitro kidney", *The Journal of urology*, vol. 178, no. 2, pp. 672–676, 2007.

[120] V. A. Khokhlova, J. B. Fowlkes, W. W. Roberts, G. R. Schade, Z. Xu, T. D. Khokhlova, T. L. Hall, A. D. Maxwell, Y.-N. Wang, and C. A. Cain, "Histotripsy methods in mechanical disintegration of tissue: Towards clinical applications", *International journal of hyperthermia*, vol. 31, no. 2, pp. 145–162, 2015.

[121] A. D. Maxwell, C. A. Cain, T. L. Hall, J. B. Fowlkes, and Z. Xu, "Probability of cavitation for single ultrasound pulses applied to tissues and tissue-mimicking materials", *Ultrasound in medicine & biology*, vol. 39, no. 3, pp. 449–465, 2013.

[122] A. D. Maxwell, T.-Y. Wang, C. A. Cain, J. B. Fowlkes, O. A. Sapozhnikov, M. R. Bailey, and Z. Xu, "Cavitation clouds created by shock scattering from bubbles during histotripsy", *The Journal of the Acoustical Society of America*, vol. 130, no. 4, pp. 1888–1898, 2011.

[123] S.-i. Umemura, K.-i. Kawabata, and K. Sasaki, "In vitro and in vivo enhancement of sonodynamically active cavitation by second-harmonic superimposition", *The Journal of the Acoustical Society of America*, vol. 101, no. 1, pp. 569–577, 1997.

[124] K.-W. Lin, Y. Kim, A. D. Maxwell, T.-Y. Wang, T. L. Hall, Z. Xu, J. B. Fowlkes, and C. Cain, "Histotripsy beyond the intrinsic cavitation threshold using very short ultrasound pulses: Microtripsy", *IEEE transactions on ultrasonics, ferroelectrics, and frequency control*, vol. 61, no. 2, pp. 251–265, 2014.

[125] X. Zhang, G. E. Owens, H. S. Gurm, Y. Ding, C. A. Cain, and Z. Xu, "Noninvasive thrombolysis using histotripsy beyond the intrinsic threshold (microtripsy)", *IEEE transactions on ultrasonics, ferroelectrics, and frequency control*, vol. 62, no. 7, pp. 1342–1355, 2015.

[126] K.-W. Lin, A. Duryea, Y. Kim, T. Hall, Z. Xu, and C. Cain, "Dual-beam histotripsy: A low-frequency pump enabling a high-frequency probe for precise lesion formation", *IEEE transactions on ultrasonics, ferroelectrics, and frequency control*, vol. 61, no. 2, pp. 325–340, 2014.

[127] T. Ikeda, S. Yoshizawa, M. Tosaki, J. S. Allen, S. Takagi, N. Ohta, T. Kitamura, and Y. Matsumoto, "Cloud cavitation control for lithotripsy using high intensity focused ultrasound", *Ultrasound in medicine & biology*, vol. 32, no. 9, pp. 1383–1397, 2006.

[128] S. Yoshizawa, T. Ikeda, A. Ito, R. Ota, S. Takagi, and Y. Matsumoto, "High intensity focused ultrasound lithotripsy with cavitating microbubbles", *Medical & biological engineering & computing*, vol. 47, no. 8, pp. 851–860, 2009.

[129] A. P. Duryea, W. W. Roberts, C. A. Cain, and T. L. Hall, "Removal of residual cavitation nuclei to enhance histotripsy erosion of model urinary stones", *IEEE transactions on ultrasonics, ferroelectrics, and frequency control*, vol. 62, no. 5, pp. 896–904, 2015.

[130] A. Shah, N. R. Owen, W. Lu, B. W. Cunitz, P. J. Kaczkowski, J. D. Harper, M. R. Bailey, and L. A. Crum, "Novel ultrasound method to reposition kidney stones", *Urological research*, vol. 38, no. 6, pp. 491–495, 2010.

[131] A. Shah, J. D. Harper, B. W. Cunitz, Y.-N. Wang, M. Paun, J. C. Simon, W. Lu, P. J. Kaczkowski, and M. R. Bailey, "Focused ultrasound to expel calculi from the kidney", *The Journal of urology*, vol. 187, no. 2, pp. 739–743, 2012.

[132] J. D. Harper, B. W. Cunitz, B. Dunmire, F. C. Lee, M. D. Sorensen, R. S. Hsi, J. Thiel, H. Wessells, J. E. Lingeman, and M. R. Bailey, "First in human clinical trial of ultrasonic propulsion of kidney stones", *The Journal of urology*, vol. 195, no. 4, pp. 956–964, 2016.

[133] A. D. Maxwell, B. W. Cunitz, W. Kreider, O. A. Sapozhnikov, R. S. Hsi, J. D. Harper, M. R. Bailey, and M. D. Sorensen, "Fragmentation of urinary calculi in vitro by burst wave lithotripsy", *The Journal of urology*, vol. 193, no. 1, pp. 338–344, 2015.

[134] P. C. May, W. Kreider, A. D. Maxwell, Y.-N. Wang, B. W. Cunitz, P. M. Blomgren, C. D. Johnson, J. S. Park, M. R. Bailey, D. Lee, *et al.*, "Detection and evaluation of renal injury in burst wave lithotripsy using ultrasound and magnetic resonance imaging", *Journal of endourology*, vol. 31, no. 8, pp. 786–792, 2017.

[135] T. A. Zwaschka, J. S. Ahn, B. W. Cunitz, M. R. Bailey, B. Dunmire, M. D. Sorensen, J. D. Harper, and A. D. Maxwell, "Combined burst wave lithotripsy and ultrasonic propulsion for improved urinary stone fragmentation", *Journal of endourology*, vol. 32, no. 4, pp. 344–349, 2018.

[136] K. Maeda, W. Kreider, A. Maxwell, B. Cunitz, T. Colonius, and M. Bailey, "Modeling and experimental analysis of acoustic cavitation bubbles for burst wave lithotripsy", in *Journal of Physics: Conference Series*, IOP Publishing, vol. 656, 2015, p. 012 027.

[137] R. O. Cleveland, M. R. Bailey, N. Fineberg, B. Hartenbaum, M. Lokhandwalla, J. A. McAteer, and B. Sturtevant, "Design and characterization of a research electrohydraulic lithotripter patterned after the dornier hm3", *Review of Scientific Instruments*, vol. 71, no. 6, pp. 2514–2525, 2000.

[138] M. R. Bailey, D. T. Blackstock, R. O. Cleveland, and L. A. Crum, "Comparison of electrohydraulic lithotripters with rigid and pressure-release ellipsoidal reflectors. i. acoustic fields", *The Journal of the Acoustical Society of America*, vol. 104, no. 4, pp. 2517–2524, 1998.

[139] ——, "Comparison of electrohydraulic lithotripters with rigid and pressure-release ellipsoidal reflectors. ii. cavitation fields", *The Journal of the Acoustical Society of America*, vol. 106, no. 2, pp. 1149–1160, 1999.

[140] C. Ohl and R Ikink, "Shock-wave-induced jetting of micron-size bubbles", *Physical review letters*, vol. 90, no. 21, p. 214 502, 2003.

[141] A. P. Duryea, T. L. Hall, A. D. Maxwell, Z. Xu, C. A. Cain, and W. W. Roberts, "Histotripsy erosion of model urinary calculi", *Journal of Endourology*, vol. 25, no. 2, pp. 341–344, 2011.

[142] A. Meitzler, H. Tiersten, A. Warner, D Berlincourt, G. Couqin, and F. Welsh III, *Ieee standard on piezoelectricity*, 1988.

[143] G. Everstine, "Finite element formulatons of structural acoustics problems", *Computers & Structures*, vol. 65, no. 3, pp. 307–321, 1997.

[144] O. Zienkiewicz and P Bettess, "Fluid-structure dynamic interaction and wave forces. an introduction to numerical treatment", *International Journal for Numerical Methods in Engineering*, vol. 13, no. 1, pp. 1–16, 1978.

[145] A. Logg, K.-A. Mardal, and G. Wells, *Automated solution of differential equations by the finite element method: The FEniCS book*. Springer Science & Business Media, 2012, vol. 84.

[146] M. Alnæs, J. Blechta, J. Hake, A. Johansson, B. Kehlet, A. Logg, C. Richardson, J. Ring, M. E. Rognes, and G. N. Wells, "The fenics project version 1.5", *Archive of Numerical Software*, vol. 3, no. 100, 2015.

[147] T. R. Chandrupatla, A. D. Belegundu, T Ramesh, and C. Ray, *Introduction to finite elements in engineering*. Prentice Hall Upper Saddle River, NJ, 2002, vol. 2.

[148] S. Balay, S. Abhyankar, M. F. Adams, J. Brown, P. Brune, K. Buschelman, L. Dalcin, V. Eijkhout, W. D. Gropp, D. Kaushik, M. G. Knepley, L. C. McInnes, K. Rupp, B. F. Smith, S. Zampini, H. Zhang, and H. Zhang, *PETSc Web page*, 2016. [Online]. Available: http://www.mcs.anl.gov/petsc.

[149] R. D. Falgout and U. M. Yang, "Hypre: A library of high performance preconditioners", in *Preconditioners," Lecture Notes in Computer Science*, 2002, pp. 632–641.

[150] N. Perez, M. A. Andrade, F. Buiochi, and J. C. Adamowski, "Identification of elastic, dielectric, and piezoelectric constants in piezoceramic disks", *IEEE transactions on ultrasonics, ferroelectrics, and frequency control*, vol. 57, no. 12, pp. 2772–2783, 2010.

[151] Y. H. Zheng, Y. F. Li, S. W. Wang, and Y. Zhao, "Experiment on yield strength of pzt-4 piezoelectric generating column", in *Applied Mechanics and Materials*, Trans Tech Publ, vol. 441, 2014, pp. 62–65.

[152] P. E. Farrell, D. A. Ham, S. W. Funke, and M. E. Rognes, "Automated derivation of the adjoint of high-level transient finite element programs", *SIAM Journal on Scientific Computing*, vol. 35, no. 4, pp. C369–C393, 2013.

[153] S. W. Funke and P. E. Farrell, "A framework for automated pde-constrained optimisation", *ArXiv preprint arXiv:1302.3894*, 2013.

[154] A. Griewank and A. Walther, "Algorithm 799: Revolve: An implementation of checkpointing for the reverse or adjoint mode of computational differentiation", *ACM Transactions on Mathematical Software (TOMS)*, vol. 26, no. 1, pp. 19–45, 2000.

[155] K. Kim, K. Lee, H. Kim, S. Yoon, and S.-H. Hong, "Dependence of particle volume fraction on sound velocity and attenuation of epdm composites", *Ultrasonics*, vol. 46, no. 2, pp. 177–183, 2007.

[156] J. M. Cannata, T. A. Ritter, W.-H. Chen, R. H. Silverman, and K. K. Shung, "Design of efficient, broadband single-element (20-80 mhz) ultrasonic transducers for medical imaging applications", *IEEE transactions on ultrasonics, ferroelectrics, and frequency control*, vol. 50, no. 11, pp. 1548–1557, 2003.

[157] Y. Kim, A. D. Maxwell, T. L. Hall, Z. Xu, K.-W. Lin, and C. A. Cain, "Rapid prototyping fabrication of focused ultrasound transducers", *IEEE transactions on ultrasonics, ferroelectrics, and frequency control*, vol. 61, no. 9, pp. 1559–1574, 2014.

[158] M. Akiyama and T. Kamakura, "Elliptically curved acoustic lens for emitting strongly focused finite-amplitude beams: Application of the spheroidal beam equation model to the theoretical prediction", *Acoustical science and technology*, vol. 26, no. 3, pp. 279–284, 2005.

[159] E. Bängtsson, D. Noreland, and M. Berggren, "Shape optimization of an acoustic horn", *Computer methods in applied mechanics and engineering*, vol. 192, no. 11, pp. 1533–1571, 2003.

[160] Q. D. Tran, G.-W. Jang, H.-S. Kwon, W.-H. Cho, S.-H. Cho, Y.-H. Cho, and H.-S. Seo, "Shape optimization of acoustic lenses for underwater imaging", *Journal of Mechanical Science and Technology*, vol. 30, no. 10, pp. 4633–4644, 2016.

[161] X. Wang and K.-J. Bathe, "Displacement/pressure based mixed finite element formulations for acoustic fluid-structure interaction problems", *International Journal for Numerical Methods in Engineering*, vol. 40, no. 11, pp. 2001–2017, 1997.

[162] G. H. Yoon, J. S. Jensen, and O. Sigmund, "Topology optimization of acoustic–structure interaction problems using a mixed finite element formulation", *International journal for numerical methods in engineering*, vol. 70, no. 9, pp. 1049–1075, 2007.

[163] G. P. Thomas, J.-Y. Chapelon, J.-C. Béra, and C. Lafon, "Parametric shape optimization of lens-focused piezoelectric ultrasound transducers", *IEEE transactions on ultrasonics, ferroelectrics, and frequency control*, vol. 65, no. 5, pp. 844–850, 2018.

[164] J.-P. Berenger, "A perfectly matched layer for the absorption of electromagnetic waves", *Journal of computational physics*, vol. 114, no. 2, pp. 185–200, 1994.

[165] W. Chew, J. Jin, and E Michielssen, "Complex coordinate stretching as a generalized absorbing boundary condition", *Microwave and Optical Technology Letters*, vol. 15, no. 6, pp. 363–369, 1997.

[166] U. Basu and A. K. Chopra, "Perfectly matched layers for time-harmonic elastodynamics of unbounded domains: Theory and finite-element implementation", *Computer methods in applied mechanics and engineering*, vol. 192, no. 11, pp. 1337–1375, 2003.

[167] H. Allik and T. J. Hughes, "Finite element method for piezoelectric vibration", *International journal for numerical methods in engineering*, vol. 2, no. 2, pp. 151–157, 1970.

[168] G. Allaire, F. Jouve, and A.-M. Toader, "A level-set method for shape optimization", *Comptes Rendus Mathematique*, vol. 334, no. 12, pp. 1125–1130, 2002.

[169] M. Alnæs, J. Blechta, J. Hake, A. Johansson, B. Kehlet, A. Logg, C. Richardson, J. Ring, M. E. Rognes, and G. N. Wells, "The fenics project version 1.5", *Archive of Numerical Software*, vol. 3, no. 100, pp. 9–23, 2015.

[170] K.-J. Bathe, *Finite element procedures*. Klaus-Jurgen Bathe, 2006.

[171] E. Jones, T. Oliphant, and P. Peterson, *Scipy: Open source scientific tools for python*, 2014.

[172] J.-L. Mestas, R. A. Fowler, T. J. Evjen, L. Somaglino, A. Moussatov, J. Ngo, S. Chesnais, S. Røgnvaldsson, S. L. Fossheim, E. A. Nilssen, *et al.*, "Therapeutic efficacy of the combination of doxorubicin-loaded liposomes with inertial cavitation generated by confocal ultrasound in at2 dunning rat tumour model", *Journal of drug targeting*, vol. 22, no. 8, pp. 688–697, 2014.

[173] D. L. Sokolov, M. R. Bailey, and L. A. Crum, "Use of a dual-pulse lithotripter to generate a localized and intensified cavitation field", *The Journal of the Acoustical Society of America*, vol. 110, no. 3, pp. 1685–1695, 2001.

[174] D. Cathignol, *Device and method for producing high-pressure ultrasonic pulses*, US Patent 7,264,597, 2007.

[175] M. Lafond, F. Prieur, F. Chavrier, J.-L. Mestas, and C. Lafon, "Numerical study of a confocal ultrasonic setup for cavitation creation", *The Journal of the Acoustical Society of America*, vol. 141, no. 3, pp. 1953–1961, 2017.

[176] A Philipp, M Delius, C Scheffczyk, A Vogel, and W Lauterborn, "Interaction of lithotripter-generated shock waves with air bubbles", *The Journal of the Acoustical Society of America*, vol. 93, no. 5, pp. 2496–2509, 1993.

[177] G. Sankin, W. Simmons, S. Zhu, and P Zhong, "Shock wave interaction with laser-generated single bubbles", *Physical review letters*, vol. 95, no. 3, p. 034 501, 2005.

[178] E. Klaseboer, S. W. Fong, C. K. Turangan, B. C. Khoo, A. J. Szeri, M. L. Calvisi, G. N. Sankin, and P. Zhong, "Interaction of lithotripter shockwaves with single inertial cavitation bubbles", *Journal of fluid mechanics*, vol. 593, pp. 33–56, 2007.

[179] N. Hawker and Y Ventikos, "Interaction of a strong shockwave with a gas bubble in a liquid medium: A numerical study", *Journal of Fluid Mechanics*, vol. 701, pp. 59–97, 2012.

[180] E. Johnsen and T. Colonius, "Shock-induced collapse of a gas bubble in shockwave lithotripsy", *The Journal of the Acoustical Society of America*, vol. 124, no. 4, pp. 2011–2020, 2008.

[181] M Arora, L Junge, and C. Ohl, "Cavitation cluster dynamics in shock-wave lithotripsy: Part 1. free field", *Ultrasound in medicine & biology*, vol. 31, no. 6, pp. 827–839, 2005.

[182] G. Sankin and P Zhong, "Interaction between shock wave and single inertial bubbles near an elastic boundary", *Physical Review E*, vol. 74, no. 4, p. 046 304, 2006.